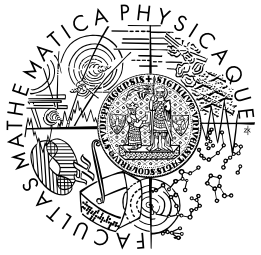

FACULTY
OF MATHEMATICS
AND PHYSICS
Charles University

DOCTORAL THESIS

Ingrid Knapová

Study of gamma decay in ^{168}Er from neutron capture

Institute of Particle and Nuclear Physics

Supervisor of the doctoral thesis: doc. Mgr. Milan Krtička, Ph.D.
Study programme: Physics
Study branch: Particle and Nuclear Physics

Prague 2022

I declare that I carried out this doctoral thesis independently, and only with the cited sources, literature and other professional sources. It has not been used to obtain another or the same degree.

I understand that my work relates to the rights and obligations under the Act No. 121/2000 Sb., the Copyright Act, as amended, in particular the fact that the Charles University has the right to conclude a license agreement on the use of this work as a school work pursuant to Section 60 subsection 1 of the Copyright Act.

In Prague, July 29, 2022 .....

Author's signature

First of all, I would like to express deep gratitude to my supervisor Milan Krtička and consultant Standa Valenta for their time, patience, and endless discussions about all the interesting aspects of nuclear physics. I am very grateful for all their help that was vital for carrying out my doctoral study.

An important aspect of my Ph.D. was the cooperation with the DANCE collaboration and a few stays at Los Alamos National Laboratory. I would like to thank namely Chris, Aaron, John, and John for their hospitality and advice on the analysis of the experimental data.

There are many great people I have met at our institute. I wish to thank Martin for everything and to name a few people who influenced my stay here - Katka and Martin S. whose friendship I appreciate, Tomáš, Stano, and Michal, who showed me everything necessary at the beginning of my doctoral study and Hedvika, who later joined our office.

Last but not least, I thank my family and friends for their support and encouragement on this journey.

Title: Study of gamma decay in ^{168}Er from neutron capture

Author: Ingrid Knapová

Institute: Institute of Particle and Nuclear Physics

Supervisor: doc. Mgr. Milan Krtička, Ph.D., Institute of Particle and Nuclear Physics

Abstract:

The γ-ray emission process in highly-excited nuclei is typically described within the statistical model of nucleus using the two main ingredients - the level density (LD) and the photon strength functions (PSFs). The knowledge of LD and PSFs is essential in the modeling of nuclear reactions with applications in astrophysics or advanced nuclear reactors. In this work, we studied the multi-step γ-ray cascade spectra following the radiative neutron capture $^{167}\mathrm{Er}(n,\gamma)^{168}\mathrm{Er}$ measured with the Detector for Advanced Neutron Capture Experiments in Los Alamos National Laboratory. The experimental γ-ray spectra were compared with the simulated spectra exploiting the DICEBOX Monte Carlo code for simulation of radiative decay to test different models of LD and PSFs.

Furthermore, the measured spectra allowed us to determine the population of the isomeric state in ^{168}Er with 109 ns half-life and compare it with the simulated isomeric population, which provides an important test of the applicability of the statistical model. The simulated isomeric population was found to be significantly lower than the experimental one if no structure effects are assumed above the excitation energy of the isomer. If we adopt the decay scheme up to excitation energy well above 2 MeV, we obtain the simulated isomeric ratio comparable to the experimental one.

This result indicates that the structural effects in ^{168}Er might still play a role in the region of higher excitation energies (likely up to 2.0-2.4 MeV), where the statistical model was successfully used to describe the γ-ray spectra in other rare-earth nuclei.

In addition, from the $^{167}\mathrm{Er}(n,\gamma)^{168}\mathrm{Er}$ data, we were able to assign spins to individual neutron resonances up to energies of several hundred eV. We studied the fluctuation properties of these neutron resonances and compared them with the predictions of the random matrix theory. The Gaussian orthogonal ensemble version of the random matrix theory predicts a very precise determination of the nuclear level spacing if a sequence of neutron resonances is complete. However, we found that the determination of the completeness is problematic and the completeness cannot be guaranteed even for short sequences with tens of resonances.

Keywords: level density, photon strength functions, statistical γ decay, neutron resonances, isomer

Contents

Introduction **3**

1 Level Density **7**
1.1 Statistical Interpretation 7
1.2 Phenomenological Models 7
1.2.1 Back-Shifted Fermi Gas Model 8
1.2.2 Constant Temperature Model 9
1.3 Microscopic Calculations 9
1.4 Experimental Information on Level Density 10

2 Photon Strength Functions **13**
2.1 Introduction of PSFs 13
2.1.1 Probability of Electromagnetic Transitions 13
2.1.2 Selection Rules 14
2.1.3 Average Quantities 14
2.2 Electric Dipole PSF 15
2.2.1 Phenomenological Models of Electric Dipole PSF 15
2.2.2 Microscopic Models of Electric Dipole PSF 18
2.3 Magnetic Dipole PSF 18
2.3.1 Scissors Mode 18
2.3.2 Spin-flip Mode 20
2.3.3 Low-energy Enhancement 20
2.4 Electric Quadrupole PSF 21

3 Simulations of Statistical γ Decay **25**
3.1 Assumptions 25
3.2 Nuclear Realizations and Suprarealizations 26
3.3 Algorithm 27
3.4 Simulation of the Detector Response 29

4 Fluctuation Properties of Neutron Resonances **31**
4.1 Random Matrix Theory 31
4.2 Gaussian Orthogonal Ensemble 31
4.2.1 Fluctuations of Neutron Widths 32
4.2.2 Fluctuations of Resonance Positions 33
4.3 Simulations of GOE Predictions 35
4.3.1 Reduced Neutron Widths 35
4.3.2 Statistics Related to Resonance Positions 35

5 Experiment **37**

5.1 Data Acquisition and Data Processing . . . 37
5.1.1 Experimental Background . . . 38
5.1.2 Energy and Time Calibration . . . 39
5.2 Specifics to Erbium Measurement and Experimental Spectra . . . 40
5.2.1 Sum-energy and MSC Spectra . . . 41
5.2.2 Experimental Isomeric Ratio . . . 44
5.2.3 Parasitic Detector Effects . . . 45
5.3 Spin Assignment of Neutron Resonances . . . 47
5.3.1 Optimized γ-multiplicity-based Spin Assignment Method . . . 47
5.3.2 Spectra of Decomposed Yields . . . 48
5.3.3 Influence of the Detector Effects . . . 50

6 Results and Discussion **53**
6.1 Statistical Properties of Neutron Resonances . . . 53
6.1.1 Fluctuations of Neutron Widths . . . 53
6.1.2 Fluctuations of Resonance Positions . . . 55
6.1.3 Average Resonance Spacing . . . 57
6.2 Level Density and Photon Strength Functions . . . 59
6.2.1 Level Density . . . 61
6.2.2 $E1$ Photon Strength Function . . . 61
6.2.3 $M1$ Photon Strength Function . . . 63
6.2.4 Average Radiative Width . . . 66
6.2.5 Comparison of SM Strength with Other Data . . . 68
6.3 Isomeric Ratio . . . 72
6.3.1 Experimental Isomeric Ratio . . . 72
6.3.2 Simulated Isomeric Ratio . . . 72

Conclusions and Outlook **77**

Bibliography **79**

List of Figures **84**

List of Tables **86**

List of Abbreviations **87**

List of Publications **89**

Appendices **93**

A Spin assignment and statistical properties of neutron resonances from ^{161,163}Dy(n,γ) and ^{167}Er(n,γ) measured at the DANCE facility **93**

B Photon strength functions, level densities and isomeric ratio in ^{168}Er from the radiative neutron capture measured at the DANCE facility **95**

Introduction

In 1932 James Chadwick discovered the neutron, which was immediately exploited as a probe to study nuclear structure. Soon after, Enrico Fermi, motivated by previous measurements with α particles, decided to use neutrons to induce radioactivity in different elements. The bombardment with high-speed neutrons as well as neutrons with thermal velocities resulted in observing the capture of the neutron and subsequential emission of a proton, α particle, or γ radiation. The (n, γ) reaction was however difficult to interpret within the nuclear theory at the time, which could not describe the surprisingly large measured cross sections [1, 2] that exhibited resonances restricted to narrow neutron energy regions.

The existence of the resonances was explained by Bohr's famous model of compound nucleus [3]. He argued that their origin could not be caused by the interaction of a neutron with a single nucleon of the target, where the time scale is in the order of 10^{-22} s. On the contrary, the neutron collides with many nucleons of the target, and its energy is rearranged among them, which creates a complex configuration - the compound nucleus - whose lifetime $\approx 10^{-15}$ s is much longer. This formation is illustrated in Fig. 1, where the neutron with an incident energy provided by the billiard cue is passing through the nuclear interior. It takes the system a long time until a possible emission of a particle or radiation takes place, which can be considered a separate process with no immediate connection to the first stage. The creation of the compound nucleus has the highest probability when the incident neutron's energy is equal to the energy of the level in the spectrum of the compound nucleus.

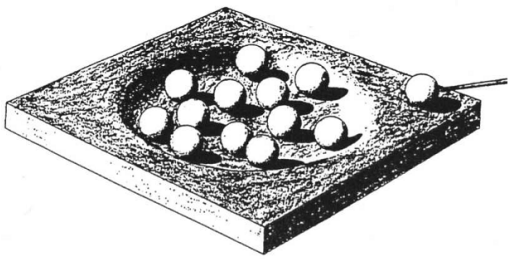

Figure 1: Bohr's wooden toy model illustrating formation of the compound nucleus. The figure is taken from Ref. [4].

A complex scheme of a radiative neutron capture reaction is shown in Fig. 2. A neutron with kinetic energy E_n is captured in the nucleus with mass number A forming a compound nucleus with A+1 nucleons. This so-called *Neutron Resonance* is a highly-excited, well-defined nuclear state with a given energy, spin, and parity. The excitation energy is given by a sum of neutron separation energy S_n (in rare-earth nuclei typically 5–9 MeV) and the kinetic energy E_n of the neutron. This state decays by emission of one or more γ rays until the nucleus reaches its ground state.

Due to the extreme complexity of the nuclear states above S_n, the positions and other properties of these states cannot be predicted within any nuclear model. The nucleus displays a statistical behavior and the fluctuation properties of its

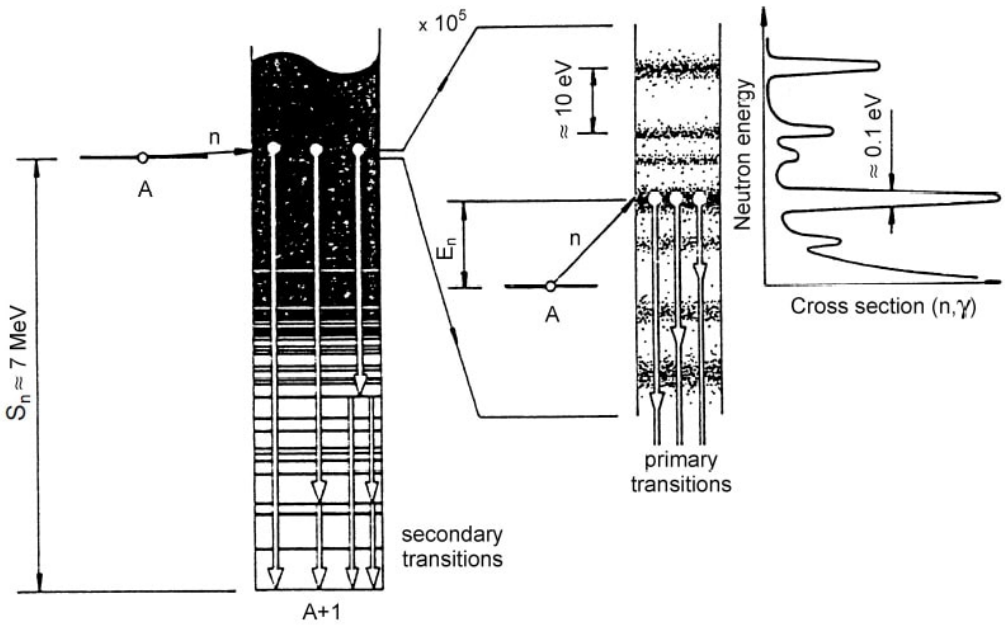

Figure 2: Scheme of a neutron capture reaction, formation of a compound nucleus and following emission of γ rays. The neutron resonances illustrated in the cross section correspond to the excitation of the nuclear levels. The figure is taken from [5].

levels are believed to be described by the *Random Matrix Theory* (RMT), introduced to nuclear physics by Wigner in 1960s [6, 7]. Instead of an actual nuclear Hamiltonian, he considered an ensemble of Hamiltonians expressed in a matrix form, where matrix elements are given in terms of some probability distribution - hence the name random matrices. There is a plethora of experimental evidence that fluctuation properties of neutron resonances follow the predictions of random matrix theory and the details are discussed in Chap 4.

The γ decay following the formation of a neutron resonance in heavy nuclei populates a large number of levels in the energy range between the ground state up to S_n. The levels at low excitation energies just above the ground state are well separated and their properties such as energy, spin, parity, and decay pattern are known from experiments and usually are confirmed by theoretical calculations. With increasing excitation energy the number of levels grows exponentially and they cannot be experimentally resolved anymore. It also becomes impossible to predict individual levels and their properties within nuclear models. Consequently, one has to rely on a statistical approach to describe nuclear level properties using average quantities and fluctuation properties. In even-even well-deformed rare-earth nuclei, this region, which is often referred to as the quasicontinuum, is typically above 2 MeV. In order to describe the γ decay therein, we cannot consider individual levels, but use average quantities within the *Statistical Model* of nucleus - those are *Level Density* (LD) and *Photon Strength Functions* (PSF). These quantities are essential for nuclear reaction calculations involving interaction of photons with nuclei.

Lane and Lynn [8] introduced the PSF in 1959 as a quantity proportional

to the photoabsorption cross section. At that time it was already known that the photoabsorption cross section is dominated by a *Giant Electric Dipole Resonance* (GEDR) [9], a manifestation of the collective vibrations of proton and neutron fluids induced by the incoming γ radiation. The Standard Lorentzian model assuming a Lorentzian shape of the GEDR was very successful to describe the $E1$ transitions at excitation energies above the S_n. However, later it has been shown that the Standard Lorentzian model is inadequate in the energy region below S_n because the situation there is probably much more complicated and many other models of $E1$ PSF have been introduced. Furthermore, similar structures as the GEDR have been observed in $M1$ and $E2$ PSFs which also affect the γ decay below S_n. The current status of the PSFs models is discussed in Chap. 2.

The typical lifetimes of the intermediate states below S_n are in orders of ps. In some nuclei, we also observe states with much longer lifetimes, referred to as nuclear isomers. The population of an isomer is sometimes considerable and its presence thus significantly influences the γ decay of the given nucleus. Describing the population of the short-lived isomers (with half-lives around tens to hundreds of ns) is problematic within the statistical model of γ decay. The analyses of the experimental isomeric population in ^{177}Lu [10, 11] or Hf isotopes [12] revealed a discrepancy between the measured population and the population predicted with simulations using the statistical model. There is a systematic trend of underestimating the simulated populations with respect to the experimental ones.

The aim of this thesis was to study γ decay following the resonance neutron capture on ^{167}Er that was measured by the Detector for Advanced Neutron Capture Experiments (DANCE) located at Los Alamos National Laboratory (LANL). The corresponding even-even rare-earth compound nucleus ^{168}Er is interesting because of its isomeric state of ≈ 109 ns half-life at the excitation energy ≈ 1 MeV. The feeding of this state is so significant that we can observe it in the γ-ray spectra measured with the DANCE detector, which can distinguish between the cascades populating and depopulating the isomer. The acquired γ-ray spectra were compared with the Monte Carlo simulations of the γ decay employing the statistical model of nucleus in order to obtain information about the LD and PSFs. The simulations of γ cascades also provide the isomeric population that can be compared to the experimental one. Furthermore, we assigned spin to measured neutron resonances and performed analysis of the neutron resonance fluctuations, specifically comparing the measured fluctuation properties to the predictions of the random matrix theory.

This work is organized as follows: models of LD that we tested in our analysis are introduced in Chap. 1. The current status of the knowledge on PSFs is discussed in Chap. 2 and the algorithm used for the modeling of the γ decay is described in Chap. 3. A summary of the random matrix theory predictions relevant to our study and measures used to estimate the fluctuation properties of neutron resonances is given in Chap. 4. The DANCE experimental facility, data processing, experimental spectra of the measured γ rays and the experimental method of assigning spin to neutron resonances is discussed in Chap. 5. The main results from $^{167}\mathrm{Er}(n,\gamma)^{168}$Er analysis are presented in Chap. 6 and the conclusions are given in Chap. 6.3.2.

The results concerning statistical properties of neutron resonances are accepted to be published in the form of the paper attached in Appendix A, together

with the analogous analysis of two Dy isotopes. The author of this thesis was responsible for all the work related to $^{167}\mathrm{Er}(n,\gamma)^{168}\mathrm{Er}$, while the methodology and realization of the statistical analysis was a collective work led by the Prague group. The Appendix B includes a paper ready to be submitted that describes the results on LD, PSFs and isomeric ratio deduced from the $^{167}\mathrm{Er}(n,\gamma)$ measurement. In this case, the author of the thesis performed the complete presented analysis.

1. Level Density

Level density is one of the important characteristics of highly excited nuclei. Together with photon strength functions, those are the main quantities necessary for simulating γ decay within the statistical model. Here we introduce the most common phenomenological models of LD, their parametrizations as well as LD derived from microscopic calculations. In addition, we provide a short overview of experimental techniques used to extract the LD in the energy region of our interest.

1.1 Statistical Interpretation

Above a certain region of excitation energies (around $1.5 - 2\,\mathrm{MeV}$ in even-even heavy nuclei) we rely on the statistical model to describe nuclear level properties. Adopting a method from statistical physics, Bethe [13] in 1936 derived a formula for nuclear LD. The main idea is that the complete information on the spectrum is equivalent to the knowledge of the partition function of the system. Assuming a gas of noninteracting fermions with equidistant nondegenerate single-particle levels yields LD ρ at excitation energy E:

$$\rho(E) = \frac{\exp(2\sqrt{aE})}{4\sqrt{3}E}, \tag{1.1}$$

where a is the level density parameter.

1.2 Phenomenological Models

The two most widely used phenomenological models of level density are the Back-Shifted Fermi Gas (BSFG) model and the Constant Temperature (CT) model. The level density is usually expressed in a separable form:

$$\rho(E, J, \pi) = \rho(E) f(J, \sigma) g(\pi) \tag{1.2}$$

with $\rho(E)$ as the total LD, $f(J, \sigma)$ as the spin distribution and $g(\pi)$ is the parity distribution. The spin distribution $f(J, \sigma)$ might depend on excitation energy E through the spin cut-off parameter σ - details are discussed in the following two subsections. Considering gaussian distribution of the spin projections M, the spin distribution function [14, 15], is given as:

$$f(J, \sigma) = \exp\left(-\frac{J^2}{2\sigma}\right) - \exp\left(-\frac{(J+1)^2}{2\sigma}\right) \simeq \frac{2J+1}{2\sigma^2} \exp\left(-\frac{(J+1/2)^2}{2\sigma^2}\right) \tag{1.3}$$

The parity distribution is usually assumed to be $g(\pi) = 1/2$ for each parity, corresponding to the same number of levels with positive and negative parity independently of excitation energy. However, parity dependence cannot be a priori excluded. The asymmetry should decrease with higher excitation energy and for

nuclei with $20 < A < 110$ was proposed to be described with a phenomenological formula [16]:

$$g(\pi = +, E) = \frac{\rho_+(E)}{\rho_+(E) + \rho_-(E)} = \frac{1}{2}\left(1 \pm \frac{1}{1 + \exp[c(E - \delta_p)]}\right) \tag{1.4}$$

where the sign "+" denotes the dominant parity for low-energy levels. Authors proposed $c = 3$ MeV^{-1}, the shift δ_p is different for even-even, odd-even, even-odd and odd-odd nuclei and can be found in [16].

1.2.1 Back-Shifted Fermi Gas Model

This model employs a more realistic expression of the Bethe formula (1.1). Corrections were motivated by the pairing tendency of two types of fermions present in the nucleus. To break such a pair, an extra amount of energy is needed - which is reflected as subtracting an energy shift Δ from the excitation energy E. The resulting *Back-Shifted Fermi Gas* LD formula derived by Gilbert and Cameron has the energy dependence in a form [14]:

$$\rho(E) = \frac{\exp(2\sqrt{a(E - \Delta)})}{12\sqrt{2}\sigma a^{1/4}(E - \Delta)^{5/4}} \tag{1.5}$$

where Gilbert and Cameron proposed the energy shift $\Delta = P(N) + P(Z)$ with $P(N), P(Z)$ being the neutron and proton pairing energies, respectively. In the later works [17, 18], a and Δ were considered free parameters that are nucleus-dependent and can be obtained from reproducing the experimental LD at low excitation energies or in region above the neutron separation energy. Von Egidy and Bucurescu [17] introduced the spin cut-off parameter σ from a global fit of 310 nuclei. The resulting expression is:

$$\sigma^2 = 0.0146A^{5/3}\frac{1 + \sqrt{1 + 4a(E - \Delta)}}{2a} \tag{1.6}$$

where A is the mass number. In the later work [18] the spin cut-off parameter was proposed to be independent of a:

$$\sigma^2 = 0.391A^{0.675}(E - 0.5P_{a'})^{0.312} \tag{1.7}$$

and $P_{a'}$ is the deuteron pairing energy calculated from nucleus masses $M(A, Z)$ as follows:

$$P_{a'} = \frac{1}{2}\left[M(A + 2, Z + 1) - 2M(A, Z) + M(A - 2, Z - 1)\right] \tag{1.8}$$

and can be found in [18].

A deviation of the experimental spin distribution from Eq. (1.3) was observed at low excitation energies for even-even nuclei. This so-called staggering effect manifests as a preference of levels with even spins with respect to odd spins. The corresponding spin distribution function introduced in [18] depends on a staggering parameter x:

$$f_{ee}(J, \sigma) = f(J, \sigma)(1 + x) \tag{1.9}$$

where $x = 0.227$ for even spin, $x = -0.227$ for odd spin and $x = 1.02$ for zero spin. No energy dependence was proposed in the original paper, but the staggering effect is expected to vanish at higher excitation energies.

1.2.2 Constant Temperature Model

Another model proposed by Gilbert and Cameron [14] aimed to describe the experimental low-energy behavior of LD, which for a wide range of nuclei showed an exponential dependence. This is the so-called *Constant Temperature* formula:

$$\rho(E) = \frac{1}{T} \exp\left(\frac{E - E_0}{T}\right) \tag{1.10}$$

with nuclear temperature T and back shift E_0 being the free parameters. The spin cut-off parameter paired with the CTF model in Ref. [17] is a function of A and has a form:

$$\sigma = 0.98A^{0.29} \tag{1.11}$$

In the later work, [18] Eq. (1.7) serves as the spin cut-off parameter formula for both CT and BSFG level density models. It is important to note that both these models work under the assumption of parity independence of level density.

1.3 Microscopic Calculations

The above described phenomenological models adopt relatively simple formulae to parametrize experimental data on LD. On the other hand, they do not explain the energy shifts and dependences on the mass number, which can be performed within numerical microscopic calculations. We will restrict ourselves to microscopic models relevant to this study and tested in our simulations. A comprehensive summary can be found in the RIPL-3 database [21].

One of the methods how to compute level densities relies on a combinatorial approach, which includes counting all the configurations allowed for a given number of nucleons. This approach combined with a single-particle level scheme from axially symmetric Hartree-Fock-Bogoliubov (HFB) method [22, 19] yields microscopic level densities in a tabular form for around 8000 nuclei with $8 \leq Z \leq 110$. The resulting level densities are spin- and parity-dependent and given for each isotope up to excitation energy $E = 200\,\mathrm{MeV}$. The HFB method usually cannot reproduce neither the average neutron resonance spacings nor the low-lying levels, hence a renormalization is suggested [19] to match the LD with the experimental data.

Another approach employs Shell-Model Monte Carlo (SSMC) calculations that transform imaginary-time many-body evolution operator to a superposition of one-body evolutions in fluctuating one-body fields. The SSMC method was applied to heavy rare-earth nuclei such as ^{162}Dy [23] and different isotopes of Sm and Nd [24]. The energy dependence of the LD $\rho(E)$ displays a very similar behavior to the BSFG model in all the above-mentioned isotopes. Calculated spin distribution of the level density in ^{162}Dy agrees with Eq. (1.9) when the staggering parameter x decreases linearly with excitation energy to zero at $E = 4\,\mathrm{MeV}$.

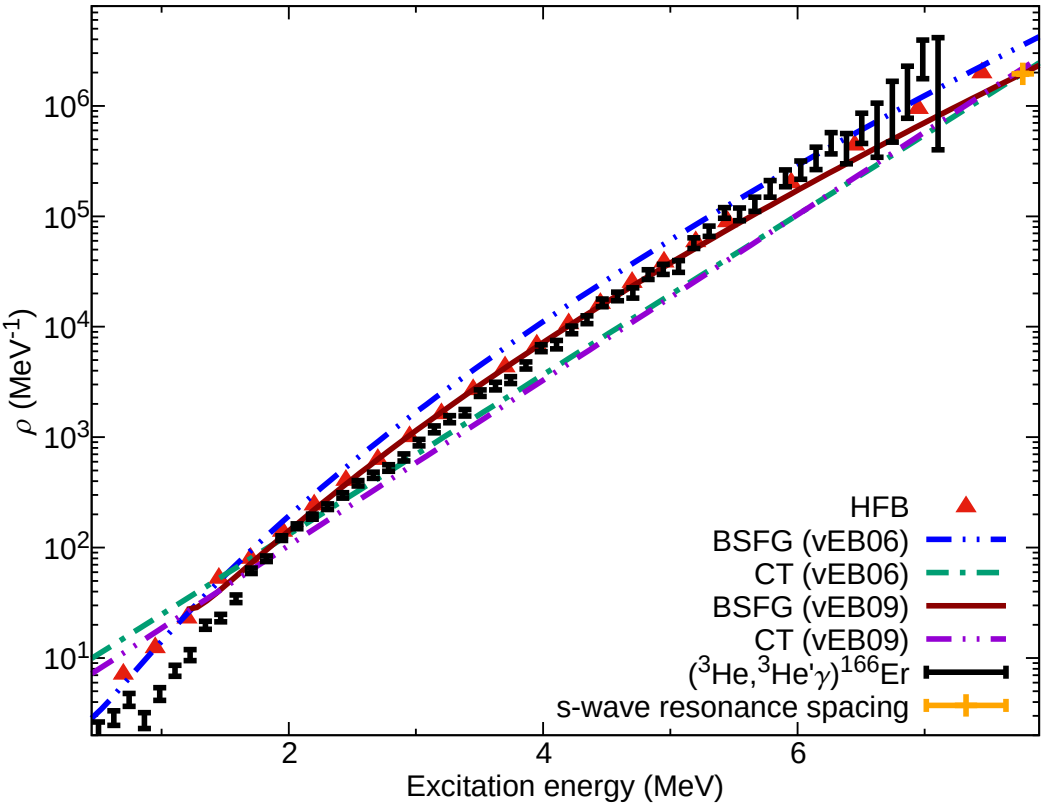

Figure 1.1: Spin- and parity-summed LD models tested for ^{168}Er. The red triangles correspond to the microscopic HFB calculations [19]. BSFG and CTF models are shown for two different parametrizations of the spin cut-off parameter σ - parametrization denoted as vEB06 is taken from [17] and the vEB09 version is from [18]. The normalization to the s-wave resonance spacing yields different total $\rho(e)$ for the same model (BSFG or CTF). The experimental LD data for ^{166}Er extracted by the Oslo method [20] are marked with black points. The s-wave resonance spacing point was converted to the summed LD using the spin distribution $f(J,\sigma)$ with σ from [18].

The obtained parity dependence follows Eq. (1.4) with the asymmetry disappearing at $E = 3\,\mathrm{MeV}$.

1.4 Experimental Information on Level Density

There are two experimental methods providing us with LDs in the continuous energy region below neutron separation energy. The first consists of measuring the neutron evaporation spectra from reactions induced by neutrons, protons, and α particles. Analysis of the experimental cross sections and their comparison with Hauser-Feshbach statistical calculations determines the absolute values of the LD, as it is one of the key ingredients in these calculations. For the majority of the analyzed nuclei [25, 26] LD is consistent with the BSFG model, while several closed-shell nuclei with $A \approx 208$ demonstrate better agreement with the CT formula [27].

The second experimental technique to extract the LD together with the PSFs

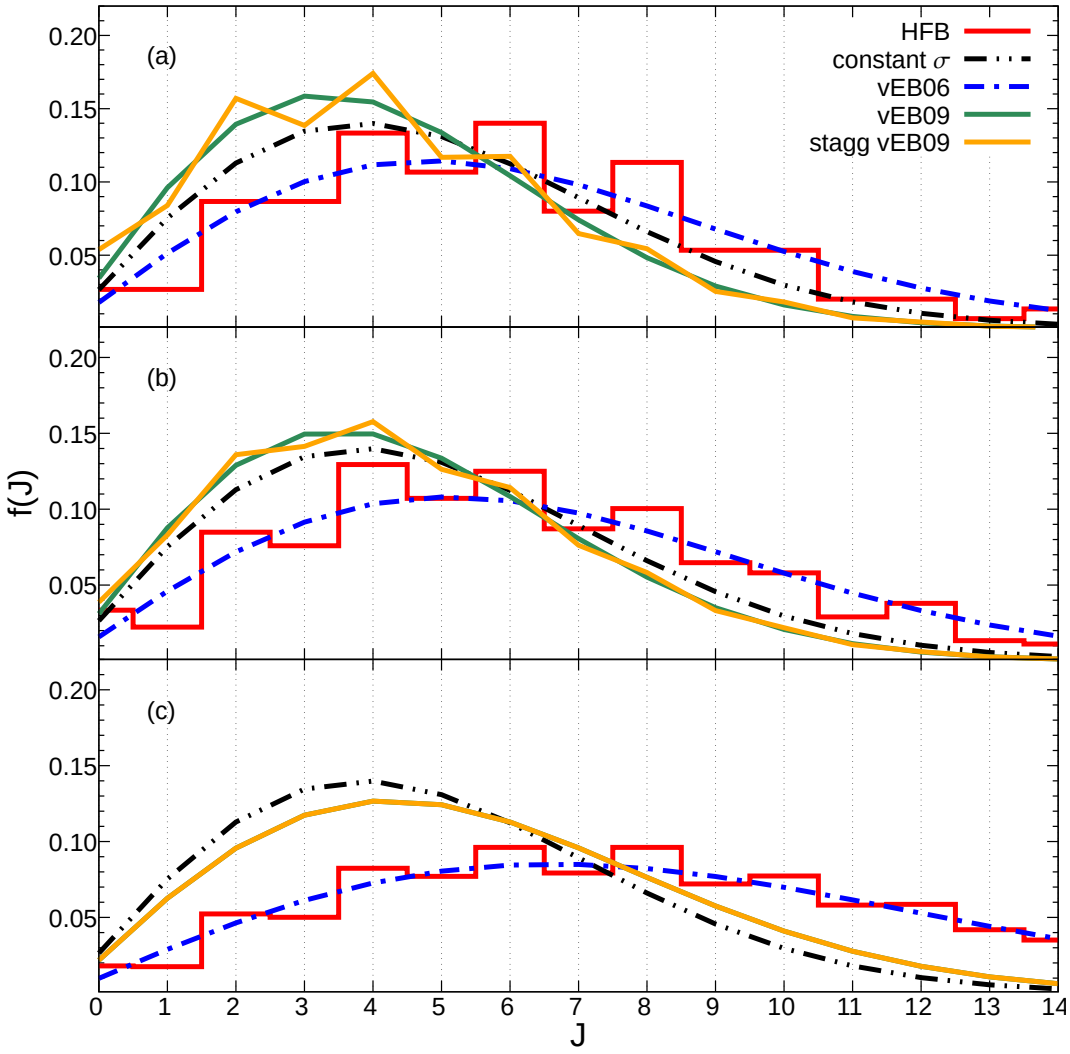

Figure 1.2: Spin distribution function $f(J,\sigma)$ (see Eq. (1.3)) at 2.4 MeV, 3.0 MeV and S_n excitation energy, respectively. $f(J,\sigma)$ is shown for HFB calculations and for different spin cut-off parameters σ - a constant σ, vEB06 parametrization taken from [17], vEB09 parametrization from [18] and vEB09 with staggering, which decreases linearly with increasing excitation energy and vanishes at 4 MeV (see Eq. (1.9)

.

is the so-called Oslo method [28, 29, 30]. It is based on reactions with charged particles, usually induced by ^{3}He, deuterons, and protons. The energy of the resulting charged particles is measured with silicon ΔE–E detectors, while the γ spectra are detected with a set of $LaBr_3$ scintillators (or the former setup with NaI detectors), and these two quantities are put into a coincidence. Extraction of the LD and PSFs is rather complicated and involves unfolding the spectra [31] and a fit of the resulting first-generation matrix of primary γ-ray transitions. This method does not yield absolute values of LD and PSFs, as there is an infinite set of solutions fitting the spectra. The slope and the absolute value of the LD energy dependence are obtained using external data on the number of low-lying

levels, neutron resonance spacing, and average radiative width. Oslo method was used to analyse a variety of rare-earth nuclei including ^{166,167}Er [32, 20].

2. Photon Strength Functions

Photon strength functions characterize average electromagnetic properties of excited nuclei and together with the level density serve as an important input to nuclear reaction model calculations as well as simulations of the γ decay. This chapter provides a brief overview of quantities describing the probability of electromagnetic transitions, the definition of PSF, and presents PSFs models for relevant multipolarities.

2.1 Introduction of PSFs

2.1.1 Probability of Electromagnetic Transitions

The *partial γ-decay width* $\Gamma_{\alpha\gamma\beta}$ determines the probability of an electromagnetic transition from the initial state $|\alpha\rangle = |E_\alpha, J_\alpha, \pi_\alpha\rangle$ to the final state $|\beta\rangle = |E_\beta, J_\beta, \pi_\beta\rangle$ via emission of a photon with $E_\gamma = E_\alpha - E_\beta$. It can be expressed as a sum of contributions from different types X (electric or magnetic) and multipolarities L ($L = 1, 2, 3...\infty$) of the electromagnetic transitions:

$$\Gamma_{\alpha\gamma\beta} = \sum_{X=el.,mag.} \sum_{L} \Gamma^{(XL)}_{\alpha\gamma\beta} \tag{2.1}$$

and $\Gamma^{(XL)}_{\alpha\gamma\beta}$ is given as:

$$\Gamma^{(XL)}_{\alpha\gamma\beta} = \frac{8\pi(L+1)}{L[(2L+1)!!]^2}\left(\frac{E_\gamma}{\hbar c}\right)^{2L+1} B(XL, \alpha \to \beta) \tag{2.2}$$

where $B(XL, \alpha \to \beta)$ is the *reduced transition probability for deexcitation* that is proportional to the transition electromagnetic operator $\mathcal{M}^{(XL)}$:

$$B(XL, \alpha \to \beta) = \frac{1}{2J_\alpha + 1} |\langle \beta J_\beta \| \mathcal{M}^{(XL)} \| \alpha J_\alpha \rangle|^2 \tag{2.3}$$

According to the detailed–balance principle, we can relate reduced matrix elements for deexcitation and the inverse process – photoexcitation

$$|\langle \beta J_\beta | \mathcal{M}^{(XL)} | \alpha J_\alpha \rangle|^2 = |\langle \alpha J_\alpha | \mathcal{M}^{(XL)} | \beta J_\beta \rangle|^2 \tag{2.4}$$

as well as the reduced transition probability for the deexciation with the reduced transition probability for photoexcitation:

$$B(XL, \alpha \to \beta) = \frac{2J_\beta + 1}{2J_\alpha + 1} B(XL, \beta \to \alpha) \tag{2.5}$$

and consequently express the partial γ-decay width $\Gamma^{(XL)}_{\alpha\gamma\beta}$ as a function of the *photoabsorption cross section* $\sigma^{(XL)}_{\beta\gamma\alpha}(E_\gamma)$:

$$\Gamma^{(XL)}_{\alpha\gamma\beta} = \frac{E_\gamma^2}{(\pi\hbar c)^2} \frac{2J_\beta + 1}{2J_\alpha + 1} \sigma^{(XL)}_{\beta\gamma\alpha} \tag{2.6}$$

2.1.2 Selection Rules

In reality, not all multipolarities L contribute to the sums in Eq. (2.1). The multipolarities of the allowed transitions $|\alpha\rangle \rightarrow |\beta\rangle$ follow the Wigner-Eckart theorem:

$$|J_\beta - J_\alpha| \leq L \leq |J_\beta + J_\alpha| \tag{2.7}$$

As a result of the system Hamiltonian commutating with the parity operator, we can also derive selection rules for parities of the initial and final states that give nonzero contribution for electric and magnetic transitions:

- $(-1)^L \pi_\alpha \pi_\beta = 1$ for electric transitions
- $(-1)^{L+1} \pi_\alpha \pi_\beta = 1$ for magnetic transitions

In practice, the most contributing types and multipolarities XL of PSFs are $E1$ (electric dipole), $M1$ (magnetic dipole) and $E2$ (electric quadrupole).

2.1.3 Average Quantities

At higher excitation energies it becomes difficult to observe transitions from/to individual levels, therefore we need to use the average partial γ-decay width $\overline{\Gamma}^{(XL)}_{\alpha\gamma\beta}$ instead of Eq.(2.2) and the average reduced transition probability for deexcitation $\overline{B}(XL, \alpha \rightarrow \beta)$. Fermi's golden rule implies that $\overline{B}(XL, \alpha \rightarrow \beta)$ is inversely proportional to the LD of the initial state $\rho(E_\alpha, J_\alpha, \pi_\alpha)$, because the sum of transition rates around initial state $|\alpha\rangle$ is expected to be constant independently of the number of levels. As a result $\overline{\Gamma}^{(XL)}_{\alpha\gamma\beta} \sim 1/\rho(E_\alpha, J_\alpha, \pi_\alpha)$. Instead of $\overline{\Gamma}^{(XL)}_{\alpha\gamma\beta}$, Bartolomew [33] introduced the so-called *photon strength function* to describe the distribution of average transition probability between levels:

$$f^{(XL)}(E_\gamma) = \frac{\overline{\Gamma}^{(XL)}_{\alpha\gamma\beta} \rho(E_\alpha, J_\alpha, \pi_\alpha)}{E_\gamma^{2L+1}} \tag{2.8}$$

as a function of the transition energy E_γ.

Similarly as in Eq. (2.6), $\overline{\Gamma}^{(XL)}_{\alpha\gamma\beta}$ can be related to the energy smoothed photoabsorption cross section $\overline{\sigma}^{(XL)}_{\beta\gamma\alpha}$:

$$\overline{\Gamma}^{(XL)}_{\alpha\gamma\beta} \rho(E_\alpha, J_\alpha, \pi_\alpha) = \frac{E_\gamma^2}{(\pi\hbar c)^2} \frac{\overline{\sigma}^{(XL)}_{\beta\gamma\alpha}}{2L+1} \tag{2.9}$$

which combined with Eq. (2.8) leads to an alternative definition of the PSF:

$$f^{(XL)}(E_\gamma) = \frac{1}{(\pi\hbar c)^2} \frac{\overline{\sigma}^{(XL)}_{\beta\gamma\alpha}}{(2L+1) E_\gamma^{2L-1}} \tag{2.10}$$

where $\overline{\sigma}^{(XL)}_{\beta\gamma\alpha}$ is supposed to depend only on the photon energy E_γ and not on the properties of the initial state. This expectation is known as the Brink hypothesis [34] and is based on the assumption that the collective vibrations are independent of intrinsic nuclear motion.

2.2 Electric Dipole PSF

In 1947 Baldwin and Klaiber [9, 35] observed a broad resonance above the neutron separation energy in the photoabsorption cross section. This resonance was already predicted a few years prior as a result of collective vibrations of proton and neutron fluids induced by incoming radiation. Protons and neutrons move with mutually opposite phases, therefore this motion has electric dipole character and the observed structure is called the *Giant Electric Dipole Resonance*.

There exist two macroscopic models explaining the GEDR motion. Steinwedel–Jensen model [36, 37] assumes vibration of proton and neutron fluid within a fixed surface and the energy of the GEDR centroid is proportional to $A^{-1/3}$. On the other hand, Goldhaber–Teller model [38] describes it as an oscillation of a proton incompressible sphere against a neutron incompressible sphere. The resulting GEDR center follows $A^{-1/6}$ dependence. Experimental analysis of photoneutron cross section data [39] for spherical nuclei suggests GEDR position in the form:

$$E_G = 31.2A^{-1/3} + 20.6A^{-1/6} \tag{2.11}$$

The width of the GEDR in spherical nuclei ranges from $\Gamma_G \approx 4 - 8\,\mathrm{MeV}$ [40] and systematic analysis of the photoneutron cross section data yields the expression $\Gamma_G = 0.026E_G^{1.9}$ [41]. The GEDR strength is approximated by the Thomas-Reiche-Kuhn (TRK) sum rule [42]:

$$\int_0^\infty \sigma_{\mathrm{tot}}^{(E1)}(E_\gamma)\,dE_\gamma \approx 60\frac{NZ}{A} \quad \mathrm{MeV}\cdot\mathrm{mb} \tag{2.12}$$

which expresses the total integrated cross section for the electric dipole photoabsorption process. In heavy nuclei with $A > 100$, experimental data show a 10-30 % increase compared to TRK rule caused by the meson-exchange contributions [43, 40]. It is assumed that the $E1$ transitions dominate over other types near the maximum of the GEDR and it is safe to consider $\sum_{XL}\sigma_{\mathrm{tot}}^{(XL)} = \sigma_{\mathrm{tot}}^{(E1)}$ in this region.

In the case of the axially symmetric deformed nuclei, photoabsorption measurements [39] indicate splitting of the GEDR into two resonances, which is a consequence of vibrations along the symmetry axis of the nucleus and perpendicular to it.

2.2.1 Phenomenological Models of Electric Dipole PSF

The most commonly used model of $E1$ PSF above S_n is the *Standard Lorentzian* (SLO) model adopting the Lorentz form of the photoabsorption cross section in Eq. (2.10). The PSF is given by:

$$f_{\mathrm{SLO}}^{(E1)}(E_\gamma) = \frac{1}{3(\pi\hbar c)^2}\sigma_G\Gamma_G\frac{E_\gamma\Gamma_G}{(E_\gamma^2 - E_G^2)^2 + E_\gamma^2\Gamma_G^2} \tag{2.13}$$

where E_G, Γ_G, σ_G are the energy, width of the resonance (both usually expressed in MeV) and the cross section at the maximum of the resonance (expressed in mb), respectively. $E1$ PSF for well-deformed nuclei is given by a superposition of two resonances with the form in Eq. (2.13) and two sets of parameters

$\{E_{G_i}, \Gamma_{G_i}, \sigma_{G_i}\}_{i=1}^{2}$. For simplicity, all formulas with $f^{(E1)}$ in this subsection are given with only one resonance term, while the sum of two resonances is used in our simulations.

Albeit the SLO model agrees well with photoabsorption data in the vicinity of GEDR for medium and heavy nuclei [39, 44, 43] it shows inadequacy to describe region below the S_n. Measurements of (n, γ) reactions yield disagreement for a variety of spherical nuclei [44, 45] and together with the results of ^{143}Nd$(n, \gamma\alpha)$ [46, 47, 48] indicate a possible dependence on the excitation energy E. These data also pointed out a nonzero limit for $E_\gamma \to 0$ for levels with a nonzero nuclear temperature T of the final level. The nuclear temperature is usually expressed as:

$$T = \sqrt{\frac{E - \Delta_p}{a}} \tag{2.14}$$

where a is the level density parameter (see Eq. (1.5)) and Δ_p is the pairing correction.

Kadmenskij, Markushev and Furman introduced a model known as the *KMF model* employing the above-mentioned features based on the Fermi-liquid theory of finite systems together with semi-microscopic shell model. It considers the GEDR width $\Gamma_G(E_\gamma, T)$ dependent on the nuclear temperature:

$$\Gamma_G(E_\gamma, T) = \frac{\Gamma_G}{E_G^2}(E_\gamma^2 + 4\pi^2 T^2) \tag{2.15}$$

and the $E1$ PSF has a form:

$$f_{\mathrm{KMF}}^{(E1)}(E_\gamma, T) = \frac{1}{3(\pi\hbar c)^2} F_K \sigma_G \Gamma_G \frac{E_G \Gamma_G(E_\gamma, T)}{(E_\gamma^2 - E_G^2)^2} \tag{2.16}$$

where the Fermi liquid parameter $F_K = 0.7$ [49, 21] is adopted.

The model was originally proposed for spherical nuclei, however, it is often used for well–deformed ones as well. From Eq. (2.16) it is apparent that the formula diverges at $E_\gamma = E_G$ and thus it is not applicable near the GEDR centroid.

Analyses of γ spectra from the Oslo Cyclotron laboratory often adopt KMF model with a constant temperature T as $E1$ PSF [50, 51, 52, 20, 53]. We performed also simulations employing this model, hereupon denoted as the KMF-T.

Later, Chrien [54] proposed the *Generalized Lorentzian* (GLO) model for spherical nuclei with a formula valid for the whole energy range that combines both previous approaches:

$$f_{\mathrm{GLO}}^{(E1)}(E_\gamma, T) = \frac{1}{3(\pi\hbar c)^2} \sigma_G \Gamma_G \left[\frac{E_\gamma \Gamma_G(E_\gamma, T)}{(E_\gamma^2 - E_G^2)^2 + E_\gamma^2 \Gamma_G^2(E_\gamma, T)} + F_K \frac{\Gamma_G(E_\gamma = 0, T)}{E_G^3} \right] \tag{2.17}$$

where $\Gamma_G(E_\gamma, T)$ has the form of Eq. (2.15) and T is given by Eq. (2.14). For $E_\gamma \ll E_G$ the KMF shape dominates, while the SLO dependence is granted near the GEDR peaks.

Another model employing the width $\Gamma_G(E_\gamma, T)$ dependent on the energy and temperature is the so–called *Lorentzian with energy-dependent width* (ELO)

model [55]:

$$f_{\mathrm{ELO}}^{(E1)}(E_\gamma, T) = \frac{1}{3(\pi\hbar c)^2}\sigma_G\Gamma_G\frac{E_\gamma\Gamma_G(E_\gamma, T)}{(E_\gamma^2 - E_G^2)^2 + E_\gamma^2\Gamma_G^2(E_\gamma, T)} \tag{2.18}$$

which adopts the SLO formula of PSF in Eq. (2.13) and $\Gamma_G(E_\gamma, T)$ from Eq. (2.15).

There exist several other models with PSF similar to Eq. (2.18) and a different form of $\Gamma_G(E_\gamma, T)$ dependence on the nuclear temperature, specifically *Generalized Fermi Liquid* [56], *Hybrid model* [57] and a family of *Modified Lorentzian* (MLO) models [58]. Detailed description can be found in Ref. [21]. The recent reference PSF database [59] also proposes the *Simplified Modified Lorentzian* (SMLO) model, the calculated $E1$ PSF is available for all nuclides across the nuclear chart.

In an attempt to achieve better compatibility for deformed nuclei, a phenomenological modification of the width (2.15) with ad hoc empirical parameters k and $E_{\gamma 0}$ was introduced by Kopecky, Uhl and Chrien [60]:

$$\Gamma_G(E_\gamma, T, k) = \left[k_0 + \frac{E_\gamma - E_{\gamma 0}}{E_G - E_{\gamma 0}}(1 - k_0)\right]\frac{\Gamma_G}{E_G^2}(E_\gamma^2 + 4\pi^2T^2) \tag{2.19}$$

where $E_{\gamma 0} \approx 4.5$ MeV is recommended [61]. The width is enhanced at $E_\gamma = E_{\gamma 0}$ with respect to Eq. (2.15) if $k > 1$. The value of the enhancement factor k was obtained by analysis of energy dependencies of (n, γ) cross sections and γ-ray spectra, adjustments of the calculated average radiative widths and also average resonance capture (ARC) data were taken into account. In our simulations we treat k as a free parameter, as the recommended value depends strongly on the adopted model of LD and PSF.

Inserting the width $\Gamma_G(E_\gamma, T, k)$ in the form of Eq. (2.19) into the GLO PSF formula (2.17) yields the so-called *Enhanced Generalized Lorentzian* (EGLO) model [60]. The recommended k for EGLO $E1$ PSF combined with BSFG LD model from ARC compilation reaches a maximum $k = 2.5$ for $A = 160$ [61].

Finally, the so-called *Modified Generalized Lorentzian* (MGLO) model was proposed [62] by using the width in Eq. (2.19) with PSF formula in the form:

$$f_{\mathrm{MGLO}}^{(E1)}(E_\gamma, T, k) = \frac{\sigma_G\Gamma_G}{3(\pi\hbar c)^2}\left[\frac{E_\gamma\Gamma_G(E_\gamma, T, k)}{(E_\gamma^2 - E_G^2)^2 + E_\gamma^2\Gamma_G^2(E_\gamma, T, k)} + F_K\frac{\Gamma_G 4\pi^2T^2}{E_G^5}\right] \tag{2.20}$$

and the second term in the brackets can be rewritten as $F_K\Gamma_G(0, T, 1)/E_G^3$. The MGLO model is an alternative to the EGLO one with a similar high energy behavior of the decay of highly excited states. On the contrary, the MGLO has a smaller preference for low-energy transitions than the EGLO model. The MGLO model with $k \approx 1.5 - 2$ is comparable to the KMF model.

A resonance in $E1$ PSF below S_n at $E_\gamma \approx 6 - 9\,\mathrm{MeV}$ has been reported in measurements for many nuclei. This structure is usually referred to as a pygmy resonance. Due to no indications of its presence in the region of well-deformed rare-earth nuclei, it was not tested in the simulations for ^{168}Er.

Comparison of the SLO, KMF, MGLO ($k = 3$) and EGLO ($k = 3$) can be found in Fig. 2.1. Except for the SLO model, all of these models are temperature dependent, therefore we show two curves corresponding to the primary transitions ($T = \sqrt{(S_n - E_\gamma - \Delta_p)/a}$) and transitions to the ground state ($T = 0$). We

adopted the parametrization of the GEDR from Dietrich and Berman compilation [43].

2.2.2 Microscopic Models of Electric Dipole PSF

Microscopic models of $E1$ PSF are derived especially within the quasiparticle random–phase approximation (QRPA) approach. S. Goriely *et al.* performed calculations of $E1$ PSF employing the axially symmetric deformed QRPA framework based on D1M Gogny interaction [63], which can be found in the reference PSF database [59] and hereafter will be referred to as QRPA+D1M. The derived PSFs include free parameters that can be adjusted on available low-energy experimental data such as those obtained with the Oslo method or the average radiative widths.

Furthermore, predictions on $E1$ strength were calculated within the QRPA approach using Skyrme effective interaction [64, 65, 66] with parametrizations SkI3 [67], SkM* [68], SLy6 [69], SVbas [70] and SkP [71]. For more details, see App. B.

2.3 Magnetic Dipole PSF

Below the S_n, also magnetic dipole ($M1$) transitions play an important role in the γ decay of well-deformed rare-earth nuclei. Experimental information on $M1$ strength especially in this region is nearly comparable to that of $E1$. There are two dominant types of collective excitations - the *Scissors Mode* (SM) and the *Spin-Flip Mode* (SF). Furthermore, there is an evidence about a strong increase of the $M1$ PSF for very low E_γ, which is usually referred to as the *Low-Energy Enhancement* (LEE).

2.3.1 Scissors Mode

A collective magnetic dipole mode was theoretically predicted using the geometrical two–rotor model by Hilton [72] and later by Lo Iudice and Palumbo [73] as well as within the framework of proton–neutron interacting model by Iachello [74]. The name of this mode originates from the graphical representation as a scissors-like counterrotation of the proton versus neutron fluid. The first experimental observation was performed with high–resolution electron inelastic scattering in ^{156}Gd [75] and subsequently in ^{154}Sm, ^{158}Gd, ^{164}Dy, ^{168}Er and ^{174}Y [76] . It was confirmed that SM dominating at energy $E_{\mathrm{SM}} \approx 3\,\mathrm{MeV}$ is a general feature for a large variety of heavy deformed nuclei.

These findings were verified with another experimental technique - nuclear resonance fluorescence (NRF) [77], which employs (γ, γ') reaction. The experimental data from even-even nuclei showed fragmentation of the transition strength at energy $E_{\mathrm{SM}} \approx 3\,\mathrm{MeV}$, where the SM is expected to dominate [78]. NRF was a successful tool to examine SM of the majority of stable even-even rare-earth nuclei. Moreover, the SM was observed in several heavy odd-mass nuclei as well.

A systematic study of the SM via the NRF experiments in well-deformed even-even rare-earth nuclei suggested the total transition strength $\sum B(M1) \approx$

$3\,\mu_N^2$ [79] and the spectra measured in the chain of ^{148,150,152,154}Sm isotopes [80] revealed its proportionality to the square of the nuclear deformation δ^2.

The NRF measurement of erbium isotopes derived the total $M1$ transition strength summed in the energy range $E_{\rm SM} = 2.4 - 3.7\,$MeV in ^{166,168,170}Er to be $\sum B(M1) = 2.67(19), 2.82(42)$ and $2.63(16)\,\mu_N^2$ [77], respectively. A newer measurement [81] derived a larger strength $\sum B(M1) = 3.56(15)\,\mu_N^2$ for ^{168}Er in the range $E_{\rm SM} = 2.7 - 3.7\,$MeV. The total strengths in the $E_{\rm SM}$ energy range for even-even Er isotopes ^{166,168,170}Er thus fit very well into the systematics of even-even rare-earth nuclei.

The situation is more complicated for odd-A nuclei. In particular, ^{167}Er(γ,γ') measurement presented much larger total transition strength $\sum B(M1) = (3.14 \pm 1.12)\mu_N^2$ [82] than all values reported previously for odd-A nuclei. Moreover, the $M1$ strength was found to be spread over a large interval of $E_{\rm SM} = 2.5 - 4.3\,$MeV. Generally, while in even-even nuclei the strength wass usually distributed over a few states corresponding to $\Gamma_{\rm SM} \approx 200 - 300\,$keV, the spreading width in odd-A nuclei is very variable.

The NRF and elastic scattering experiments observe SM excitations above the ground state, while there are two types of indirect experiments used to study properties of the SM in the quasicontinuum - measurements of neutron capture (n,γ) reaction and p, d,α and ^{3}He induced reactions using the Oslo Method (see Sec. 1.4). The SM is represented by a resonance structure that is described by a Lorentzian (2.13) with a set of parameters $(E_{\rm SM}, \Gamma_{\rm SM}, \sigma_{\rm SM})$ and the total strength $\sum B$(SM) is proportional to the product of $\Gamma_{\rm SM}$ and $\sigma_{\rm SM}$. Two-step γ cascade (TSC) spectra following the neutron capture of thermal neutrons were studied for ^{163}Dy, where a 3 MeV bump was detected and interpreted as a SM resonance with the integrated $M1$ strength $6.2\,\mu_N^2$ [83, 84]. An important outcome of this experiment was the observation of the SM not only in the ground-state transitions but also transitions to the excited states [84]. The MSC spectra obtained the resonance neutron capture on a chain of Gd isotopes yielded 2–3 times larger SM strength in odd-A ^{157,159}Gd [62] than even–even neighboring ones [85, 86]. MSC spectra for ^{162}Dy [87] suggest the SC strength consistent with the above-mentioned MSC data for even-even Gd isotopes, while even a larger strength was reported for ^{164}Dy [87]. Integrating the summed $M1$ strengths in ^{162,164}Dy [87] from MSC over the energy range $2.7 - 3.7\,$MeV, which can be directly compared to those obtained from the NRF measurements, yields fully compatible values.

Oslo method derived the SM parameters for a large variety of rare-earth nuclei, including a chain of Dy isotopes [51, 52, 53]. The deduced $M1$ strength $7.8 \pm 2.2\,\mu_N^2$ for ^{163}Dy [53] is consistent with the TSC measurement mentioned above. Furthermore, this strength was comparable to SM strength in neighboring even–even Dy nuclei measured at the Oslo Cyclotron Laboratory [53], which was $6.8(8)\,\mu_N^2$ for ^{162}Dy and $5.3(10)\,\mu_N^2$ for ^{164}Dy. The Oslo-derived total strength in ^{162}Dy is significantly higher than $2.3 - 4.3\,\mu_N^2$ [87] from the MSC, while comparable to the ^{164}Dy value of $5.3 - 7.5\,\mu_N^2$ [87]. Later the ^{162,164}Dy Oslo data were reanalyzed [88], yielding significantly smaller values of $\sum B$(SM) (see Fig. 6.16).

Analysis of the γ-ray spectra with the Oslo method in ^{166,167}Er [20] reported a pygmy resonance in both isotopes at energy $\approx 3\,$MeV, which was interpreted as a low-energy $E1$ enhancement. The authors however note that "the possibility

that it on the contrary is of $M1$ character cannot be excluded".

2.3.2 Spin-flip Mode

Inelastic proton scattering experiments confirmed the orbital nature of the scissors mode and were later used to study spin magnetic dipole strength in deformed heavy nuclei that is shifted to higher energies. It is essential for the SF analysis to use a probe sensitive to the spin part of the nuclear current. Scattering of200 MeV protons at very small forward angles showed presence of a double–peak structure at energies ≈ 6 and 8.5 MeV and width ≈ 2 MeV in ^{154}Sm, ^{158}Gd and ^{168}Er [89]. Positions of the SF centers of gravity for non-spherical heavy nuclei follow $\approx 34A^{-1/3}$ and $44A^{-1/3}$ dependency [79]. On the contrary, measurements of inelastic electron scattering on ^{156}Gd and ^{168}Er provided no evidence of a concentrated $M1$ strength in the $4-10$ MeV region of excitation energy.

Parameters of the SF mode were also examined in ARC experiments which proposed center position $E_{\mathrm{SF}} \approx 41A^{1/3}$ and width $\Gamma_{\mathrm{SF}} \approx 4$ MeV [90], this global parametrization is also recommended in the RIPL-3 database [21]. However, due to low value of S_n in rare-earth nuclei, ARC is not particularly sensitive to the specific shape of $M1$ SF strength. Nonetheless, results from several ARC experiments on rare–earth nuclei determined the ratio $f^{(E1)}/f^{(M1)} \approx 7$ at $E_\gamma = 7$ MeV [91].

2.3.3 Low-energy Enhancement

In the rare-earth region, a strong LEE was firstly revealed in the PSFs extracted from $(p, d\gamma)^{151,153}$Sm measurement [92] with the Compton-shielded Ge clover detectors, using the Oslo method. Later measurement at the same facility also reported LEE in $(p, d\gamma)^{147,149}$Sm [93]. On the other hand, the $M1$ PSF deduced from $(d, p\gamma)^{151,153}$Sm measured at the Oslo Cyclotron Laboratory [94] did not show any evidence of LEE. Similar enhancement was previously reported in lighter nuclei, where the shell model calculations [95, 96, 97, 98] predict its $M1$ nature and an exponential decrease with the γ-ray energy. Furthermore, the authors of [96] suggest presence of the $M1$ LEE throughout the nuclear chart.

Similarly to $E1$ PSF, the $M1$ PSF was derived based on QRPA+HFB calculations using D1M Gogny interaction [63, 59]. For erbium, dysprosium and gadolinium isotopes the $M1$ PSF shape indicates presence of a concentrated strength near the positions of the expected SM and SF resonances - just above $E_\gamma \approx 2$ MeV and in the region $E_\gamma \approx 6-8$ MeV. In addition, $M1$ PSF was calculated within the QRPA approach using Skyrme effective interaction [64, 65, 66].

In our simulations, we usually adopt a composite $M1$ PSF as a sum of contributions from a single-particle (SP) model, scissors mode, and spin-flip mode $f^{(M1)} = f_{\mathrm{SP}} + f_{\mathrm{SM}} + f_{\mathrm{SF}}$. The SP model f_{SP} corresponds to a a constant function, independent of the E_γ. f_{SM} is given by the Lorentzian form (2.13) and f_{SF} is expressed as a sum of two Lorentzians from (2.13). We assume a strict validity of the Brink hypothesis, i.e. the $M1$ PSF only depends on the γ-ray energy E_γ. In reality, the $M1$ PSF may have a more complicated form, which we try to mimic

within an easily adjustable composite model. The composite $M1$ PSF given by the sum of SM and SF contribution is plotted in Figs. 2.1- 2.2.

2.4 Electric Quadrupole PSF

Besides the dipole transitions that dominate the γ decay, it is affected by $E2$ transitions as well. The $E2$ strength was experimentally studied mainly by measuring the inelastic scattering of charged particles [99] because the corresponding cross section can be expressed as a sum of multipole contributions. These reactions using electrons, protons, and α-particles as probes demonstrated the resonance-like behavior of $E2$ strength [100] that was theoretically explained as an isoscalar *Giant Electric Quadrupole Resonance* (GEQR). This collective motion is interpreted as a surface oscillation of protons moving together with neutrons. The position E_G of the GEQR [40] is very close to the GEDR and the systematic for the width Γ_G and the cross section at the maximum σ_G was proposed as [101]:

$$\begin{aligned} E_G &= 63A^{-1/3} \quad \text{MeV} \\ \Gamma_G &= 6.11 - 0.012A \quad \text{MeV} \\ \sigma_G &= 0.00015\frac{Z^2E_G^2}{A^{1/3}\Gamma_G} \quad \text{mb} \end{aligned} \tag{2.21}$$

Moreover, an isovector giant quadrupole resonance was observed at higher energy $\approx 130A^{-1/3}$ [40], but its effect on γ transitions below 10 MeV is negligible.

Only a small number of primary $E2$ transitions was observed in (n,γ) reactions with thermal and resonance neutrons [101]. The ratio of average partial radiation width of $E1$ transitions compared to the $E2$ one deduced from ARC measurements is $\Gamma^{(E1)}/\Gamma^{(E2)} \geq 100$ [91]. This is consistent with the results on primary γ-rays from (n,γ) experiments.

$E2$ PSF can be represented by a Lorentzian shape using formula (2.13) with the parameters taken from (2.21, which is recommended in [21] or it is often adopted as a single-particle model with $f^{(E2)}$ being a constant function. It is important to note that while at higher energies below the S_n the $E2$ transitions do not play a major role, they significantly affect transitions at low excitation energies due to structural effects. However, in our approach, the statistical model assumptions are not applied in this region.

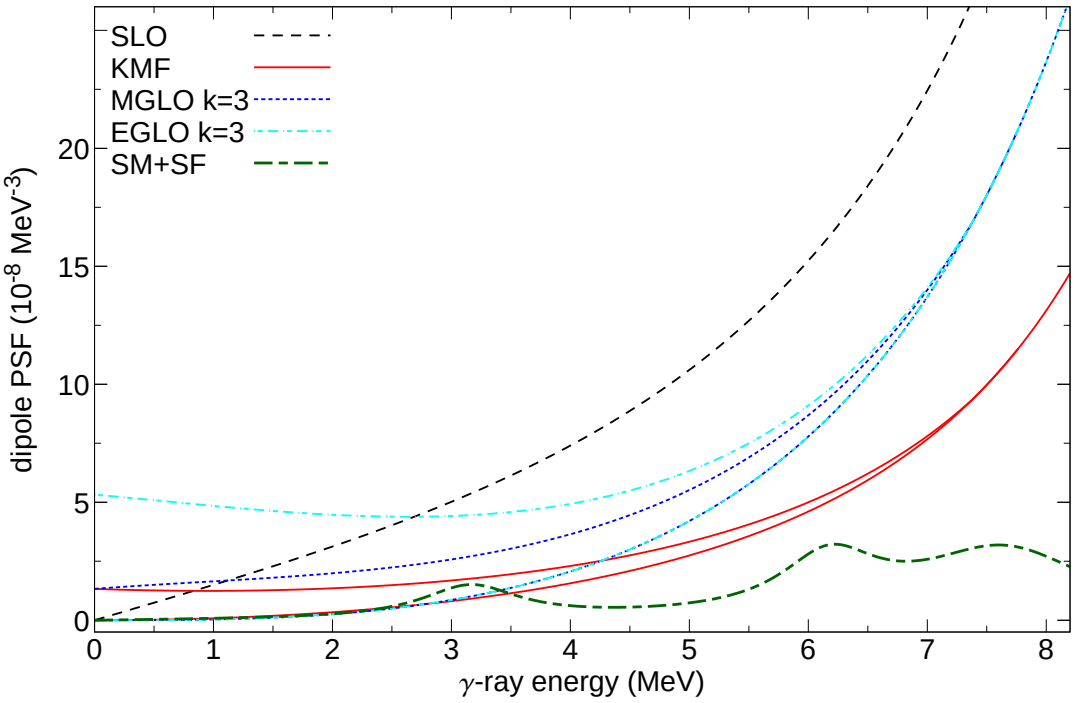

Figure 2.1: Dipole PSF models for ^{168}Er tested in our simulations. The upper curves for the KMF, MGLO ($k = 3$) and EGLO ($k = 3$) correspond to the primary transitions ($T = \sqrt{(S_n - E_\gamma - \Delta_p)/a}$), while the lower curves represent the transitions to the ground state ($T = 0$). The parameters of the SM are $E_{\rm SM} = 3.2\,$MeV, $\Gamma_{\rm SM} = 1.0\,$MeV and $\sigma_{\rm SM} = 0.5\,$mb. The parameters of the SF are $E^{(1)}_{\rm SF} = 6.2\,$MeV, $\Gamma^{(1)}_{\rm SF} = 1.0\,$MeV, $\sigma^{(1)}_{\rm SF} = 1.7\,$mb and $E^{(2)}_{\rm SF} = 7.7\,$MeV, $\Gamma^{(2)}_{\rm SF} = 1.8\,$MeV, $\sigma^{(2)}_{\rm SF} = 2.6\,$mb.

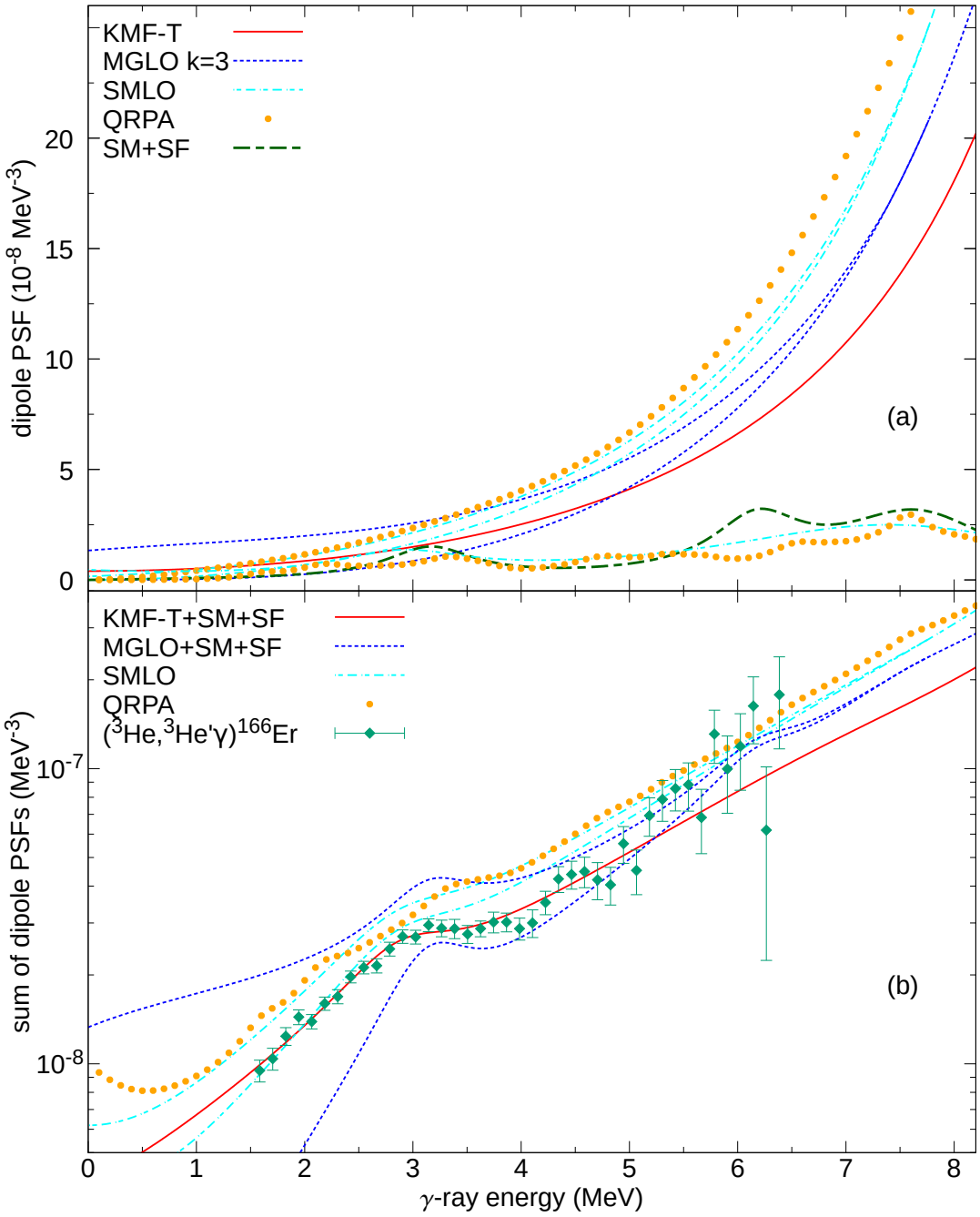

Figure 2.2: Panel (a): Dipole photon strength functions models tested for ^{168}Er. The SMLO and the QRPA+D1M calculations are available in the reference PSF database [59]. The KMF-T model with $T = 0.31$ was proposed for ^{166}Er measurement using the Oslo method [20]. There are two $E1$ PSF curves for the SMLO and MGLO ($k = 3$) model, the upper curves correspond to the primary transitions ($T = \sqrt{(S_n - E_\gamma - \Delta_p)/a}$), while the lower curves represent the transitions to the ground state ($T = 0$). The lowest SMLO curve represents the $M1$ PSF. The upper QRPA curve corresponds to the $E1$ PSF, the lower one represents the $M1$ PSF. The SM+SF parameters are the same as plotted in Fig. 2.1. Panel (b): Sum of dipole photon strength function models. Parameters for the KMF-T+SM+SF model combination are taken from Ref. [20], as well as the measured data points for (^{3}He,^{3}He'γ)^{166}Er.

3. Simulations of Statistical γ Decay

One of the methods to study level density and photon strength functions that govern the γ decay is to analyze experimental γ-ray spectra in comparison with their simulated counterparts. A Monte Carlo code DICEBOX was developed by F. Bečvář [102] to generate γ-cascade deexcitation within the statistical model of γ decay. Its major advantage is the correct treatment of partial radiation widths which are expected to follow a χ^2 distribution with one degree of freedom, in nuclear physics referred to as the Porter-Thomas (PT) distribution (see Sec. 4.2.1). In a number of works [59], the DICEBOX has been proved as a useful tool to describe γ decay following the slow neutron capture and it is freely available online at [103].

The original algorithm of [102] was enhanced with a concept of *nuclear supra-realizations* [87], the detailed description can be found in Sec. 3.2. To directly compare experimental spectra with their simulated counterparts, it is necessary to simulate also the response of the detector system, see Sec. 3.4.

3.1 Assumptions

The algorithm is based on the validity of the statistical model of γ decay and other simplifying assumptions:

- Only electromagnetic channels, corresponding to deexcitation via γ rays and internal conversion electrons are taken into account and particle channels have negligible effect.
- Each cascade starts from a well-defined single initial level a_1 with known energy, spin and parity E_1, J_1, π_1.
- Below a certain excitation energy, hereafter denoted as the *critical energy* $E_{\rm crit}$, a complete experimentally determined level scheme is known, including level energies, spins, parities and branching intensities of the depopulating transitions.
- Above the $E_{\rm crit}$ individual levels and their properties are calculated by a random discretization of an *a priori* known LD formula $\rho(E, J, \pi)$.
- The partial radiation width Γ_{ab} for a transition $a \to b$ from the level a with $E_1 \geq E_a > E_{crit}$ to the level b is given by a sum of contributions:

$$\Gamma_{ab} = (1+\alpha_{ab}) \sum_{XL} \Gamma^{(XL)}_{a\gamma b} = \\ = (1+\alpha_{ab}) \sum_{XL} \left(y^{(XL)}_{ab}\right)^2 (E_a - E_b)^{2L+1} \frac{f^{(XL)}(E_a - E_b, \tau)}{\rho(E_a, J_a, \pi_a)} \quad (3.1)$$

in a general case where mixing of various types X and multipolarities L is allowed by selection rules. Here $f^{(XL)}$ is the corresponding photon strength function (as defined by Eq. (2.8)) depending on the γ-ray energy $E_\gamma = E_a - E_b$ and possibly on other variables τ and $\rho(E_a, J_a, \pi_a)$ is the LD at the initial energy E_a. The coefficient α_{ab} corresponds to the internal electron conversion. The quantities $y_{ab}^{(XL)}$ are random values independently drawn from a standard normal distribution $\mathcal{N}(0,1)$ that ensure the PT fluctuations of individual partial radiation widths $\Gamma_{ab}^{(XL)}$.

Theoretically, the summation in Eq. (3.1) goes over all allowed XL, while in reality only $E1$, $M1$ and $E2$ transitions are taken into account above the E_{crit} in our simulations. The only possible mixed transition is thus $M1$ + $E2$ and the corresponding internal conversion coefficient α_{ab} can be expressed as a function of a mixing ratio δ:

$$\alpha_{ab} = \frac{\alpha_{ab}^{(M1)} + \delta^2 \alpha_{ab}^{(E2)}}{1+\delta^2}, \quad \delta^2 = \frac{\Gamma_{a\gamma b}^{(E2)}}{\Gamma_{a\gamma b}^{(M1)}} \tag{3.2}$$

Consequently, the partial width from Eq. 3.1 for the mixed transition $M1$ + $E2$ is given as:

$$\Gamma_{ab}^{(M1+E2)} = (1+\alpha_{ab}^{(M1)})\Gamma_{a\gamma b}^{(M1)} + (1+\alpha_{ab}^{(E2)})\Gamma_{a\gamma b}^{(E2)} \tag{3.3}$$

- Partial radiation widths Γ_{ab} and $\Gamma_{a'b'}$ with $a \neq a'$ and $b \neq b'$ are not statistically correlated.

The resulting nuclear levels and partial radiation widths governing the transitions between these levels are hence produced by a random discretization of the given LD formula and drawn from the PT distributions with expectation values determined by the PSFs. In rare–earth nuclei, the set of levels below S_n usually includes $10^{10} - 10^{13}$ partial radiation widths and that amount can be problematic to store in the computer memory. This challenge is bypassed by the algorithm described in Sec. 3.3.

All the information about the levels below E_{crit} are taken from the ENSDF database [104]. If the experimental information on the contribution of the internal electron conversion is not known, it is computed using parameters from the BrIcc database [105].

3.2 Nuclear Realizations and Suprarealizations

A generated set of levels and their corresponding partial radiation widths as described in the previous section is hereafter called a *nuclear realization* (NR). In principle, there exists an infinite number of nuclear realizations.

In addition to the original work [102], a concept of *nuclear suprarealizations* (NSs) was introduced [87]. It was motivated by real behavior observed in the decay of neutron resonances. The only difference in the γ decay of individual resonances in the vicinity of the excitation energy E_1 are the partial radiation widths of the primary transitions, whereas the levels below E_1 and their partial radiation widths are identical.

In practical implementation, a nuclear suprarealization denoted as Ω_k is defined as a set of nuclear realizations $\{\omega_{ik}\}_{i=1}^{I}$. Within a given NS Ω_k, all the NRs $\omega_{ik}, i = 1...I$ consist of an identical set of levels and partial radiation widths except for the partial widths of the initial level. In other words, two NRs ω_{ik} and $\omega_{i'k}$ within a common NS Ω_k differ only by intensities of the primary transitions. Generally, there are infinite nuclear realizations ω_{ik} even within one fixed nuclear suprarealization Ω_k.

3.3 Algorithm

Electromagnetic cascades coming from the decay of a compound nucleus following the neutron capture are generated adopting the assumptions discussed above employing the Monte Carlo technique. The essential tool of this algorithm is a deterministic random number generator (RNG) which produces a sequence of quasi-random numbers that are predetermined by an adjustable parameter, referred to as a generator seed ζ. The random number drawn from a uniform distribution in the interval $[0, 1)$ which is not preset is hereafter denoted as $s_{(\bullet)}$. The scheme of the algorithm can be found in Fig. 3.3. The γ cascades are generated as follows:

1. The level density $\rho(E, J, \pi)$ is discretized to yield energies E_a, spins J_a and parities π_a of all individual levels a with $E_1 > E_a > E_{\text{crit}}$. Integrating the LD formula over the given energy bin provides the average number of levels involved. Within the statistical approach, these level numbers fluctuate around the average values and usually Poisson distribution is adopted in the simulations. In reality, the RMT theory predicts Wigner distribution of the nearest neighbor spacings between the levels in the statistical region, however, the level spacing in the low-energy region is better represented by the Poisson distribution. Due to larger fluctuations expected from the Poisson distribution than Wigner one, our fluctuation estimates may be slightly conservative.

2. A generator seed ζ_a is randomly ascribed to each level a with energy $E_a > E_{\text{crit}}$ and stored in the memory. Obtaining all partial radiation widths $\Gamma_{aa'}$ for a fixed level a is initialized only after the RNG is preset using the seed ζ_a. As the seeds are ascribed to all levels above E_{crit}, a set of partial radiation widths $\Gamma_{aa'}$ for transitions to all allowed final levels a' is known. The seeds thus uniquely determine the outcome of generating partial radiation widths, which presents the key ingredient to the algorithm.

3. The seed ζ_1 is ascribed to the initial capturing level, RNG is preset using the seed ζ_1 and a set of partial radiation widths $\Gamma_{1a'}$ for transitions $1 \to a'$ to all possible levels a' (where $E_{a'} < E_1$) is generated.

4. A total radiation width Γ_1 for the capturing level $a = 1$ is calculated as:

$$\Gamma_1 = \sum_{a'} \Gamma_{1a'} \tag{3.4}$$

A complete set of branching intensities $I_{1a'}$ for transitions initialized from the capture level is determined from:

$$I_{1a'} = \frac{\Gamma_{1a'}}{\Gamma_1} \tag{3.5}$$

and stored as a starting point of each cascade. The normalization condition $\sum_{a'>1} I_{1a'} = 1$ is fulfilled.

5. The initial capture level decays to a level a_1 which is determined by a random number s_1. The choice of level a_1 follows from the requirement:

$$\sum_{a'>1}^{a_1-1} I_{1a'} \leq s_1 < \sum_{a'>1}^{a_1} I_{1a'} \tag{3.6}$$

As a result, the level a_1 at energy E_{a_1} with spin J_{a_1} and parity π_{a_1} reached by the first γ-cascade step is determined.

6. If the energy E_{a_1} of a_1 level is above E_{crit}, a set of partial radiation widths $\Gamma_{a_1a'}$ for all allowed transitions $a_1 \to a'$ initialized from the given level a_1 is generated. Prior to this process the RNG is preset using the seed ζ_{a_1}. Corresponding total width Γ_{a_1} and a full set of branching intensities $I_{a_1a'}$ is calculated in the same fashion as listed in Item 4. If $E_{a_1} < E_{\text{crit}}$, the branching intensities $I_{a_1a'}$ are derived entirely from the experimental data.

7. Using the random number s_2 and a set of branching intensities $I_{a_1a'}$ a second intermediate level a_2 is chosen in the same way as described in Item 5.

8. The procedure outlined from the Items 5-7 repeats until the moment when n-th cascade step reaches the ground state. As an illustration in Fig. 3.3, the cascade reaches the ground state after 4 steps. After reaching the ground state, all the information characterizing a single cascade is available - energies E_{a_i}, spins J_{a_i} and parities π_{a_i} of all intermediate levels as well as the transition types X, multipolarities L and mixing ratios δ. This data set can be used to calculate any quantity of interest such as the γ-ray spectrum.

9. The modeling procedure described in Items 5-7 is repeated L times until satisfactory statistical accuracy of the desired quantity is achieved. Typically $L \approx 10^5$ within the given NR.

10. In order to estimate the influence of the PT fluctuations of the primary transitions, the algorithm steps in Item 3-9 are repeated I times to obtain a set of NRs $\{\omega_{ik}\}_{i=1}^{I}$ (see Sec. 3.2). For some quantities of interest, it is sufficient to model only one NR ω_{1k} within each NS Ω_k.

11. To assess the role of PT fluctuations of transition intensities below the initial capture level and fluctuations due to random discretization of the LD, the procedure in Item 1-9 is repeated K times to produce the full set $\{\omega_{ik}\}_{i=1,k=1}^{I,K}$.

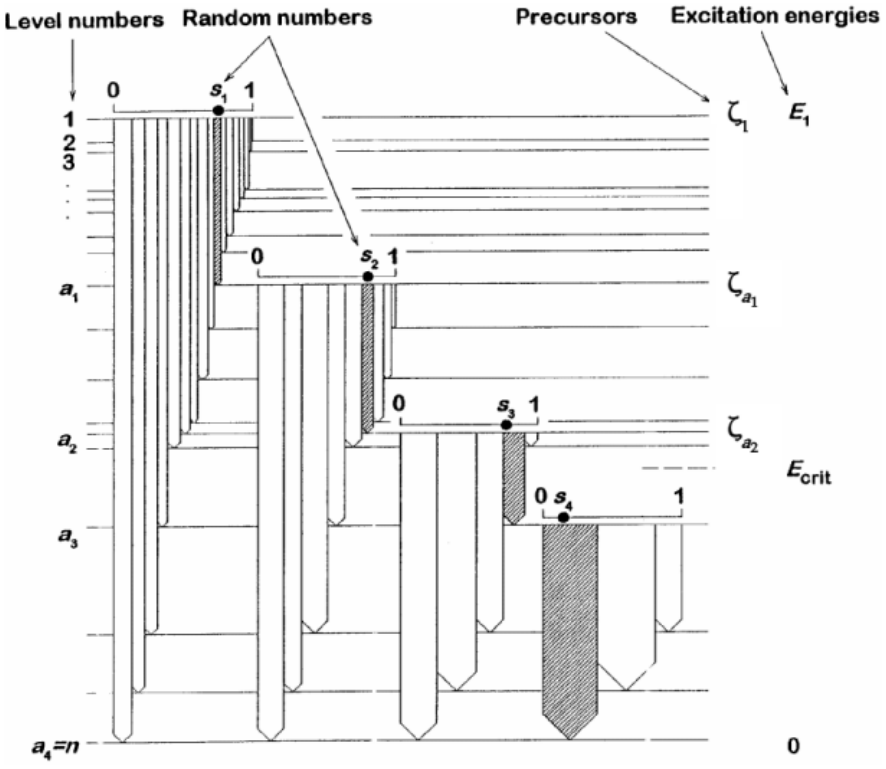

Figure 3.1: Schematic description of generating γ cascades with the DICEBOX algorithm. The involved levels are denoted as a_j, their energies E_j and their ascribed seeds as ζ_{a_j} [102].

3.4 Simulation of the Detector Response

Our goal is to directly compare experimental γ-ray spectra to simulated ones, thus it is necessary to feed the γ cascades produced by DICEBOX to the simulation of the detector response. The DANCE calorimeter is a rather complicated detection system consisting of 160 individual crystals and also other non-scintillating materials (see Chap. 5). A simulation of the DANCE array based on GEANT4 Monte Carlo code was created by M. Jandel *et al.* [106]. Simulated γ spectra were compared with measured data using radioactive sources ^{88}Y, ^{22}Na and ^{60}Co, and a good agreement was achieved [106]. DANCE-GEANT4 code is thus a highly accurate simulation to model the detector response to the simulated γ cascades.

4. Fluctuation Properties of Neutron Resonances

Measurements of (n, γ) reactions on heavy rare–earth targets with the DANCE detector allow us to observe individual s–wave resonances in the energy region up to hundreds of eV. Resonance sequences of a single spin J and parity π serve as unique data sets to test predictions of the random matrix theory, which aims to describe properties of chaotic quantum systems. Assuming the validity of the RMT has been widely used to test the completeness of resonance data or to determine the number of missing levels (see e.g. [107]).

This chapter addresses the main conclusions drawn from the RMT predictions of nuclear spectral properties, in particular concerning Gaussian orthogonal ensemble (GOE). A comprehensive review of the RMT concepts and status in nuclear physics can be found in [108, 109], hereafter we will restrict ourselves only to the introduction of fluctuation measures relevant to our study. In addition, we present methods how to test completeness or estimate the number of missing levels from simulations of GOE predictions.

4.1 Random Matrix Theory

In the 1960s Wigner [6, 7] introduced random matrices to nuclear physics, which was probably motivated by Bohr's compound nucleus model and his idea that nuclei display statistical properties at excitation energies of several MeV [3]. Bohr identified the positions of the resonances as eigenvalues of an unknown complicated Hamiltonian, for which calculating the energies of these excited states is not possible. Wigner's approach was not to calculate the individual spectra but to characterize spectra by their fluctuation properties as averages over the ensemble. Instead of an actual nuclear Hamiltonian, he considered an ensemble of Hamiltonians, each represented by a matrix. The ensemble is defined by a probability distribution for the matrix elements, which leads to the name random matrices.

Canonical RMT as developed by Wigner and Dyson [7] characterizes systems by their symmetry properties. Within the RMT one calculates the joint probability distribution of the eigenvalues and from here determines spectral fluctuation measures of interest, which can be compared with actual fluctuation properties from the experiment. Generally, RMT contains several input parameters, in the case of spectral fluctuations the parameter is the average nuclear level spacing. The predicted fluctuation measures are scaled by the average level spacing and hence are parameter-free.

4.2 Gaussian Orthogonal Ensemble

Various nuclear global symmetries lead to different canonical ensembles of random matrices. In particular, the *Gaussian Orthogonal Ensemble* characterizes systems that are invariant under time reversal - such as nuclei - and it was very successful in describing properties of nuclear resonances. We consider real and symmetric

matrices in a Hilbert space of dimension N, representing systems with time-reversal invariance, and their reality and symmetry is preserved under orthogonal transformations of the basis. Their elements are independent random variables drawn from Gaussian probability distribution. According to Wigner, nuclear levels of a single spin and parity display the same ordering behavior as eigenvalues of large $N \times N$ GOE matrices.

The mean level density $\rho(E)$ of a GOE spectrum with N levels is approximately semicircular:

$$\rho(E) = \begin{cases} \frac{1}{2\pi}\sqrt{4N - E^2}, & \text{for } |E| \leq 2\sqrt{N}. \\ 0, & \text{otherwise.} \end{cases} \tag{4.1}$$

except for a few levels at the extreme edges on both sides. The mean level spacing is defined as $D(E) = \rho(E)^{-1}$. On the other hand, the mean s–wave level density in nuclei can be considered constant over the few keV region of experimental comparison. As a result, it is necessary to perform a transformation to a new energy parameter such that the average level spacing is constant, i.e. unfolding the spectra.

We present two categories of GOE fluctuations measures that are useful in the experimental analysis of neutron resonances - the first corresponding to fluctuations of neutron widths, while the second category contains several measures related to fluctuations of the resonance positions.

4.2.1 Fluctuations of Neutron Widths

For a single resonance of the energy E_R, the capture cross section as a function of the neutron incident energy E can be expressed with the Breit-Wigner formula:

$$\sigma_\gamma(E) = \pi\lambda\!\!\!^{-2} \frac{g\Gamma_n\Gamma_\gamma}{(E - E_R)^2 + \frac{1}{4}\Gamma^2} \tag{4.2}$$

where $\lambda\!\!\!^{-} = \hbar/(\sqrt{2mE})$ is the de Broglie wavelength of the incoming neutron and m is the neutron reduced mass. The total resonance width:

$$\Gamma = \Gamma_n + \Gamma_\gamma \tag{4.3}$$

is given as a sum of the neutron width Γ_n and the radiative width Γ_γ. The strength of the resonance is characterized by the resonance integral A_γ defined as:

$$A_\gamma = \int_{-\infty}^{+\infty} \sigma_\gamma(E) dE \tag{4.4}$$

which yields

$$A_\gamma = 2\pi^2\lambda\!\!\!^{-2} g \frac{\Gamma_n\Gamma_\gamma}{\Gamma} \tag{4.5}$$

where g is the statistical factor:

$$g = \frac{2J + 1}{2(2I + 2)} \tag{4.6}$$

depending on the spin of the target nucleus I and the resonance spin J.

Removing the energy dependence of the neutron widths Γ_n of s–wave resonances, we obtain the *reduced neutron widths* $\Gamma_n^0 = \Gamma_n/\sqrt{E_R}$, where E_R is the resonance energy. The experimentally observed values of Γ_n^0 show large fluctuations from one resonance to another in the same nucleus. This can be explained within the GOE approach, where eigenvalues and eigenfunctions are uncorrelated random variables and for $N \to \infty$ the projections of the eigenfunctions onto an arbitrary vector in Hilbert space have a Gaussian distribution centered at zero. These projections correspond to the reduced widths amplitudes and since one measures reduced widths, not the amplitudes, the resulting Γ_n^0 distribution is χ^2 with one degree of freedom [110], in nuclear physics referred to as the Porter-Thomas distribution:

$$P(y) = \frac{1}{\sqrt{2\pi y}} \exp\left(-\frac{y}{2}\right) \tag{4.7}$$

where $y = \Gamma_n^0/\langle\Gamma_n^0\rangle$ is a dimensionless variable with $\langle\Gamma_n^0\rangle$ being the average neutron reduced width. Within the RMT calculations, the parameter $\langle\Gamma_n^0\rangle$ is an input parameter not predicted by the RMT.

The PT distribution of Γ_n^0 has been analyzed and verified for many data sets, see for example the study of single–spin s–wave resonances in even–even nuclei [111]. On the other hand, there are also indications of violation, thus it is still an object of further studies [112, 113].

An ideal data set for the test of PT distribution is complete (no missing resonances) and pure (sequences of resonances of a single spin and parity). Unfortunately, every experiment has a lower limit for observing resonances. The quantity that determines the observability is the resonance integral A_γ (see Eq. (4.4)) and for the weakest resonances in the rare-earth region, it holds that $\Gamma_n \ll \Gamma_\gamma$, where $\Gamma_\gamma \sim 0.1\,\mathrm{eV}$ and it is fluctuating only by a few percent, thus $A_\gamma \sim g\Gamma_n$. The exact form of the observability threshold is usually not known, as it depends on the experimental conditions.

4.2.2 Fluctuations of Resonance Positions

For a measured sequence of N resonances, the average spacing $\langle D\rangle$ is calculated as:

$$\langle D\rangle = \frac{\Delta E}{N-1} \tag{4.8}$$

where ΔE is the energy difference between the last and the first resonance.

There are several different measures that can be employed for fluctuations of resonance positions. The first and straightforward measure is the distribution of spacings between the neighboring levels (resonances), hereafter denoted as *nearest neighbor spacing distribution* (NNSD). Distribution $P(s)$ of the nearest level spacings D_i depends on the ratio $s = D_i/\langle D\rangle$. It cannot be given in a closed form, however, an excellent approximation is given by the so-called Wigner surmise [7]:

$$P(s) = \frac{\pi}{2} s \exp\left(-\frac{\pi}{4}s^2\right) \tag{4.9}$$

An important implication of the GOE theory is the level repulsion between any pair of levels, which is displayed in Eq. (4.9) as a linear increase with s for a small value of s. In the case of random, uncorrelated levels the NNSD would follow the Poisson distribution and there would be no level repulsion. The exact expression of $P(s)$ for a random matrix utilizing a rapidly converging infinite product was numerically calculated by Gaudin [114]. Its comparison with Wigner's hypothesis gave a very good agreement.

Validity of the Wigner surmise (4.9) was tested against the so-called nuclear data ensemble (NDE), containing 157 proton and 1250 neutron resonance energies obtained from 30 sequences in 27 different medium–weight and heavy nuclei (see Fig. 4.1). Each sequence was scaled to the same average level spacing. A remarkable agreement was found between fluctuation properties predicted from GOE and NDE energies [115]. The results also suggest that this is a universal phenomenon.

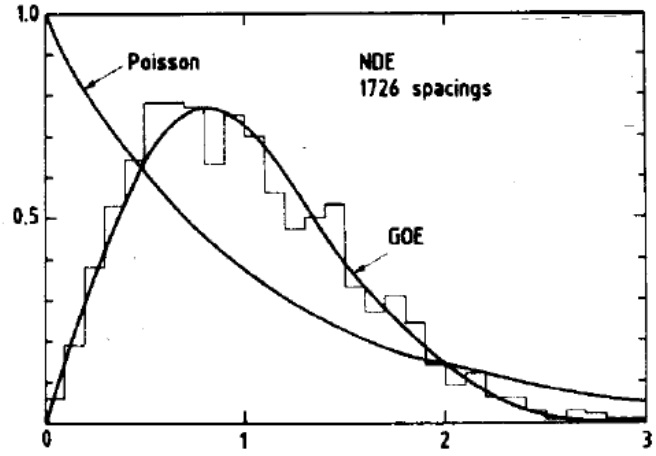

Figure 4.1: The nearest neighbor spacing distribution for NDE containing 1726 spacings D_i (the histogram) as a function of $s = D_i/\langle D\rangle$, where $\langle D\rangle$ is the mean level spacing. For comparison, the predicted distribution from GOE and Poisson distribution are shown as solid lines. Figure taken from Ref. [116].

The NNSD does not include information about correlations between level spacings. Such information is contained in two other fluctuation measures described below - correlation coefficient $\rho(D_i, D_{i+1})$ and Δ_3 statistic.

The correlation coefficient between the adjacent nearest neighbor spacings $\rho(D_i, D_{i+1})$ defined as:

$$\rho(D_i, D_{i+1}) = \frac{\sum_i (D_i - \langle D_i\rangle)(D_{i+1} - \langle D_{i+1}\rangle)}{[\sum_i (D_i - \langle D_i\rangle)^2 \sum_i (D_{i+1} - \langle D_{i+1}\rangle)^2]^{1/2}} \tag{4.10}$$

is sensitive to correlations between levels with energies E_i and E_{i+2}. GOE prediction for a large number of levels yields $\rho(D_i, D_{i+1}) \approx -0.27$ [117], indicating anticorrelation between adjacent level spacings.

The Δ_3 statistic is a measure of the long-range order of level positions. GOE theory suggests that resonances of the same spin and parity tend to be equally spaced, which manifests as a crystalline-like long-range order [118]. Dyson and Mehta [118] developed the Δ_3 statistic as a measure of the mean square deviation

of a staircase plot $N(E)$ from a best–fitting straight line:

$$\Delta_3(L) = \frac{1}{L} \min_{\alpha,\beta} \int_{E_i}^{E_i+L} [N(E) - AE - B]^2 dE \tag{4.11}$$

on a given length L and $N(E)$ is the cummulative number of levels in the energy range $(E_i, E_i + L)$. For a large number of levels N the expected value (ensemble average) of Δ_3 approaches [118]:

$$\Delta_3(N) \approx \frac{1}{\pi^2}[\ln N - 0.0687] \tag{4.12}$$

with a constant standard deviation of 0.11. The Δ_3 statistics has been often utilized to test fluctuation properties of measured neutron resonances, see for example [117, 119, 120, 107].

4.3 Simulations of GOE Predictions

4.3.1 Reduced Neutron Widths

The analysis of the PT distribution and estimating the number of sub-threshold s–wave resonances is traditionally performed using $g\Gamma_n^0$. It is usually assumed that the observability threshold can be reasonably approximated with a power law function in neutron energy.

To determine the number of sub-threshold resonances, we simulate random sequences of resonances within the statistical approach - i.e. using the average s–wave resonance spacing D_0 and the s–wave neutron strength function S_0, which follow:

$$S_0 = \frac{\langle g\Gamma_n^0 \rangle}{D_0} \tag{4.13}$$

The generated resonance positions follow predictions from the GOE, see the following Sec. 4.3.2. Each resonance from the 10^4 simulated resonance sequences is assigned $g\Gamma_n^0$ following the PT distribution, assuming the average value $\langle g\Gamma_n^0 \rangle$ given by Eq. (4.13) and the resulting $g\Gamma_n^0$ are compared to the experimental threshold.

4.3.2 Statistics Related to Resonance Positions

In order to compare experimental resonance sequences with GOE predictions, a large number (typically ≈ 5000) of randomly generated GOE matrices is diagonalized and the eigenvalues are unfolded for the Wigner's semicircle law (see Eq. (4.1)) to have a constant level density. The matrices are large enough to get individual sequences of the same length as in the experiment and up to $\approx 30\%$ longer. The average simulated spacing is adjusted to be consistent with the experiment. For the resonance sequences of mixed spin, several reasonable values of the mixing parameter are tested and the results are independent of the exact parameter value.

The calculation of the Δ_3 statistic from Eq. (4.11) is not practical, as except for the maximum value of L, there is no unique definition of Δ_3. Therefore we use the $\Delta_3(L)$ statistic as a function of an integer L:

$$\Delta_3(L) = \left\langle \min_{a,b} \frac{1}{E_{i+L-1} - E_i} \int_{E_i}^{E_{i+L-1}} dE \Big[\mathcal{N}(E) - aE + b \Big]^2 \right\rangle_i , \tag{4.14}$$

where E_i is the energy of the i^{th} resonance, $\mathcal{N}(E)$ us the cumulative number function and a,b are parameters of the linear fit to the function $\mathcal{N}(E)$. For a given L, the minimization is performed separately for each allowed value of i, which satisfies the condition $1 \leq i$ and $(i + L - 1) \leq L_{\max}$. The Δ_3 is calculated for $L = 3, ..., L_{\max}$, where $L_{\max}$ is the length of the sequence. For more details about obtaining artificial resonance sequences from generated GOE matrices, see Ref. [113].

5. Experiment

Neutron capture experiment $^{167}\mathrm{Er}(n,\gamma)^{168}\mathrm{Er}$ was performed with the neutron spallation source located at Los Alamos Neutron Science Center (LANSCE) [121] at LANL. Protons accelerated to the energy of 800 MeV strike the tungsten target at the repetition rate 20 Hz, producing neutrons that are moderated by a backscatter water moderator [122]. The resulting neutrons energies range from thermal up to a few MeV. The DANCE detector is positioned at a 20.28 m flight path from the neutron source.

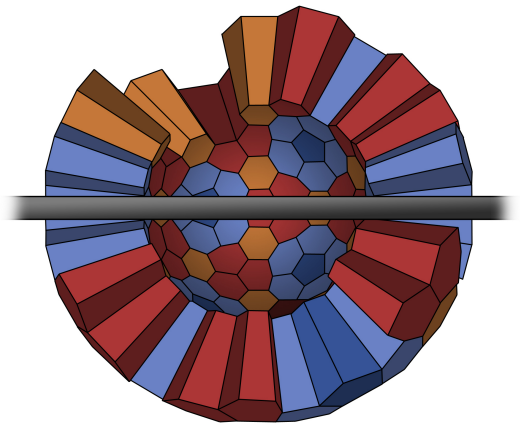

Figure 5.1: DANCE detector visualized with the GEANT4 simulation toolkit. The measured sample is positioned in the centre, two crystals are left out to make space for the neutron beam pipe.

DANCE [123, 124] is a highly efficient scintillator calorimeter consisting of 160 BaF_2 crystals covering a solid angle of almost 4π, see Fig. 5.1. Its main purpose is the measurement of γ rays following the neutron capture on small samples, both stable and radioactive. The solid angle coverage is essential to achieve the detection efficiency as close to 100% as possible. A full 4π array would include 162 crystals, in reality, two of them are removed to make space for the neutron beam pipe. Each BaF_2 crystal is covered in a PVC foil and glued to a photomultiplier tube and this array is supported by an aluminum structure. To reduce the flux of scattered neutrons hitting the crystals, a ^{6}LiH shell of 6 cm thickness is placed between the sample and the crystals. Three detectors are monitoring the neutron flux: a gas-filled BF_3+Ar proportional counter, an n-type surface barrier Si detector, and a ^{235}U fission chamber.

The DANCE efficiency for detecting a single 1 MeV γ ray is $\approx$ 86% [106], while the energy resolution for 1 and 6 MeV γ rays is 16% and 7%, respectively. Specifics about the energy calibration of the array are discussed in Sec. 5.1.2.

5.1 Data Acquisition and Data Processing

The scintillation light emitted by the BaF_2 crystals is formed by a slow component (decay time $\approx$ 600 ns) and a fast component (decay time $\approx$ 600 ps). Signals from

the DANCE crystals are read out using 16-channel CAEN VX1730 digitizers with 14-bit resolution, running 500 mega samples per second [125, 126]. All DANCE crystals trigger independently and are validated by a timing gate of a fixed width starting ≈ 100 μs before the arrival of protons on the tungsten target. The width of this gate (typically a few milliseconds) determines the range of neutron energies recorded by the acquisition system.

To reduce the amount of stored data, only a fraction of the information available from the full waveforms is recorded. For each crystal, the leading edge timestamp, long and short charge integrals, and 80-ns partial waveforms covering the rise of the signal are recorded for the offline analysis. The short integral, containing the bulk of the fast component in BaF_2 is 12 ns wide, while the long integral is 1000 ns long and it measures the slow component. The energy deposited in each DANCE crystal is calculated as the difference between the slow and fast components. It is important to note that while the digitizer is integrating the fast and slow components of the most recent trigger, it cannot trigger again. This feature introduces dead time into the system, for more details see Sec. 5.2.3. After extracting the essential waveform information, the data are transferred to the master computer using the MIDAS (Maximum Integrated Data Acquisition System) [127] approach.

All γ-ray signals that arrive within a preset coincidence window (usually 5–20 ns) form an *event*. This event is characterized by the number of crystals that fired, the energy deposited in each crystal, and the total energy E_Σ as a sum of all crystal energies. The simulations and calibration measurements demonstrate that an emitted γ ray does not necessarily deposit its full energy in a single crystal, but due to Compton scattering it is rather in several, often neighboring crystals. The number of crystals that fire during a single γ cascade detection is thus higher than the true multiplicity. This effect is taken into account by introducing the so-called *cluster*, which is a set of adjacent crystals that are hit during an event. The number of clusters that are hit within an event is the *cluster multiplicity* M, which is closer to the real multiplicity than the crystal one. After clusterization, we obtain individual energies deposited in M clusters.

5.1.1 Experimental Background

There are several background sources for the DANCE detector array, which can be grouped into three major types [124]:

1. Time-independent background, which is not correlated with the time structure of the neutron beam. This includes intrinsic radioactivity of the BaF_2 crystals originating from the α decay of ^{226}Ra, which is a chemical homologue of Ba. α particles display a different intensity ratio between the fast and slow scintillation component than γ rays (see Fig. 5.2), therefore background from the α activity can be rejected from the comparison of the fast and slow integrals. The spectrum of the emitted α particles is used for energy calibration, see Sec. 5.1.2. In addition to α radiation, there is also β^- activity contribution from the ^{226}Ra decay chain, which dominates for the lower multiplicities $M < 3$ and lower energies.

2. Time-dependent background correlated with the time structure of the beam,

but not scaled with the sample placed in the beam. It is related to the γ rays originating from the interaction of the primary proton beam with the tungsten spallation target, preceding the produced neutrons (the so-called γ-flash). In order to shield the DANCE detector from this contribution, the flight path is designed to view the upper-tier water moderator, not directly the tungsten target. Moreover, interactions of neutrons with the material of the beam pipe cause that γ rays are the second most prominent component of the beam after neutrons. This background is significantly reduced by placing Kapton foils as windows dividing the beam pipe.

3. Sample-related background, that is related to three processes:

   - (n, n) reactions, where scattered neutrons are captured in the BaF_2 crystals or surrounding materials. The Q-values of the capture reactions $^{135}Ba(n, \gamma)$ and $^{137}Ba(n, \gamma)$ are 9.1 and 8.6 MeV, respectively, which is usually higher than the Q-values of the reactions with the studied rare-earth isotopes. As already mentioned above, a 6 cm-thick ^{6}LiH shell is placed between the sample and the crystals causing the scattered neutrons to be attenuated due to $^{6}Li(n, \alpha)$ reaction.
   - Neutron capture on sample impurities, which is discussed specifically for Er measurement in Sec. 5.2.
   - Possible radioactivity of the sample, it is not the case of this study.

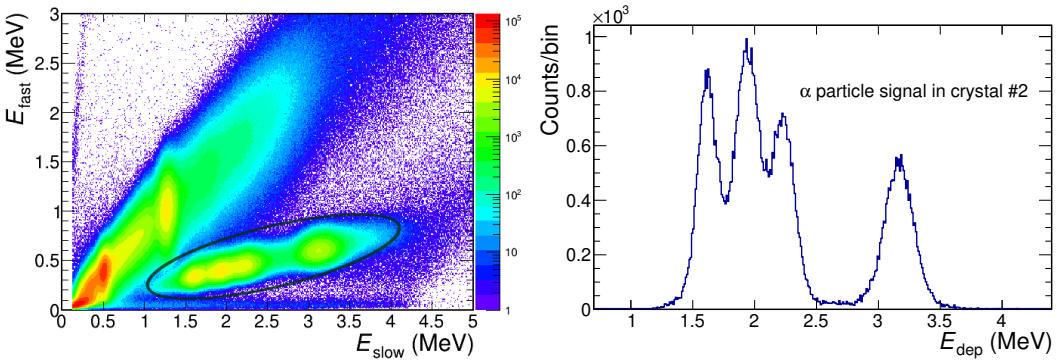

Figure 5.2: Left panel: Energy of the fast vs. slow component, the α particles (marked with a black ellipse) are discriminated against the γ-ray signals. Right panel: Deposited energy E_{dep} of the α particles in crystal 2.

5.1.2 Energy and Time Calibration

The BaF_2 crystals are temperature sensitive and small gain shifts have been observed over time. As a result, it is necessary to perform run-by-run correction to the detected energy based on α-decay signals that are distinguished from γ rays using pulse shape discrimination (see Fig. 5.2).

Shortly before the actual measurement of $^{167}Er(n, \gamma)$, the calibration measurement using radioactive sources ^{22}Na and ^{88}Y without the neutron beam was run. The first step of the calibration was utilizing the known γ-decay lines of these radioisotopes (see Fig. 5.3), which yielded the initial quadratic energy calibration

for each DANCE crystal. With this initial calibration applied, the α spectra for each crystal of the source runs were saved as a template. For the subsequent $^{167}\mathrm{Er}(n,\gamma)$ runs, the uncalibrated α spectra were fitted to these templates for each crystal to extract the energy calibration for a given run. An example of the α spectra for a specific run can be found in Fig. 5.2.

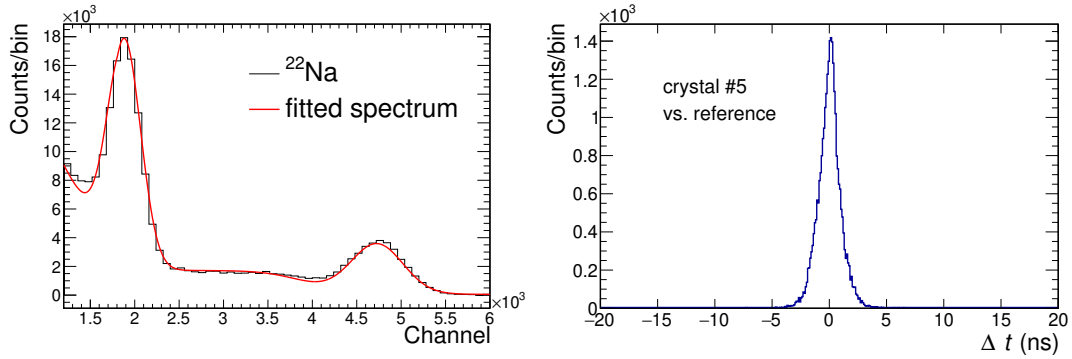

Figure 5.3: Left panel: The measured and fitted spectrum of ^{22}Na source γ-decay lines used for energy calibration. Right panel: Time alignment of the crystal 5 against the reference crystal.

The relative timing of all DANCE crystals slightly changes for each run as a result of the synchronization of the digitizers. All crystals thus need to be aligned with one another in time on a run-by-run basis, which is achieved by adjusting their time offsets such that there is a zero difference between Compton-scatter events in each pair of adjacent crystals. As we can see from Fig. 5.3, the alignment within a few ns is reached.

5.2 Specifics to Erbium Measurement and Experimental Spectra

The enriched Er sample was prepared at the Oak Ridge National Laboratory and its isotopic composition can be found in Tab. 5.1. The first measurement in 2018 was performed with the sample of 20.1 mg mass, while the additional measurement in 2019 used the same sample with its mass reduced by a factor of 4.

Sample	Mass	Isotope abundance (%)					
	(mg)	^{162}Er	^{164}Er	^{166}Er	^{167}Er	^{168}Er	^{170}Er
^{167}Er	20.1	0.02(3)	0.06(6)	2.94(11)	91.52(25)	5.15(11)	0.33(6)

Table 5.1: Mass and isotopic composition of the Er sample. Additional smaller-mass Er measurement was performed with a mass reduced by a factor of 4 to check the behavior of the strong resonances.

The signals were assumed to belong to the same event if they were detected within the preset 6 ns coincidence window. The time-of-flight (TOF) of the event

is determined by the difference between the timestamp of the first γ ray in the event and the recent timing signal of the proton pulse, immediately before it strikes the tungsten spallation target. The TOF is converted to corresponding neutron energy E_n using the geometrical flight-path length. Each event is characterized by the neutron energy E_n, the total deposited energy E_Σ, the cluster multiplicity M, and the set of individual energies deposited in M clusters $\{E_\gamma^{(i)}\}_{i=1}^{M}$.

5.2.1 Sum-energy and MSC Spectra

A part of the experimental E_n vs E_Σ spectrum is shown in Fig. 5.4. We can apply cuts on the above-mentioned experimental observables to draw spectra for a chosen quantity of interest. We define the E_n intervals to analyze events from the individual, well–resolved s–wave resonances. For these intervals, the spectra of sums of deposited energies for each cluster multiplicity M, hereafter denoted as the *sum-energy spectra*, are shown in Fig. 5.5.

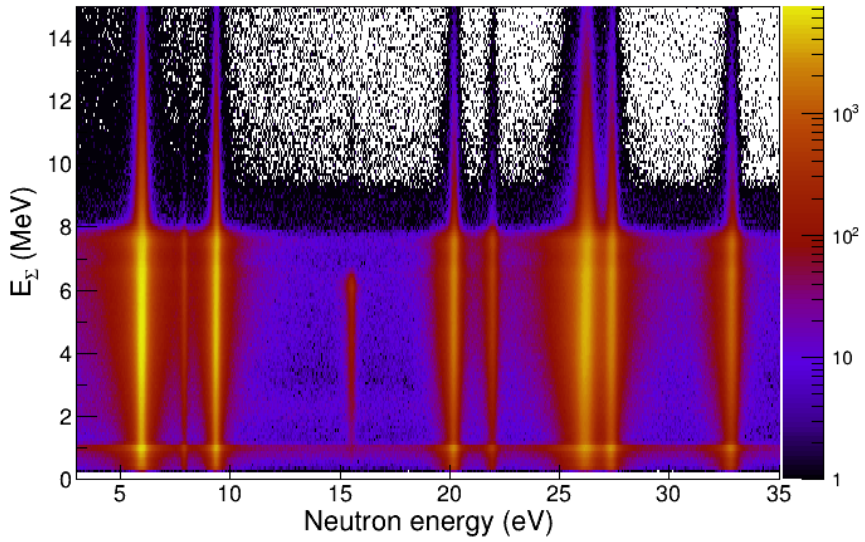

Figure 5.4: Experimental E_n vs E_Σ spectrum for $^{167}\mathrm{Er}(n,\gamma)^{168}\mathrm{Er}$ summed over all multiplicities. The resonance at 15.56 eV comes from the ^{166}Er impurity in the sample.

Each sum-energy spectrum consists of:

- The full-energy peak located in the vicinity of the neutron separation energy S_n, corresponding to the γ cascades where all the deposited energy was detected by the array.
- The low-energy tail, a continous part of the spectrum related to events where a part of the γ-ray energy escaped the detection.
- In the special case of $^{167}\mathrm{Er}(n,\gamma)$, we can also see a peak at $E_\Sigma \approx 6.6\,\mathrm{MeV}$ and a corresponding peak at $E_\Sigma \approx 1.1\,\mathrm{MeV}$. It results from the presence of an isomeric state at $E_{\mathrm{exc}} = 1.094\,\mathrm{MeV}$, whose lifetime is $\approx 100\,\mathrm{ns}$. It

is much longer than the coincidence window 6 ns, therefore the majority of the γ cascades decaying via this state is detected as two separate events, the cascade feeding the isomer (6.6 MeV peak) and the decay of the isomer (1.1 MeV peak).

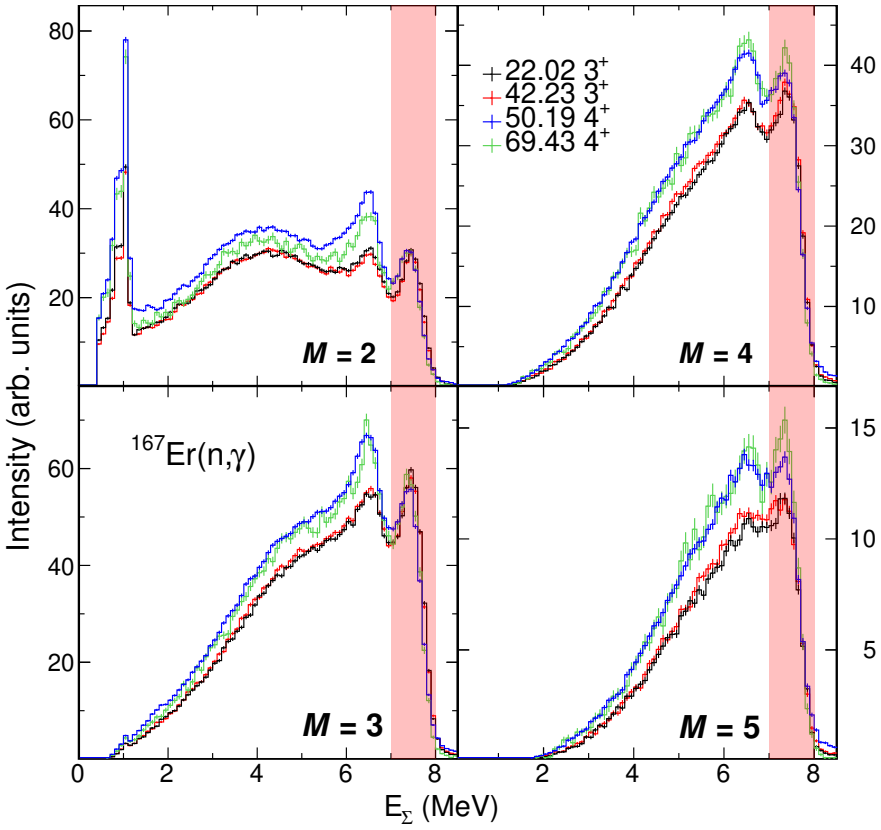

Figure 5.5: Experimental sum-energy spectra from two resonances of each spin, shown for multiplicities $M = 2 - 5$. The energy and spin of the resonance is indicated in the legend in top-right panel. The spectra are normalized in the same fashion as described in the text. The $E_\Sigma = 7 - 8$ MeV range used to construct the MSC spectra is illustrated as a red band.

The center of the full-energy peak is slighly shifted towards lower energy than S_n due to contribution of the electron conversion process that manifests in the transitions between low-lying levels. The sum-energy spectra in the region $E_\Sigma < 3$ MeV for lower multiplicities are influenced by the β^- activity in the crystals and the region above S_n is affected by the neutron capture on Ba isotopes or detector effects such as event pile-up, for more detail see Sec. 5.2.3.

The DANCE setup allows us to distinguish resonances from different isotopes if the difference in their S_n can be identified from the sum-energy spectra. An example of a parasitic resonance is observed in Fig. 5.4 at $E_n \approx 15$ eV, which clearly corresponds to a smaller S_n. This evidence is supported by Atlas [128] reporting a 15.56 eV resonance in ^{166}Er, which is one of the impurities in the sample composition (see Tab. 5.1).

For the analysis of LD and PSFs, we construct the so-called *multi-step cascade* (MSC) spectra corresponding mainly to events resulting from detection of complete γ cascades. We define a gate on E_Σ to cover events from the full-energy peak

and we construct the spectra of the γ-ray energies deposited in M clusters. For this purpose, only events from well–isolated resonances are chosen. The range in the E_Σ (usually referred to as the Q-value range) used in $^{167}\mathrm{Er}(n,\gamma)^{168}\mathrm{Er}$ measurement was $Q = 7 - 8\,\mathrm{MeV}$ to account for $S_n = 7.771\,\mathrm{MeV}$. By applying this Q-value range, we exclude events from a possible parasitic resonance if its $S_n < 7.0\,\mathrm{MeV}$, which holds for all Er impurities [128] listed in Tab. 5.1.

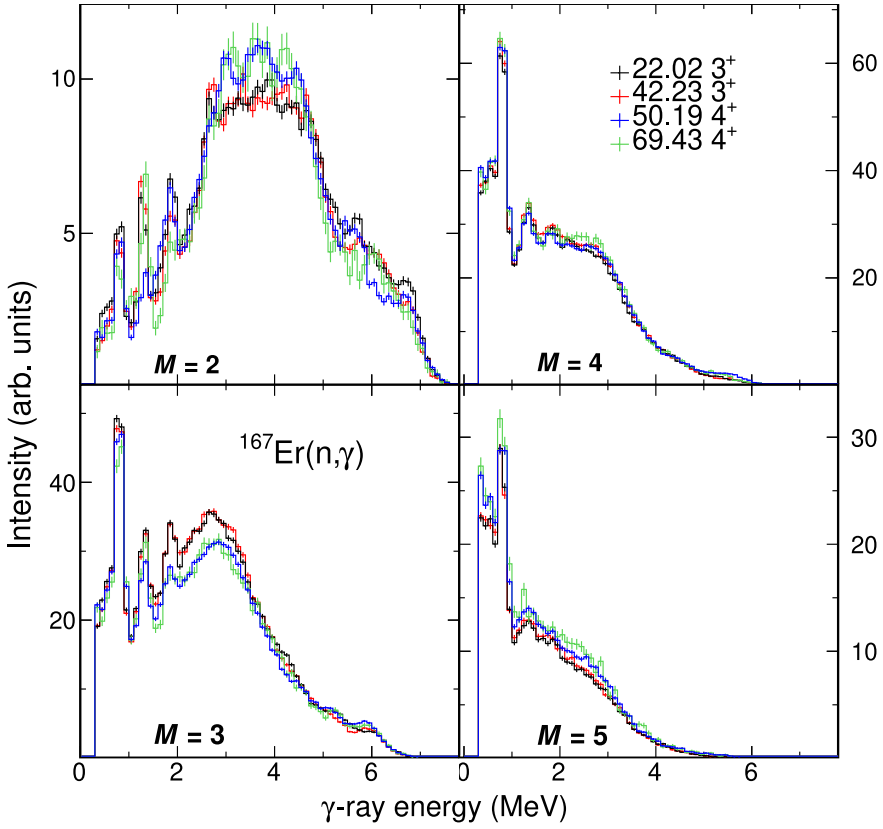

Figure 5.6: Experimental MSC spectra from two resonances of each spin, shown for multiplicities $M = 2 - 5$. The energy and spin of the resonance is indicated in the legend in top-right panel. The spectra are normalized in the same fashion as described in the text.

The presented sum-energy spectra are normalized with a single factor given by the number of events in the Q-value range summed over $M = 2 - 6$. The constructed MSC spectra inherit this normalization. There is a strong background contribution in $M = 1$ spectra, therefore this multiplicity is usually excluded. The contribution from the off-resonance capture on the sample and the capture of scattered neutrons in BaF_2 crystals is subtracted using the experimental MSC spectra from neighboring off-resonance regions on both sides of the resonance. The MSC spectra from 2 resonances of each spin are shown in Fig. 5.6 for $M = 2 - 5$. The allowed J^π of the s–wave neutron resonances in $^{167}\mathrm{Er}(n,\gamma)$ is 3^+ and 4^+, while $J^\pi = 0^+$ for the ground state. Thus we expect a difference between the decay patterns of resonances with different spins, which can be seen in the above-presented comparison of their MSC spectra. The method that was used to assign spins to individual resonances is discussed in Sec. 5.3.

To asses the role of the Porter-Thomas fluctuations in the MSC spectra, we constructed the mean MSC spectra for 12 resonances of $J^\pi = 3^+$ and 15 reso-

nances of $J^\pi = 4^+$ (see Sec. 6.2) in the same fashion as for (n, γ) measurement on Dy isotopes described in [87]. Using the maximum likelihood fit and taking into account experimental uncertainties, we compute the mean experimental intensity and fluctuation of the experimental intensity for each bin.

5.2.2 Experimental Isomeric Ratio

To estimate the experimental isomeric ratio, we define a *prompt* γ *cascade* in a way to include the cascades feeding the isomer and a *delayed* γ *cascade* mostly corresponding to the isomeric decay (see Fig. 5.7) by defining gates on our experimental observables. The prompt cascades were defined as events with $M = 2-6$ and $E_\Sigma = 5 - 8\,\mathrm{MeV}$ and the delayed cascades with $E_\Sigma = 0.4 - 1.0\,\mathrm{MeV}$.

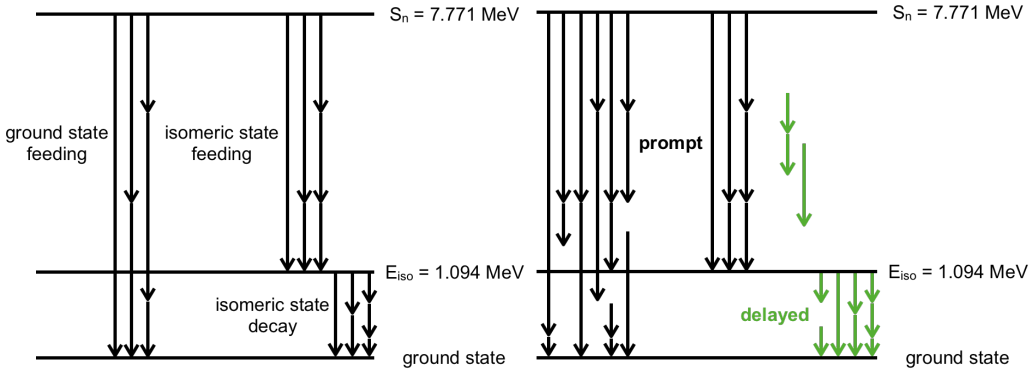

Figure 5.7: Left panel: A simplified scheme of the decay from the neutron capture state, including cascades feeding the isomer and decay of the isomer. Right panel: Examples of the cascades falling into the prompt gate (black), including isomeric feeding, and cascades corresponding to the delayed gate (green), including possible detection of incomplete cascades.

The experimental data provide us with timestamp of each event and we can construct spectra of time differences between the prompt and the delayed cascades. Not all events falling into the prompt or delayed gates come from the feeding/isomeric decay, therefore we also observe accidental coincidences that we do not a-priori know the exact shape of. The TOF spectrum of all events, prompt cascades and delayed cascades for three resonances is shown in Fig. 5.8.

We fit the time-difference spectra with a sum of two exponential functions, one corresponding to the isomeric decay and the second effectively describing the shape of accidental coincidences. An example of the time-difference spectra and the corresponding fit is shown in Fig. 5.9. From the fit, we obtain the isomeric half-life $T_{1/2}$ and the number of isomeric decays N_{iso}. The isomeric ratio is commonly defined as $R_{\mathrm{iso}} = \sigma_{\mathrm{iso}}/\sigma_{\mathrm{tot}}$, where σ_{iso} is the isomer production cross section and σ_{tot} is the total (n, γ) cross section. The experimental isomeric ratio is then calculated as:

$$R_{\mathrm{iso}} = \sigma_{\mathrm{iso}} \times \frac{1}{\sigma_{\mathrm{tot}}} = \frac{N_{\mathrm{iso}}}{\varepsilon_{\mathrm{cs}\to\mathrm{iso}}\ \varepsilon_{\mathrm{iso}}} \times \frac{\varepsilon_{\mathrm{pr}}}{N_{\mathrm{pr}}}, \tag{5.1}$$

where N_{pr} is the number of detected prompt cascades obtained from simple experimental counting. $\varepsilon_{\mathrm{pr}}$, $\varepsilon_{\mathrm{cs}\to\mathrm{iso}}$ and $\varepsilon_{\mathrm{iso}}$ are the detection efficiencies for measuring

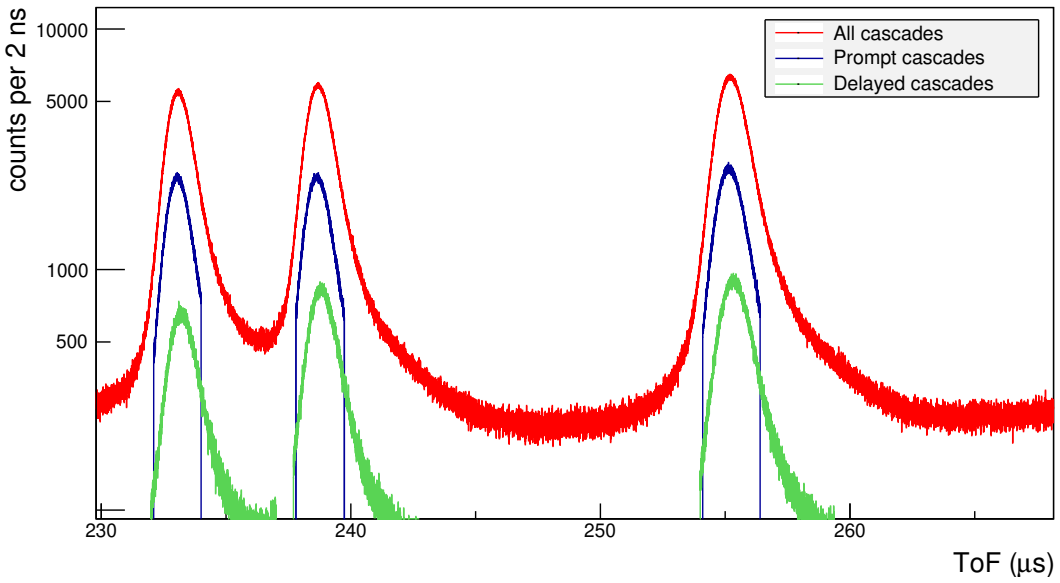

Figure 5.8: TOF spectrum of three resonances for all events (red), events falling into the prompt gate (blue) and delayed gate (green). The center of the delayed-cascades peak is shifted towards higher TOFs with respect to the prompt one.

the prompt cascade, the cascade feeding the isomer and the isomeric decay, respectively. Efficiencies were obtained from the simulations, see Sec. 6.2. It should be noted that the isomeric decay scheme is known, a simplified level scheme with the most intense transitions is shown in Fig. 5.10. Comparison of the determined experimental and simulated R_{iso} is shown in Sec. 6.3.

5.2.3 Parasitic Detector Effects

The data acquistion system integrating the fast and slow components of the most recent trigger cannot trigger again within a 1000 ns time window. If a γ ray from a cascade B hits the crystal integrating the waveform of a previous cascade A, this leads to a crystal pile-up, where the total integral obtained from the crystal is larger and results in larger E_{Σ}^{A} of the first event. On the other hand, the E_{Σ}^{B} is reduced by the missing γ-ray energy and its crystal multiplicity M_{cr}^{B} is reduced down by one. This effect is referred to as "dead time" and to account for it in the analysis, the relative number of crystals that are busy integrating at the same time as a function of TOF (and analogously E_n) is recorded. Hereafter, we will refer to this observable as the "detector load" $D(E_n)$, the average detector load over all runs is shown in Fig. 5.11. In the offline analysis, we studied the influence of the large detector load on the experimental spectra (see Sec. 5.3.3). Naturally, the largest observed detector loads correspond to the strongest resonances in $^{167}\mathrm{Er}(n,\gamma)$.

To avoid the dead-time effects, in the spin-assignment analysis (see Sec 5.3) we did not consider the centers of the strongest resonances with the average $D(E_n) \gtrsim 5\%$ from the first $^{167}\mathrm{Er}(n,\gamma)$ measurement and if necessary, we used only events from the edges of these resonances where $D(E_n)$ is low enough. In the additional measurement with 1/4 of the sample mass, the average $D(E_n)$ was much

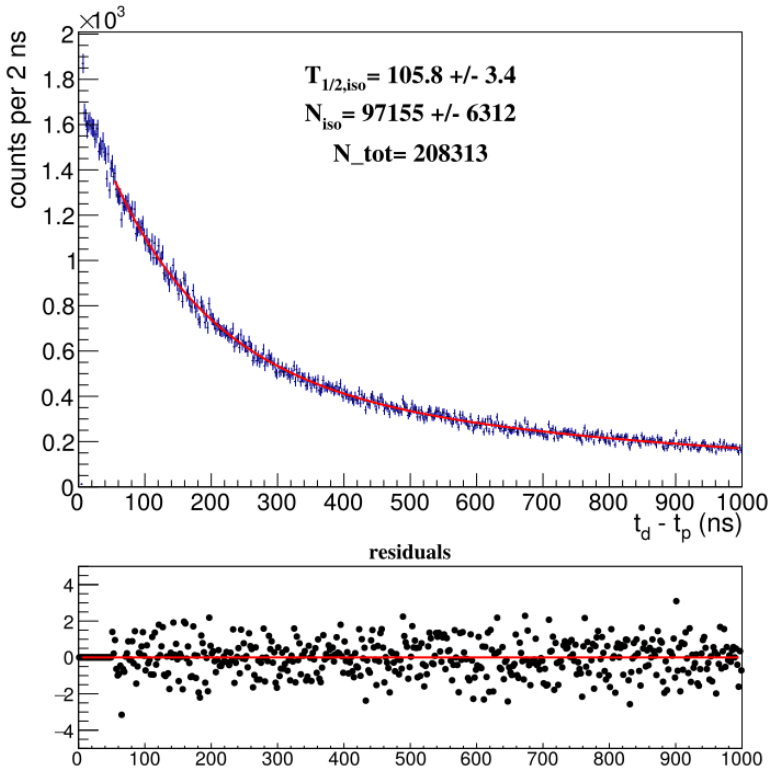

Figure 5.9: Spectrum of time difference between the prompt and delayed cascades for 50.19 eV resonance. The spectrum is fitted by a sum of two exponential functions, the obtained half-lives and N_{iso} are listed in the legend. The bottom panel shows the residuals.

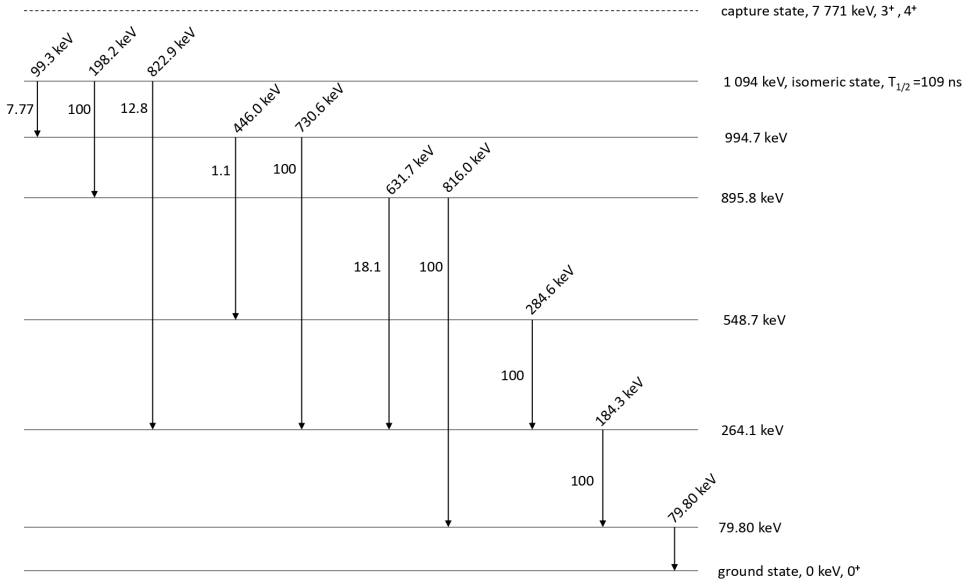

Figure 5.10: Partial low-level scheme of ^{168}Er including the isomeric state at 1094 keV excitation energy and its decay scheme. Excitation energies of the levels, photon energies and intensities are taken from from [104].

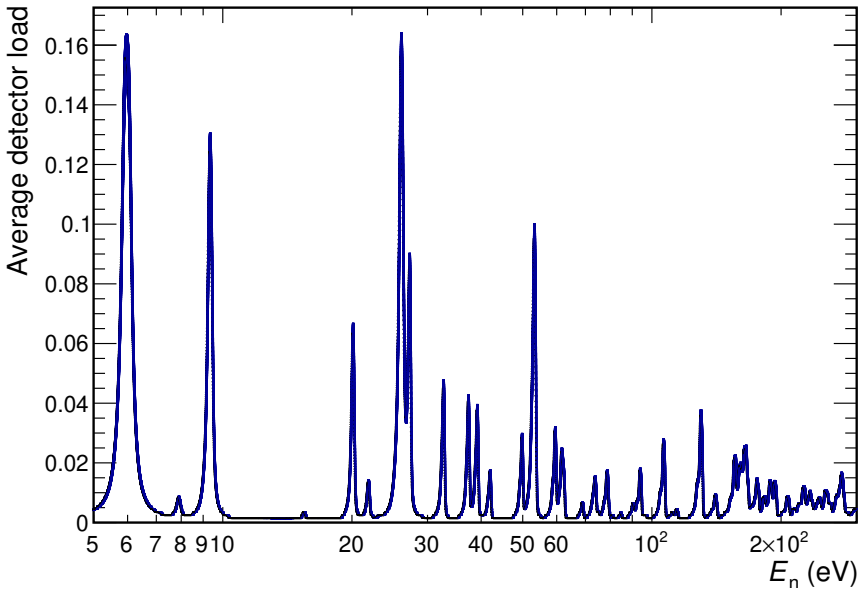

Figure 5.11: Average detector load from the higher-mass measurement, shown as a function of neutron energy.

lower and no significant dead-time effects were observed. However, the latter measurement suffered from lower statistics, therefore the presented sum-energy and MSC spectra are constructed from the data measured with the thicker target, using only resonances with maximum $D(E_n) \lesssim 5\%$.

Another detector effect related to high count rate is the event pile–up, where two (or more) separate γ cascades are recorded within the preset coincidence window and form a single event. This effect results in increased E_Σ and M, its contribution (together with neutron capture in BaF_2 crystals) can be seen in Fig. 5.4 as events with $E_\Sigma \gtrsim 8\,\mathrm{MeV}$. Only resonances with low event pile-up were considered in the analysis, which usually corresponds to our requirement of low $D(E_n)$.

5.3 Spin Assignment of Neutron Resonances

The difference in the measured γ-ray spectra of neutron resonances with different spin (see Fig. 5.6) can be exploited to determine the spin of these resonances. Knowledge of the spin is essential when constructing the mean sum-energy and mean MSC spectra. Moreover, resonance sequences of a single spin and mixed spin are an important input for tests of GOE predictions related to fluctuation properties of neutron resonances (see Chap. 4). This section is dedicated to the short introduction of the method used to assign spins to resonances in $^{167}\mathrm{Er}(n,\gamma)$ and we show the related experimental spectra.

5.3.1 Optimized γ-multiplicity-based Spin Assignment Method

The fundamental of the method is based on different multiplicity distribution of γ rays coming from the decay of resonances with different spin. Several methods

for resonance spin assignment based on this principle have been proposed [129, 130]. Here we present a short overview of the method we adopted, detailed characterization can be found in [131]. The main advantage of this method is its ability to resolve close dublets of different spins at low neutron energies, which may remain undetected by other methods of spin assignment.

The experimental yield for γ multiplicity M at neutron energy E_n is expressed as a sum of contributions of each prototype:

$$y_M(E_n) = \sum_{i=1}^{N} q^i(E_n)\mu_M^i + \delta y_M(E_n) \tag{5.2}$$

where μ_M^i are *prototypical multiplicity distributions*, $\delta y_M(E_n)$ are random perturbations due to counting statistic uncertainties and N is the number of prototypes. The multiplicity normalization condition holds $\sum_{M=M_{min}}^{M_{max}} \mu_M^i = 1$.

The total capture yield at energy E_n then can be expressed as a sum of all partial contributions from the decomposed yields $q^i(E_n)$ for a given prototype i at neutron energy E_n:

$$q(E_n) = \sum_{i=1}^{N} q^i(E_n) \tag{5.3}$$

The objective of the method is to obtain the best estimates of the decomposed yields $q^i(E_n)$, which according to the method of least squares minimize the sum of the weighted quadratic deviations:

$$S^2 = \sum_M \frac{1}{\sigma_M^2}\left(y_M - \sum_{i=1}^{N} \mu_M^i q^i\right)^2 \tag{5.4}$$

where $\sigma_M^2(E_n) = \mathrm{Var}[y_M(E_n)]$ is the variance.

In practice, an effective way to apply this method is for $N = 2-3$, where two prototypical multiplicity distributions are taken from resonances of different spins and the optional third prototype represents the background contribution. The background prototype can be taken from the off-resonance region or from measurements with a ^{208}Pb sample that provide multiplicity distribution for events related to neutron scattering. The majority of the background events fall into $M = 1$ and significantly decrease with higher M.

5.3.2 Spectra of Decomposed Yields

To construct the spectra of decomposed yields, only events with $E_\Sigma = 7 - 8\,\mathrm{MeV}$ were chosen. The multiplicity distribution of the two spin prototypes (taken from isolated resonances of the corresponding spins) and one background prototype (taken from the off-resonance region) can be found in Fig 5.12. These distributions are normalized to their intergral for $M = 2 - 6$, as we expect the background contribution in $M = 1$.

The illustration of the experimental yield and decomposed yields for a chosen energy range can be found in Fig. 5.13. We can clearly identify two well-resolved resonances of $J^\pi = 3^+$ and two of $J^\pi = 4^+$, as the decomposed yields of the corresponding spin prototype nicely follow the shape of the experimental yield. There is a clear evidence of a dublet structure in the decomposed yields at $\approx 53\,\mathrm{eV}$,

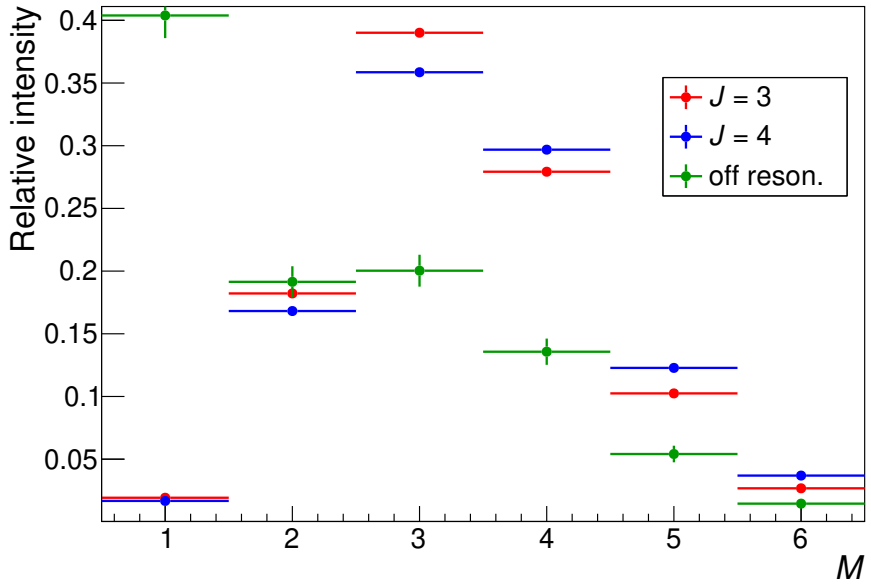

Figure 5.12: Multiplicity distribution of two spin prototypes and one off-resonance prototype. The distribution is normalized to the number of events with $M-2-6$.

while a singlet is reported in available data [128]. In fact, we can see an indication of a more complex structure than singlet already from comparing the shape of the experimental yields of 53 V resonance and the neighboring resonances. The decomposed shapes agree with the shapes of the neighboring resonances. Another example of the decomposed spectra, in particular using three prototypes, is shown in Fig. 5.14.

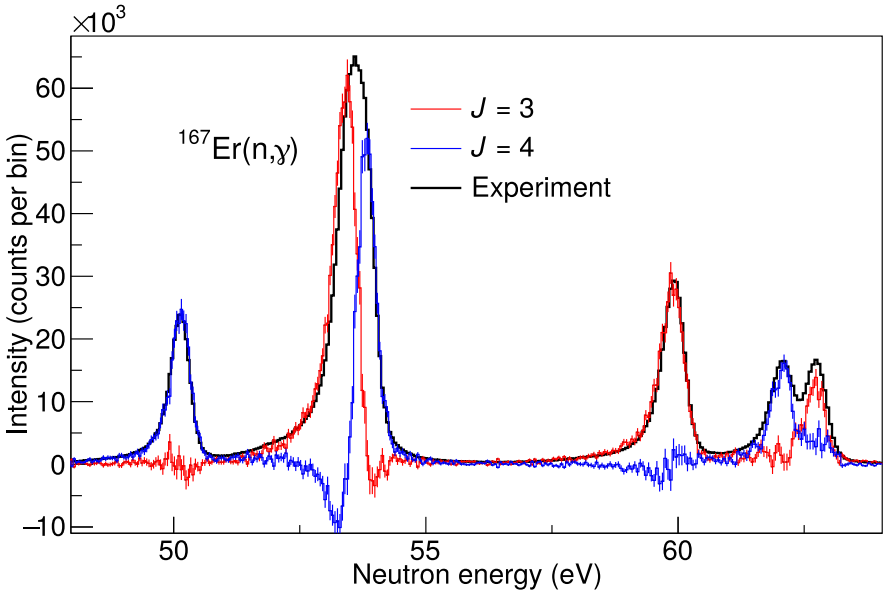

Figure 5.13: Experimental and decomposed TOF spectra. The decomposition was performed using $M = 2-6$ with two prototypes. There is a clear evidence of a previously unreported doublet near 53.5 eV.

In reality, intensities of the primary transitions fluctuate even among the reso-

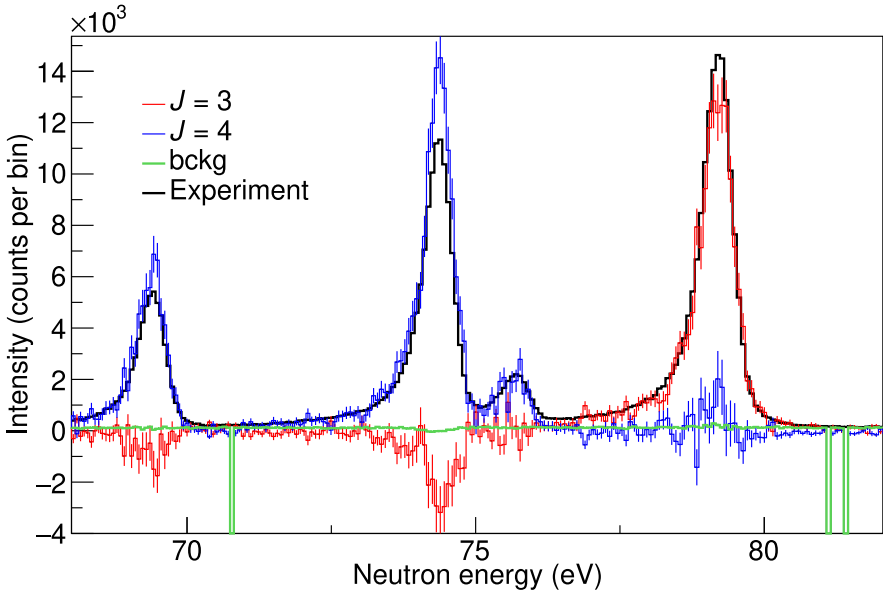

Figure 5.14: Experimental and decomposed TOF spectra. The decomposition was performed using $M = 1-6$ with three prototypes (two spins and one background prototype).

nances of the same spin following the PT distribution. Due to these fluctuations, the multiplicity distributions of the resonances with the same spin are not identical, which results in a small deviation of the decomposed yield of the correct spin. For the method to work, it is thus essential to have smaller differences between resonances with the same spin than between resonances with different spin. More details about the observed and expected fluctuations of the decomposed yields can be found in App. A.

5.3.3 Influence of the Detector Effects

As discussed in Sec. 5.2.3, parasitic detector effects lead to changes in the measured multiplicity distribution. Consequently, this effect can be observed in the spectra of decomposed yields. The example of a very strong resonance at 9.39 eV is shown in Fig. 5.15, where the sum-energy spectra of different resonance parts are plotted. Influence of the dead time causes enhancement of the sum-energy spectra at lower energy below the full-energy peak, as a part of the energy is not detected within the given event. As a result, the multiplicity distribution is shifted towards lower multiplicities for events from resonances with a large detector load $D(E_n)$. In the figure, we can see that the effect is most prominent in the center of the resonance, where the maximum $D(E_n)$ reaches $\approx 13\%$. For comparison, analogous figure is shown for the 22.02 eV resonance with much lower $D(E_n) \approx 1.5\,\%$, where we do not observe any discrepancies between the sum-energy spectra of different resonance parts.

These detector effects influence the decomposed yields, see the left panel of Fig. 5.16, where the two of the strongest resonances are displayed. Very large deviations are observed mainly in the center of resonances. The resonance edges with low $D(E_n)$ are described well by the expected decomposed yield and can be used to assign spins even for these specific cases. We compared the multiplicity

ditribution of the center of 9 eV resonance (constructed from $E_\Sigma = 7 - 8$ MeV events) with three other weaker resonances of the same spin and as expected, in the 9 eV case the multiplicity distribution is shifted towards lower values - see Fig. 5.17.

To check the correctness of our assignment, the same analysis was performed for the newer $^{167}\mathrm{Er}(n,\gamma)$ measurement with the smaller-mass sample, resulting in lower $D(E_n)$. As evident from the right panel in Fig. 5.16, no major deviations between the expected decomposed yield and experimental one were observed.

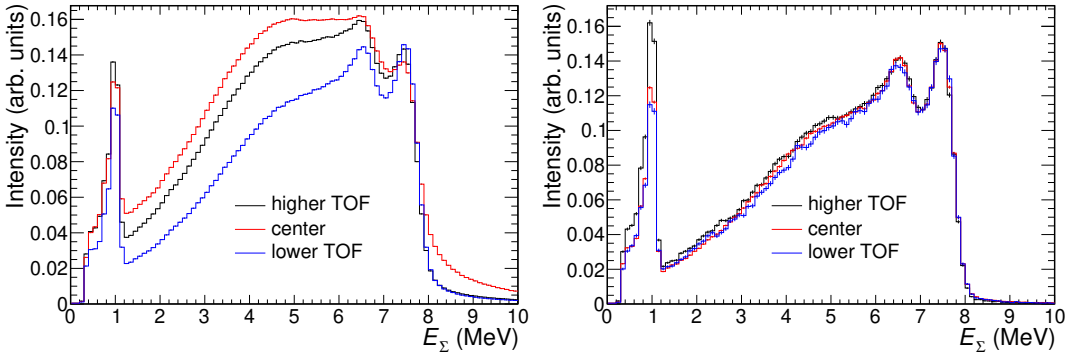

Figure 5.15: Sum-energy spectra summed over $M = 2 - 5$ from 9 eV resonance (left panel) and 22 eV resonance (right panel). The shown spectra were constructed for different parts of the corresponding resonance to demonstrate the effect of high detector load on the central part of the resonance and higher TOF (correspondingly lower E_n).

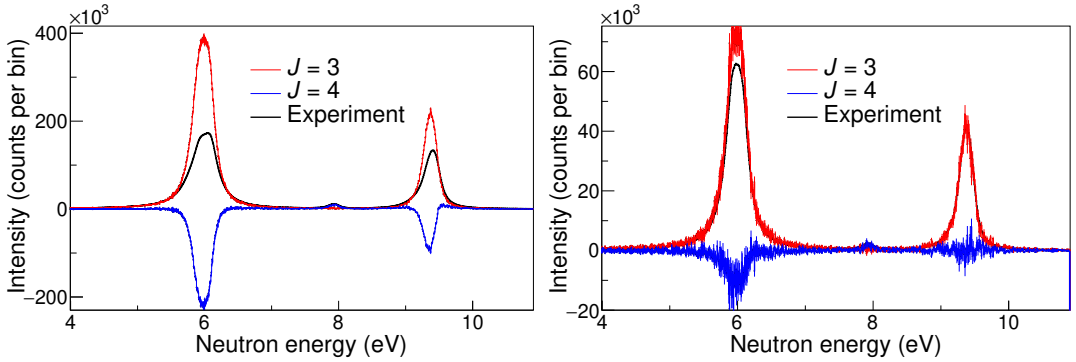

Figure 5.16: Experimental and decomposed TOF spectra. The decomposition was performed using $M = 2 - 6$ with two prototypes. Left panel: Measurement with a thick target, a significant deviation of $J = 3$ expected decomposed yield from the experimental one is observed for both resonances. Right panel: Newer measurement with 1/4 of the former target mass, detector effects related to the dead time are supressed.

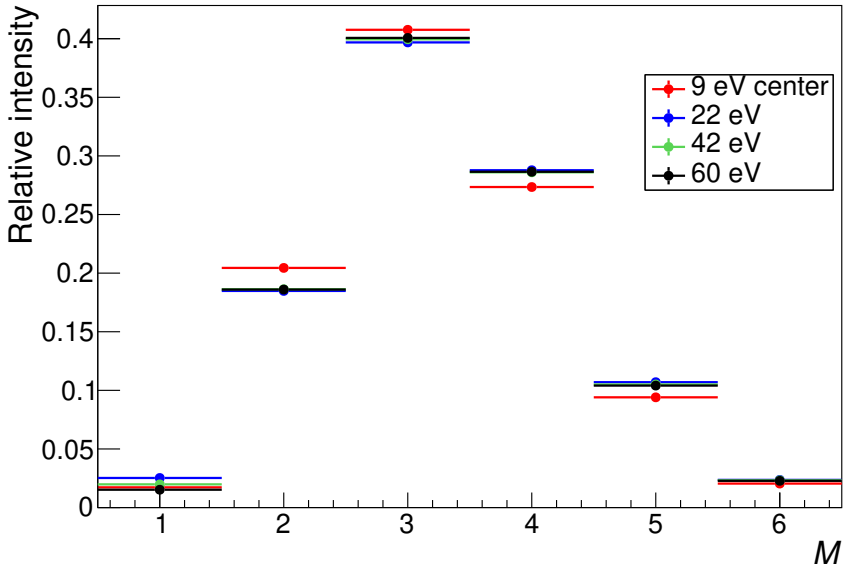

Figure 5.17: The multiplicity distribution of four $J = 3$ resonances constructed from events with $E_\Sigma = 7 - 8\,\mathrm{MeV}$. The distribution is normalized to the number of events with $M - 2 - 6$. In the 9 eV case the central part of the resonance has a large $D(E_n)$ and we observe a shift towards lower multiplicities in comparison with other three resonances with much lower $D(E_n)$.

6. Results and Discussion

The first part of this chapter, Sec. 6.1, is dedicated to the analysis of fluctuation properties of neutron resonances and determining the average resonance spacing. The second part, Sec. 6.2, summarizes the results on the LD and PSFs obtained from the MSC spectra and their comparison with other available data. Finally, the last Sec. 6.3 presents the deduced experimental and simulated isomeric ratio in ^{168}Er.

6.1 Statistical Properties of Neutron Resonances

Analysis of neutron resonances in $^{167}\mathrm{Er}(n,\gamma)$, in particular their spin assignment discussed in Sec. 5.3, provides us with pure- and mixed-spin resonance sequences that can be utilized to test RMT predictions of the GOE. The GOE version of the RMT is generally used to examine completeness of measured resonance sequences and often also to estimate the number of missing resonances. There are two ways how an *s*-wave resonance can be missed in the experiment - (a) it is a part of a close dublet or (b) it is too weak and below the threshold of observability (a sub-threshold resonance). The first option for $^{167}\mathrm{Er}(n,\gamma)$ was checked using the method of spin assigment described in Sec. 5.3 and several new dublets were found. The list of all resonances with assigned spins and their comparison to those reported in Atlas [128] is included in App. A.

The second option was addressed by estimating the number of sub-threshold resonances using the fluctuation properties of reduced neutron widths Γ_n^0 as well as GOE predictions of statistical properties of resonance positions. In the following two subsections, we discuss the expected number of missing resonances from both Γ_n^0 fluctuations and resonance-position fluctuations for each of the experimental sequences. Three different lengths of the experimental sequences were tested - $E_{\mathrm{max}} = 135$, 200, and 285 eV. The lowest E_{max} was chosen to have a sufficiently high probability for the sequence to be complete, while the other two E_{max} values were determined by the uncertain spin assigned just above the given energy. The spin of the 204 eV resonance was not assigned in our analysis nor in Atlas [128], therefore three possible options (including no resonance at this energy) were tested for the longest sequence.

Here we summarize the most important results for $^{167}\mathrm{Er}(n,\gamma)$, for details - such as the sensitivity of the tested statistics to different number of missing resonances - see App. A. Furthermore, we show additional plots that were not included in App. A.

6.1.1 Fluctuations of Neutron Widths

We generated 10^4 resonance sequences in the same fashion as introduced in Sec. 4.3.1 and we estimated the number of sub-threshold resonances using two different thresholds. The tested threshold shapes were $T_1 = C_1 E^{3/2}$ and $T_2 = C_2 E$, where $C_1 = 0.6 \times 10^{-8}\,\mathrm{eV}^{-1/2}$ and $C_2 = 1.1 \times 10^{-7}$. The parameters for gen-

erating neutron widths were $S_0 = 2.0 \times 10^{-4}$ [128] and $D_0 = 3.85\,\mathrm{eV}$, which is close to the estimated spacing discussed below. The simulated $2g\Gamma_n/\sqrt{E/1\mathrm{eV}}$ values for one chosen sequence are compared with the experimental ones reported in Atlas [128] in Fig. 6.1. The expected strength $S_1 = 1.5 \times 10^{-4}$ [128] of p-wave resonances effectively prevents us from observing any p-wave resonances in the E range of our interest.

The fractions of complete simulated mixed-spin sequences F_0^m (i.e. no resonance in the sequence is below the threshold) are listed in Tab. 6.1 for all three E_{max}. The dependence on S_0 and D_0 was found relatively weak for the fixed E_{max}. The results indicate that completeness of the sequences cannot be guaranteed even for the shortest tested sequence. The distribution of the simulated number of the sub-threshold resonances for different E_{max} are shown in Fig. 6.1 for T_1 threshold. Applying the T_2 threshold results in slightly more missing resonances below $\approx 300\,\mathrm{eV}$ (see Tab. 6.1), which compared to the right panel of Fig. 6.1 leads to shifted distribution of sub-threshold resonances for T_2 towards higher values.

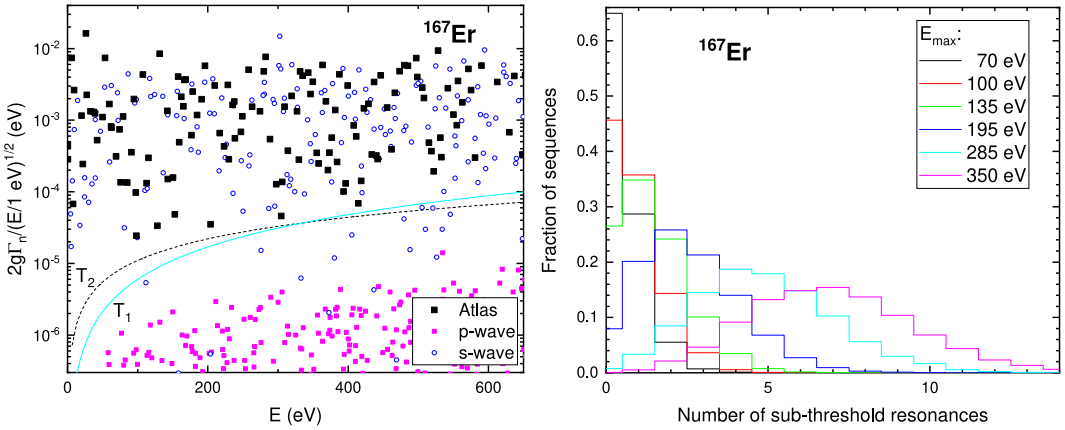

Figure 6.1: Left panel: Simulated $2g\Gamma_n/\sqrt{E/1\mathrm{eV}}$ as a function of E for s-wave and p-wave resonances compared to experimental resonances of ^{167}Er taken from Atlas [128]. Assumed thresholds T_1 and T_2 for resonance observability are shown as solid lines. Right panel: Simulated distribution of number of sub-threshold resonances for T_1 threshold and different E ranges.

Threshold	$F_0^m \times 10^3$ / Mode		
E_{max} (eV)	135	200	285
T_1	280/1	84/2	12/4
T_2	152/1	37/3	4/5

Table 6.1: Fraction of complete mixed-spin sequences F_0^m of ^{167}Er and the mode of distribution of sub-threshold resonances for different E_{max} and both adopted thresholds. Parameters used in simulations were $S_0 = 2.0 \times 10^{-4}$ and $D_0 = 3.85\,\mathrm{eV}$.

6.1.2 Fluctuations of Resonance Positions

We used three different statistics based on resonance positions (as discussed in Sec. 4.2.2) to test the completeness of experimental resonance sequences and to estimate the number of missing ones. We generated and diagonalized 5000 GOE matrices in the same process as described in Sec. 4.3.2. The distributions of the desired quantities were deduced from complete sequences of the same length $L_{\max}$ as experimental ones. In addition, we simulated longer sequences of length $L_{\max} + L_{\text{extra}}$, where we then randomly removed L_{extra} resonances to mimic the experimental case of missing resonances. The incomplete sequences were checked for all $L_{\text{extra}} \lesssim L_{\max}/3$. We analyzed pure-spin as well as mixed-spin sequences, several spin-mixing ratios were tested. The results of the statistical analysis are presented in Tab. 6.2 for all three tested lengths $E_{\max}$.

$E_{\max}$(eV)	$L^-_{\max}$	$L^+_{\max}$	$J^\pi = 3^+$			$J^\pi = 4^+$			mixed		
			Δ_3	D_i	ρ	Δ_3	D_i	ρ	Δ_3	D_i	ρ
135	18	17	0–4	0+	0	0+	0+	0+	0+	0+	0+
200	23	27	0+	0+	×	1+	0+	0+	0+	0+	0+
285[§]	29	39	1+	0+	0+	2+	0+	0+	1+	0+	0+
285[‖]	30	39	0+	0+	0+	2+	0+	0+	0+	0+	0+
285[¶]	29	40	1+	0+	0+	2+	0+	0+	0+	0+	0+

[§] no 204 eV
[‖] 204 eV 3^+
[¶] 204 eV 4^+

Table 6.2: Results of the statistical analysis of ^{167}Er resonance sequences. The range of L_{extra} for which the sequence is compatible with GOE predictions is indicated, e.g. "0+" means $L_{\text{extra}} \geq 0$, "1+" means $L_{\text{extra}} \geq 1$ etc. The symbol $\times$ indicates inconsistence with all L_{extra} values for the adopted criterion (see text). Results for three different statistics are presented - Δ_3, NNSD (column labeled D_i) and correlation coefficient ρ .The number of resonances of spin $J = 3$ and $J = 4$ are denoted as $L^-_{\max}$ and $L^+_{\max}$, respectively. The different sequence versions are explained by the respective footnotes.

The most simple measure is the NNSD, which was derived from the generated GOE sequences. The agreement with the experiment was checked using the statistic proposed by Zhang in Ref. [132]. The value of the statistic was calculated for the experimental sequence and compared to the distribution of statistics from individual simulated sequences - the p-value was determined. If this p-value fell into the 95.45% central interval corresponding to $\pm 2\sigma$ of the normal distribution, the experimental NNSD was considered consistent with the predictions of GOE. The same process was applied to generated sequences with L_{extra} resonances removed and the same length $L_{\max}$ as experimental sequence after the removal. An example of a cumulative distribution function (CDF) of nearest neighbor spacings for simulated GOE sequences and experimental sequence is shown in Fig. 6.2. The restrictive power of NNSD statistic is very low, we obtained compatibility of experimental sequences with GOE for all the tested L_{extra}.

The second tested statistic was the correlation coefficient $\rho(D_i, D_{i+1})$ calculated from the adjacent spacings both from GOE generated sequences and ex-

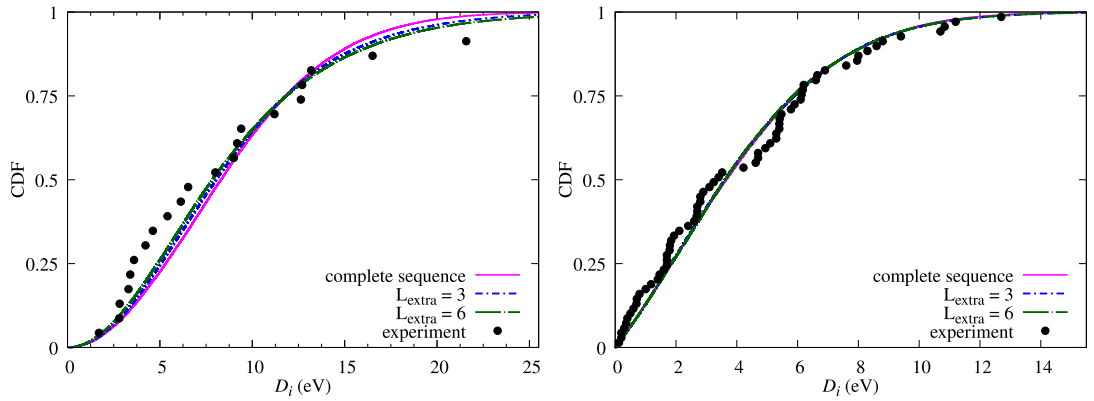

Figure 6.2: Left panel: CDF of the simulated NNSD for a complete pure-spin $L_{\max} = 23$ sequence together with the NNSD for sequences where $L_{\text{extra}} = 3$ and 6 resonances are missed. The experimental D_i of $J^\pi = 3^+$ sequence for $L_{\max} = 23$ and $E_{\max} = 200\,\text{eV}$ are shown as black points. Right panel: Analogous figure for simulated and experimental NNSD of $L_{\max} = 69$ and $E_{\max} = 285\,\text{eV}$ mixed-spin sequence.

perimental resonance sequences. The CDF of the generated $\rho(D_i, D_{i+1})$ values for a complete sequence with $L_{\max} = 23$ as well as $L_{\text{extra}} = 1$, 3, 6, compared to the experimental value can be found in Fig. 6.3. The compatibility was again determined using the 95.45% central interval. Similarly as for the NNSD, the sensitivity of $\rho(D_i, D_{i+1})$ is very limited - except for $J = 3$ sequences of $E_{\max} = 135$ and 200 eV, there are no restrictions on the number of missing resonances for relevant L_{extra} (see Tab. 6.2). As can be seen in Fig. 6.3, if the ρ^{exp} value is very small, we reject compatibility for all $L_{\text{extra}} \geq 0$ using our criterion, which is labeled with a symbol $\times$ in Tab. 6.2. However, generally, the observed shift and widening of the distribution with increasing L_{extra} is not large enough to provide sufficient restrictive power.

To assess the role of the long-range correlations, we used the Δ_3 statistics defined by Eq. (4.14). Completeness of the experimental sequences was traditionally examined by the compatibility of $\Delta_3^{\text{exp}}(L_{\max})$ with the distribution of generated or analytically derived $\Delta_3(L_{\max})$. We chose a different criterion to account for behavior for all L, where we count the number of Δ_3^{exp} points - for a given experimental sequence - outside the 95.45% central interval determined from the simulated Δ_3. It is important to note that this corridor is asymmetric. Then we calculate the probability that a simulated sequence has this number or more Δ_3 points outside the same corridors. If the probability is lower than 4.55%, we reject the hypothesis that the given experimental sequence is compatible with the simulated one. An illustration of the criterion of a complete sequence is shown in Fig. 6.4. The probabilities are calculated for complete simulated sequences as well as those where resonances were removed (i.e. $L_{\text{extra}} > 0$). The experimental and simulated $\Delta_3(L)$ together with the 95.45% corridors for different L_{extra} is shown in Figs. 6.5 and 6.6.

The Δ_3 statistic seems to be the most restrictive from the tested ones. However, its sensitivity is still limited - the corridors are wide and overlapping and compatibility with a large number of different L_{extra} is obtained especially if the

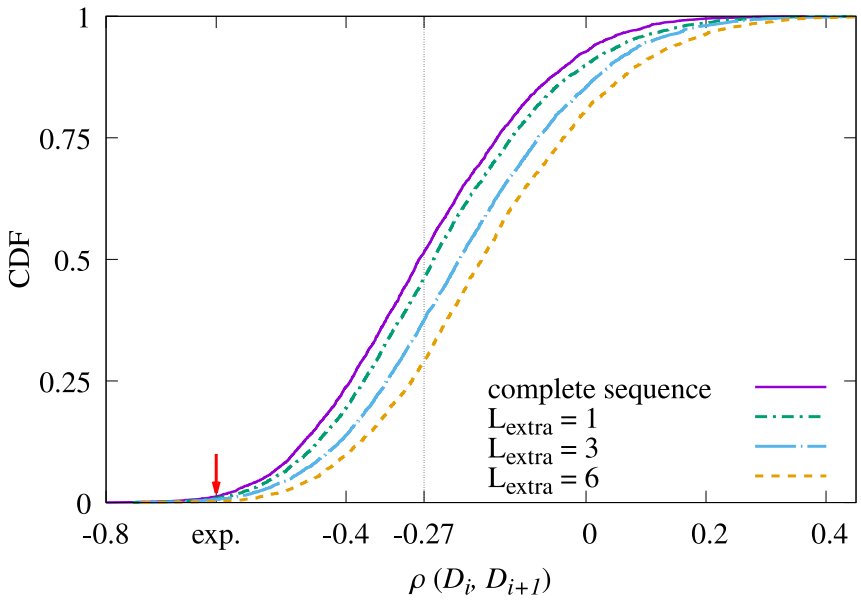

Figure 6.3: CDF of the simulated correlation coefficient $\rho(D_i, D_{i+1})$ for a complete pure-spin $L_{\max} = 23$ sequence together with sequences where $L_{\text{extra}} = 1$, 3, and 6 resonances were missed. $\rho^{\text{exp}} = -0.6164$ for the $L_{\max} = 23$ sequence ($E_{\max} = 200\,\text{eV}$) of $J = 3$ resonances in ^{167}Er is shown as a red arrow. The corresponding CDF value is 0.0127 for the complete sequence and lower for any sequence with $L_{\text{extra}} \geq 1$. The GOE predicted mean value of -0.27 [117] for a complete sequence is displayed as a dashed line.

$\Delta_3^{\text{exp}}(L)$ points lie above the simulated GOE median for the complete sequence (as illustrated in Fig. 6.5). Therefore in the majority of cases, we obtained compatibility even with the largest tested L_{extra}. On the other hand, if the $\Delta_3^{\text{exp}}(L)$ values are lower than simulated ones as illustrated in Fig. 6.6, we are able to obtain the maximum compatible L_{extra} from GOE, which is 4 missing resonances in this case. Furthermore, it is clear from the Tab. 6.2 that the sensitivity of Δ_3 is lower for the mixed-spin sequences than the pure-spin ones. Nonetheless, the allowed numbers of missing resonance from the Δ_3 statistic in Tab. 6.2 are consistent with the estimated mode of the unobserved sub-threshold resonances in Tab. 6.1.

6.1.3 Average Resonance Spacing

If a resonance sequence is complete and the positions follow predictions of the GOE, the average spacing can be determined very precisely [118, 117], even if the sequence is not very long and consist of a few tens of resonances. In reality, if we cannot guarantee completeness, the uncertainties are larger due to corrections to the unobserved resonances. To determine the D_0, we adopted the following approach. We assumed the probability distribution of the sub-threshold resonances as presented in Sec. 6.1.1. For each number of sub-threshold resonances we then determined D_0 from the difference between the position of the last and the first resonance as given in Eq. (4.8). In reality, we assumed that the actual position of the last resonance fluctuates according to the GOE predictions [118].

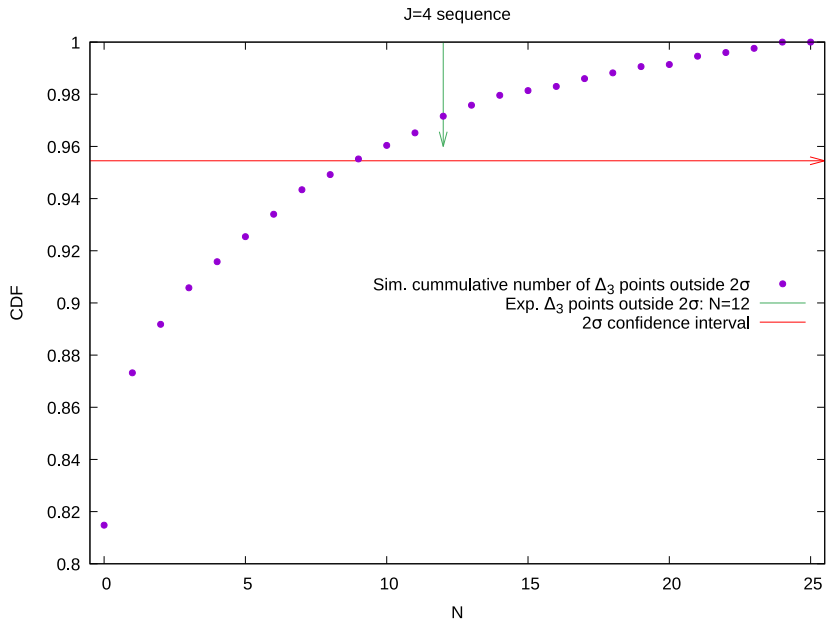

Figure 6.4: CDF for the pure-spin complete simulated sequences of $L_{\max} = 27$ to have N of $\Delta_3(L)$ points outside the simulated 95.45% central interval (i.e. $\approx 81\%$ of the 5000 simulated sequences have 0 points outside the 95.45% central interval). The experimental $J = 3$ sequence of $L_{\max} = 27$ and $E_{\max} = 200\,\text{eV}$ has $N = 12$ points outside the simulated 95.45% central interval (marked with a green arrow). The 4.55% limit for rejection of the hypothesis is shown as a red arrow.

We also took into account restrictions on number of missing resonances resulting from the Δ_3 statistic (see Tab. 6.2).

The determined average spacings for each $E_{\max}$ and T_1 threshold are listed in Tab. 6.3. The results for T_2 threshold differ at maximum by around a third of the given uncertainty. The obtained $D_0 = 3.86(12)\,\text{eV}$ for the maximum sequence length is compatible with $D_0 = 4.06(17)\,\text{eV}$ reported by Liou *et al.* [117], $D_0 = 3.80(21)\,\text{eV}$ from Atlas [128] and $D_0 = 4.20(30)\,\text{eV}$ from the RIPL-3 database [21]. The discussion about the mixing ratio D_0^-/D_0^+ of the average spacings for resonances of $J = 3$ and $J = 4$, respectively, can be found in App. A.

$E_{\max}$(eV)	D_0^-(eV)	D_0^+(eV)	D_0(eV)
135	7.46(51)	7.87(58)	3.72(19)
200	8.49(50)	6.87(34)	3.79(15)
285¶	9.03(48)	6.70(25)	3.86(12)

¶ 204 eV 4^+

Table 6.3: Determined average resonance spacing D_0^- and D_0^+ for pure sequences of $J = 3$ and $J = 4$ spin, respectively and D_0 for mixed-spin sequences.

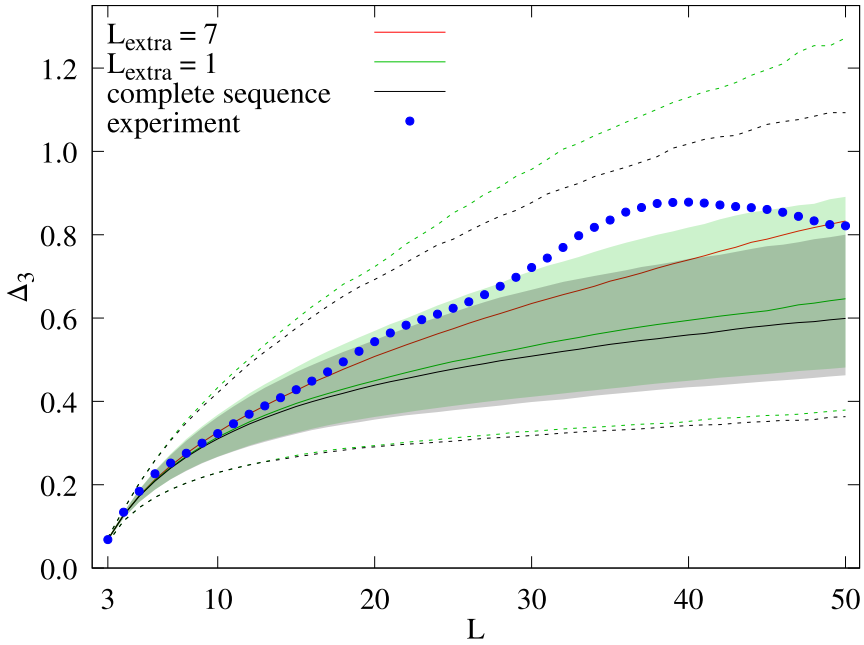

Figure 6.5: Simulated Δ_3 statistics as a function of L for mixed-spin sequences with $L_{\max} = 50$ and $L_{\text{extra}} = 0, 1$ and 7. The shaded corridors correspond to 68.27% central interval and the dashed lines for the complete sequence (black) and $L_{\text{extra}} = 1$ (green) show the edges of 95.45% central interval. The experimental values for the mixed-spin sequence of $L_{\max} = 50$ and $E_{\max} = 200\,\text{eV}$ are shown as blue points.

6.2 Level Density and Photon Strength Functions

We can learn about the LD and PSFs governing the γ-decay by adopting a trial-and-error approach of comparing experimental quantities such as the sum-energy and MSC spectra to their counterparts simulated by the DICEBOX code. We tested several hundred model combinations of LD and PSFs to check the agreement with the experimental spectra and draw conclusions about models compatible with our data or those we can reject. It has been checked that the influence of the $E2$ PSF on the shape of simulated MSC spectra is negligible, therefore we dedicate the following discussion only to LD, $E1$, and $M1$ PSF. A single-particle model of $E2$ PSF, $f^{(E2)} = 1 \times 10^{-11}\,\text{MeV}^{-5}$ was adopted.

It is very difficult to quantify the level of agreement between the simulated and experimental MSC spectra, as the individual bins are mutually correlated and the correlation matrix is a-priori not known, therefore an extensive number of additional time-consuming simulations would be needed. For this reason, the agreement was checked only visually.

If not stated otherwise, we simulated 20 NSs with one NR within each of them (for more details about the algorithm see Chap. 3). It has been verified that this approach is justified for a simple search of appropriate PSF and LD models [87]. Each NS included 2×10^5 γ cascades that were subsequently fed to the GEANT4 simulation of the detector response. For simplicity, we plot the resulting simu-

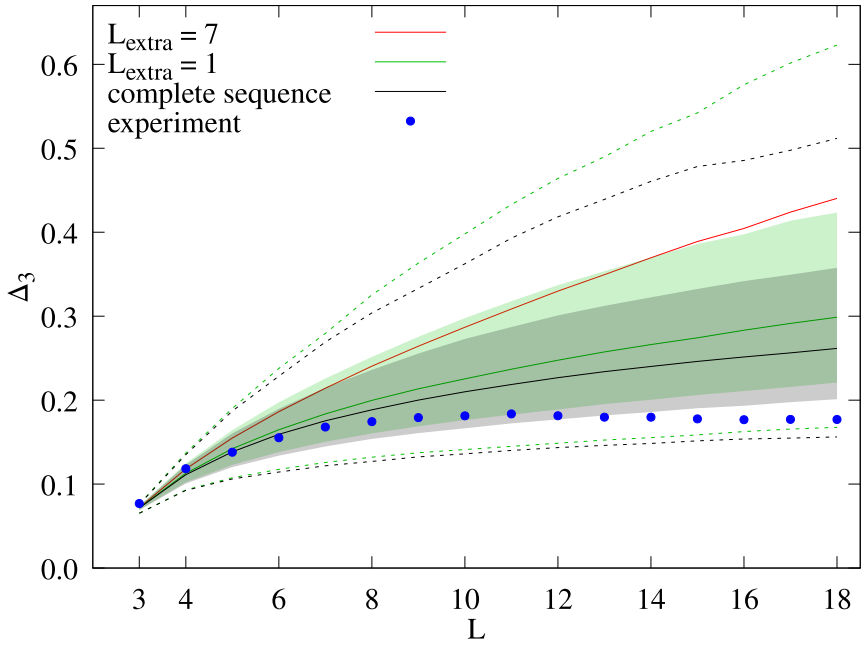

Figure 6.6: Simulated Δ_3 statistics as a function of L for pure-spin sequences with $L_{\max} = 18$ and $L_{\text{extra}} = 0, 1$ and 7. The shaded corridors correspond to 68.27% central interval and the dashed lines for the complete sequence (black) and $L_{\text{extra}} = 1$ (green) show the edges of 95.45% central interval. The experimental values for the $J = 3$ sequence of $L_{\max} = 18$ and $E_{\max} = 135\,\text{eV}$ are shown as blue points.

lated spectra as the average value ± standard deviation over the suprarealizations as a grey (or blue) band in the figures. With one exception, the presented MSC spectra are plotted simultaneously for both spins and $M = 2 - 4$, as there are no visible structures in $M \geq 5$ for $E_\gamma \gtrsim 1\,\text{MeV}$. To compare the experimental fluctuations of the MSC intensities with the predicted fluctuations from the simulations, we generated an extended simulation with 50 NRs in each of 50 NSs, employing the model combination which gave the best agreement with the experimental spectra. For the discussion about the fluctuation comparison, see App. B.

For the majority of cases, we used the highest achievable $E_{\text{crit}} = 2.418\,\text{MeV}$. We observe peaks in the $M = 2$ MSC spectra up to $\approx 2\,\text{MeV}$, which are a consequence of transitions from levels around $\approx 2.1 - 2.4\,\text{MeV}$ that could not be described statistically. Below $E_{\text{crit}} = 2.418\,\text{MeV}$ there are 57 tentative, 10 uncertain and 3 unknown J^π assignments out of 130 levels. We tested that these uncertainties do not have a significant influence on our results. Furthermore, the choice of E_{crit} strongly affects the simulated isomeric ratio - see the discussion in Sec. 6.3.

We constructed the simulated MSC spectra for the same range of $E_\Sigma = 7 - 8\,\text{MeV}$ as the experimental ones. In principle, we can use also different ranges - especially $E_\Sigma = 6 - 7\,\text{MeV}$ could be of special interest, as it includes the cascades feeding the isomer (see Fig. 5.5). However, these cascades make up to around 20% of all events in this range, while the rest corresponds to low-energy tail of the full-

energy peak. Hence the MSC spectra constructed from $E_\Sigma = 6 - 7\,\mathrm{MeV}$ range do not provide us with additional useful information, nevertheless, an example of this type of spectra is shown in Fig. 6.14.

Generally, we were unable to simultaneously describe the central interval $E_\gamma \approx 2.5 - 5.0\,\mathrm{MeV}$ of the $M = 2$ MSC spectra for both resonance spins for any of the tested model combinations. In the majority of cases, the simulated intensity in $J = 3$ central part is overestimated.

Here we summarize the main conclusions about the search for optimum LD and PSFs, for details see also App. B. Furthermore, we include additional plots of the MSC spectra that were discussed, but not shown in App. B.

6.2.1 Level Density

The best agreement between the experimental and simulated MSC spectra out of the tested models was obtained for the LD model based on HFB calculations [19]. The overall agreement for $J = 3$ spin is excellent, for $J = 4$ we observe a deviation in the center of the $M = 2$ spectra, see Fig. 6.7.

A slightly worse agreement was provided by the BSFG LD model, as it overestimates the intensity for larger multiplicities $M > 4$, see Fig. 6.8. In addition, it predicts lower intensities of the peaks at the edges of $M = 2$ spectra compared to the model combinations with the HFB LD. The simulated spectra are very similar for both proposed parametrizations of the BSFG (see Sec. 1.2.1). We tested also the influence of even-odd staggering as introduced in Sec. 1.2.1, which we assumed linearly decreasing and vanishing at $E = 4\,\mathrm{MeV}$. The resulting MSC spectra with and without the staggering are nearly identical. The parity dependence of the BSFG LD in the form of Eq. (1.4) yields very small differences in $M = 2$ spectra, but there are no significant changes in the overall agreement.

We were not able to reproduce the experimental MSC spectra with the CTF LD model shown in Fig. 6.9 for any combination of PSFs due to different strength of the SM that was required to describe $M = 2$ and $M > 2$ spectra.

Description of the $M = 2$ spectra, in particular the ratio of the intensity in the center ($E_\gamma \approx 2.5 - 5.0\,\mathrm{MeV}$) versus intensity for the peaks at the edges is probably strongly linked to the shape of the LD model. The predicted number of available levels for $E \approx 2.5 - 5.0\,\mathrm{MeV}$ with respect to $E_\gamma \gtrsim 5.0\,\mathrm{MeV}$ or $E_\gamma \lesssim 2.5\,\mathrm{MeV}$ is higher for the BSFG LD than the CT LD (as can be seen in Fig. 1.1). As a result, the BSFG model overestimates the center of $M = 2$, while at the edges the predicted intensity is lower than experimental one. On the other hand, the opposite situation is observed for the CT LD model. The behavior of the $M = 2$ spectra for the HFB LD model appears to be between the two above-mentioned cases.

6.2.2 *E*1 Photon Strength Function

We tested the $E1$ PSF models introduced in Sec. 2.2 with individually adjusted parameters of $M1$ PSF. We were not able to reproduce the experimental spectra with any model combination including SLO $E1$ PSF, as the intensity in $M = 2$ spectra is majorly overestimated in the central part, see Fig. 6.10, and the multiplicity distribution is shifted towards lower values.

Similar effects in the $M = 2$ spectra were observed also with the SMLO

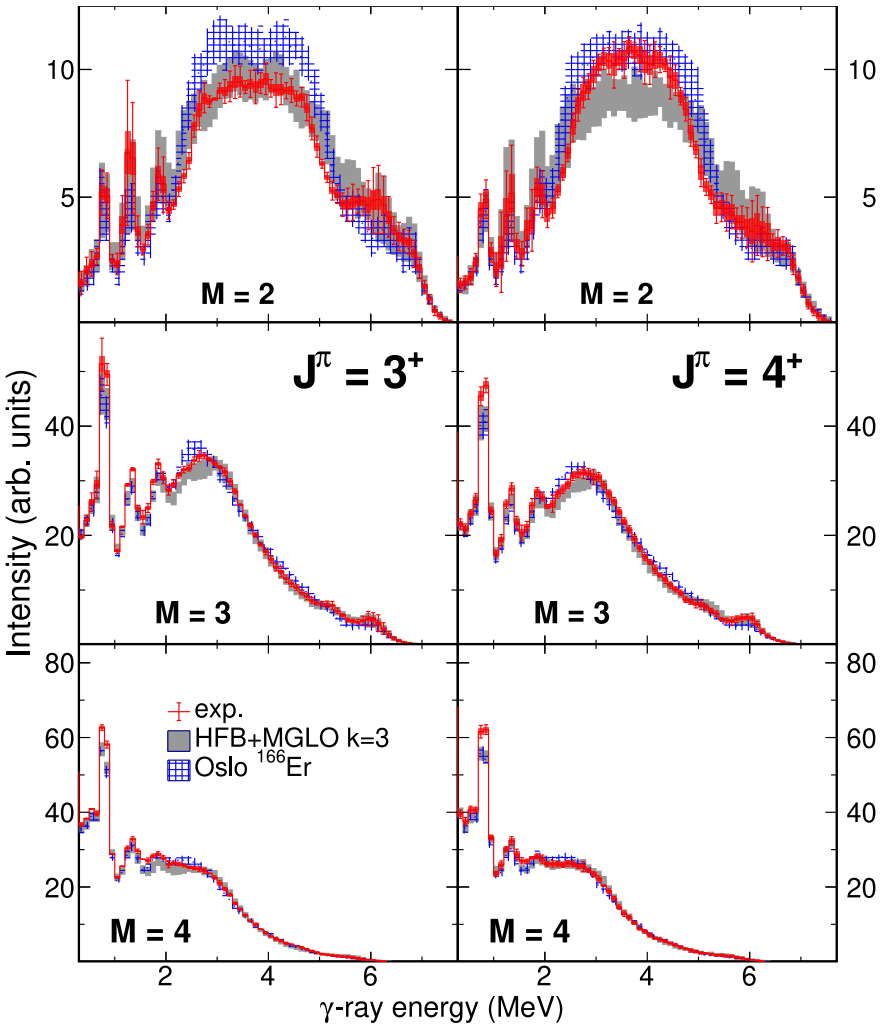

Figure 6.7: Comparison of the mean experimental MSC spectra and the simulated MSC spectra. The best-fitting model combination using HFB LD [19], MGLO ($k = 3$) $E1$ PSF model and adjusted parameters of the SM $E_{\mathrm{SM}} = 3.2\,\mathrm{MeV}$ and $\Gamma_{\mathrm{SM}} = 1.0\,\mathrm{MeV}$ and $\sigma_{\mathrm{SM}} = 0.6\,\mathrm{mb}$ is plotted in grey, while the Oslo model [32] for $E1$ and $M1$ adopting BSFG LD is plotted in blue. The mean experimental intensities and their uncertainties are shown as full red rectangles. The red error bars correspond to the fluctuation of the intensities. The simulated MSC spectra are drawn as a gray (or blue) band corresponding to a two standard deviation corridor centered at the average.

model[59], QRPA+D1M calculated $E1$ PSF[59] (both plotted in Fig. 6.11) and QRPA Skyrme-based calculations [64, 65, 66] with all the tested interactions (Fig. 6.12). However, the situation for these model combinations taken from literature is different, as here the $M1$ PSF was not adjusted but taken from the respective recommended parametrizations or calculations - for discussion of the corresponding $M1$ PSF see Sec.6.2.3 and the references therein.

On the other hand, the EGLO model shifts the average multiplicity to a higher value than the experimental one due to its preference for very low-energy transitions as illustrated in Fig.6.10.

Probably the best agreement was achieved with the MGLO ($k = 3$) model

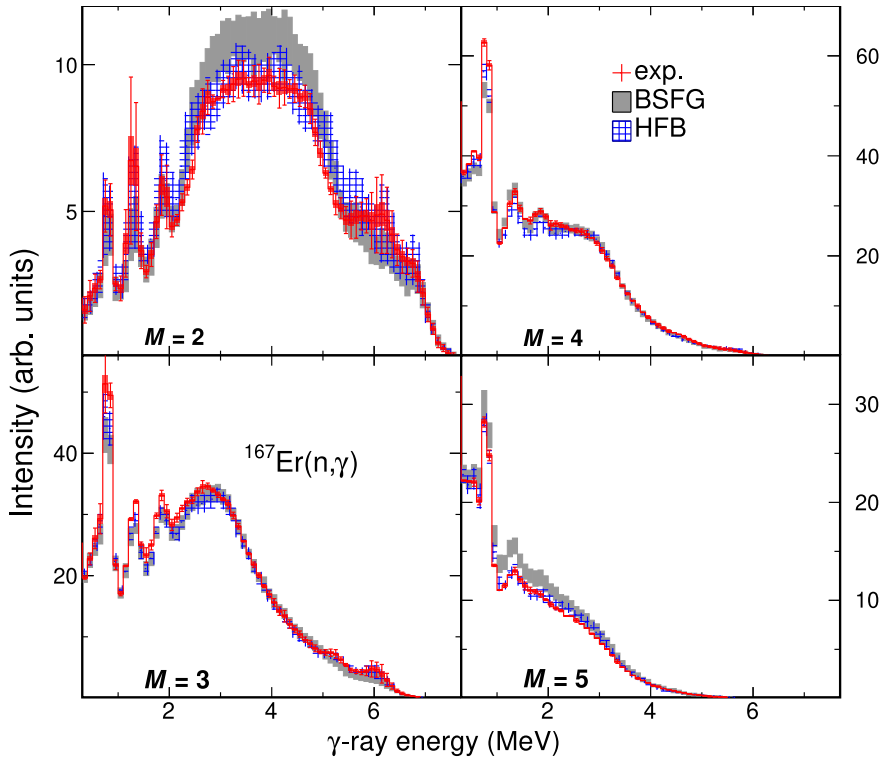

Figure 6.8: Comparison of the mean experimental MSC spectra and the simulated MSC spectra for $J^\pi = 3^+$ resonances and $M = 2 - 5$. The BSFG LD model with parametrization from [18] is plotted in grey, while the HFB LD model [19] in blue. Both models adopted MGLO ($k = 3$) $E1$ PSF model and composite $M1$ PSF model. The SM was adjusted separately for each model combination, the parameters of the SM were $E_{\mathrm{SM}} = 3.2\,\mathrm{MeV}$ and $\Gamma_{\mathrm{SM}} = 0.8\,\mathrm{MeV}$ and $\sigma_{\mathrm{SM}} = 0.45\,\mathrm{mb}$ for the BSFG LD and $E_{\mathrm{SM}} = 3.2\,\mathrm{MeV}$ and $\Gamma_{\mathrm{SM}} = 1.0\,\mathrm{MeV}$ and $\sigma_{\mathrm{SM}} = 0.60\,\mathrm{mb}$ for the HFB LD. The meaning of the symbols is analogous to the Fig. 6.7.

(Fig. 6.13). A reasonable description was also provided by the KMF model and the MGLO ($k = 2$), however, these two models slightly overestimate the intensities in $M > 3$ spectra compared to the MGLO ($k = 3$), see Fig. 6.13.

To examine whether the only acceptable $E1$ PSF models are those violating the Brink hypothesis, we tested the KMF-T model with $T = 0.31$ as proposed in [20] for ^{166}Er, see Fig. 6.7. The agreement is similar to the results obtained for the KMF and the MGLO ($k = 2, 3$) $E1$ PSF models, therefore we cannot reject or confirm the strict validity of the Brink hypothesis. This finding is consistent with the previously studied MSC spectra in even-even Gd [86] and Dy [87], that reported a good agreement using the KMF-T model with $T = 0.3 - 0.4\,\mathrm{MeV}$.

6.2.3 $M1$ Photon Strength Function

We tested the composite model of $M1$ PSF in the form $f^{(M1)} = f_{\mathrm{SP}}^{(M1)} + f_{\mathrm{SM}}^{(M1)} + f_{\mathrm{SF}}^{(M1)}$. The best agreement was obtained with a very small SP contribution of $f_{\mathrm{SP}}^{(M1)} \lesssim 2 \times 10^{-9}\mathrm{MeV}^{-3}$, as higher $f_{\mathrm{SP}}^{(M1)}$ shifts the multiplicity distribution towards too large values. All the MSC spectra are plotted with $f_{\mathrm{SP}}^{(M1)} = 0$.

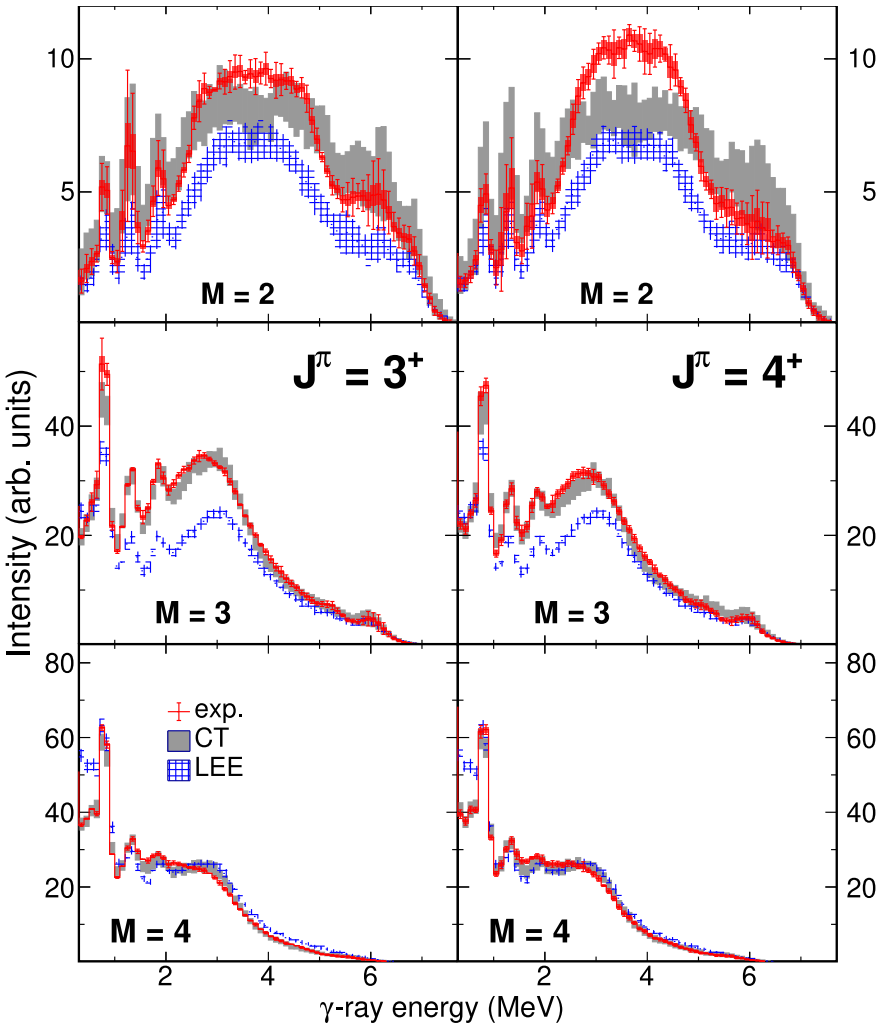

Figure 6.9: Comparison of the mean experimental MSC spectra and the simulated MSC spectra. The CT LD model with parametrization from [18] is plotted in grey, while the BSFG LD model with the LEE postulated in $M1$ PSF is plotted in blue. Both models adopted MGLO ($k = 3$) $E1$ PSF model. The SM was adjusted separately for each model combination. The meaning of the symbols is analogous to the Fig. 6.7.

$f_{\mathrm{SF}}^{(M1)}$ was adopted as a double-Lorentzian structure with $E_{\mathrm{SF}_{1,2}}$ and $\Gamma_{\mathrm{SF}_{1,2}}$ taken from [89].

A hint of a resonance around 3 MeV in the PSF is already anticipated from the prominent peak in $M = 3$ MSC spectra at the corresponding energy. We were not able to reproduce the spectra without postulating the SM resonance at ≈ 3 MeV in the $M1$ PSF.

We adopted the SM resonance in a Lorentzian form of Eq. (2.13) and searched for the suitable range of SM parameters in combination with the above-discussed $E1$ PSF models providing a reasonable description of the spectra (MGLO with $k = 2, 3$ and KMF). The acceptable ranges of SM parameters were found to be $E_{\mathrm{SM}} = 3.1-3.3$ MeV and $\Gamma_{\mathrm{SM}} = 0.8-1.3$ MeV almost independently of the chosen $E1$ PSF model. On the other hand, σ_{SM} scales with the absolute value of $f^{(E1)}$, the allowed strength for the MGLO ($k = 3$) is $\sigma_{\mathrm{SM}} = 0.4 - 0.6$ mb.

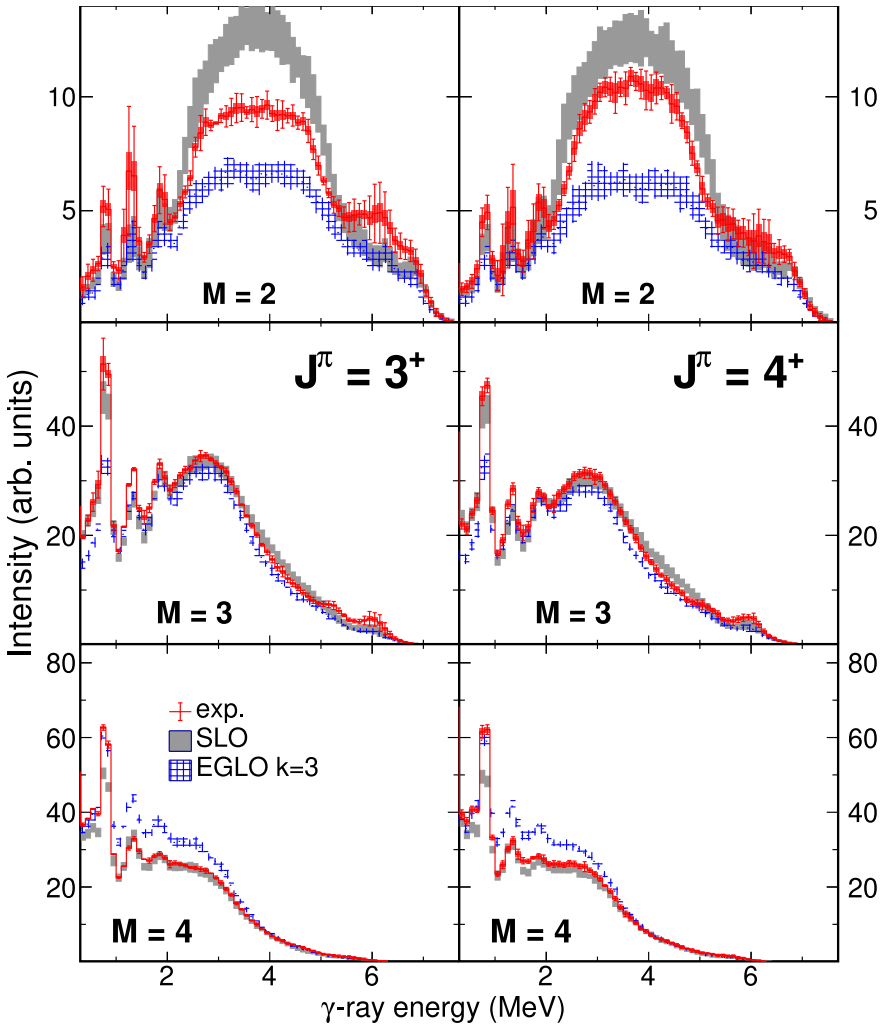

Figure 6.10: Comparison of the mean experimental MSC spectra and the simulated MSC spectra. The SLO $E1$ PSF model is plotted in grey, while the EGLO ($k = 3$) $E1$ PSF model is plotted in blue. Both models adopted BSFG LD model and composite $M1$ PSF model. The SM was adjusted separately for each model combination. The meaning of the symbols is analogous to the Fig. 6.7.

As mentioned above, the presented MSC spectra are rather sensitive to the position of the SM resonance. Therefore the microscopic $M1$ models predicting the SM resonance at a different energy - such as Skyrme calculations with SkI3, SLy6 or SkP (see the Appendix in App. B) - cannot describe the $\approx 3\,\mathrm{MeV}$ peak in $M = 3$ spectra, see Fig. 6.12.

To analyze the possibility of the LEE contribution to the $M1$ PSF, we adopted $f^{(M1)} = f^{(M1)}_{\mathrm{LEE}} + f^{(M1)}_{\mathrm{SM}} + f^{(M1)}_{\mathrm{SF}}$ with the LEE part in the same form and using the same parameter values as proposed in ^{151,153}Sm [92]. We were not able to reproduce the experimental MSC spectra with LEE for any combination of LD and $E1$ PSF models as it majorly overestimates the intensity in higher multiplicities $M > 4$, see Fig. 6.9.

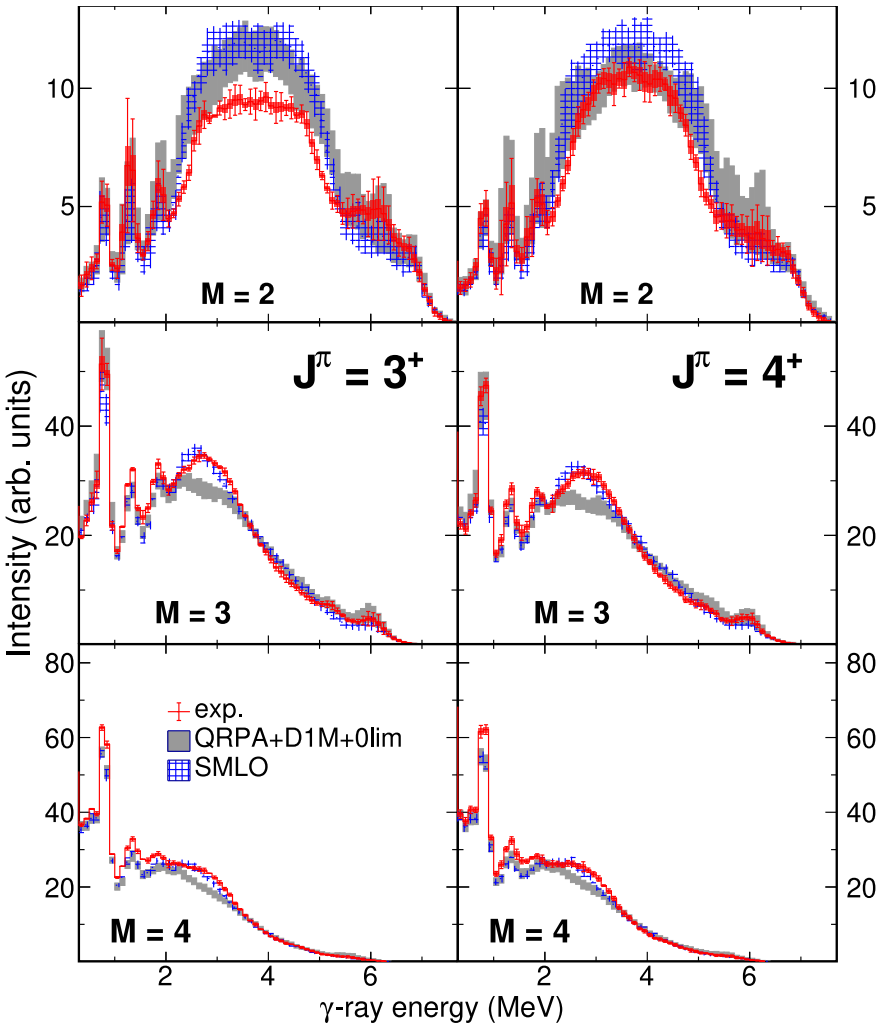

Figure 6.11: Comparison of the mean experimental MSC spectra and the simulated MSC spectra. The QRPA+D1M calculations of $E1$ and $M1$ PSF [63] plus the HFB LD model [19] is plotted in grey while SMLO model [63] for $E1$ and $M1$ PSF plus BSFG LD is plotted in blue. The meaning of the symbols is analogous to the Fig. 6.7.

6.2.4 Average Radiative Width

The only detector-independent simulated quantity in DICEBOX is the average radiative width $\overline{\Gamma}_\gamma$, which depends on the absolute values of PSFs. It is expressed as a sum of contributions from all involved transition types and multipolarities, i.e. in our case $\overline{\Gamma}_\gamma = \overline{\Gamma}_\gamma^{(E1)} + \overline{\Gamma}_\gamma^{(M1)} + \overline{\Gamma}_\gamma^{(E2)}$. Due to PT fluctuations of the primary transitions, Γ_γ from individual neutron resonances differ from the mean value - this difference reaches at most a few percent. The reported value for ^{167}Er from the Atlas [128] is $\overline{\Gamma}_\gamma = 91.0(16)$ meV.

It is important to note that there are two available GEDR parametrizations obtained from the fit on (γ, xn) data for $^{\mathrm{nat}}$Er - one from the compilation of Dietrich and Berman [43] and the other one from RIPL-3 [21] (and a recent review [133]), see Fig. 6.15. While their shape below S_n is almost identical, they significantly differ in the absolute value of the $E1$ PSF. The RIPL-3 [21]

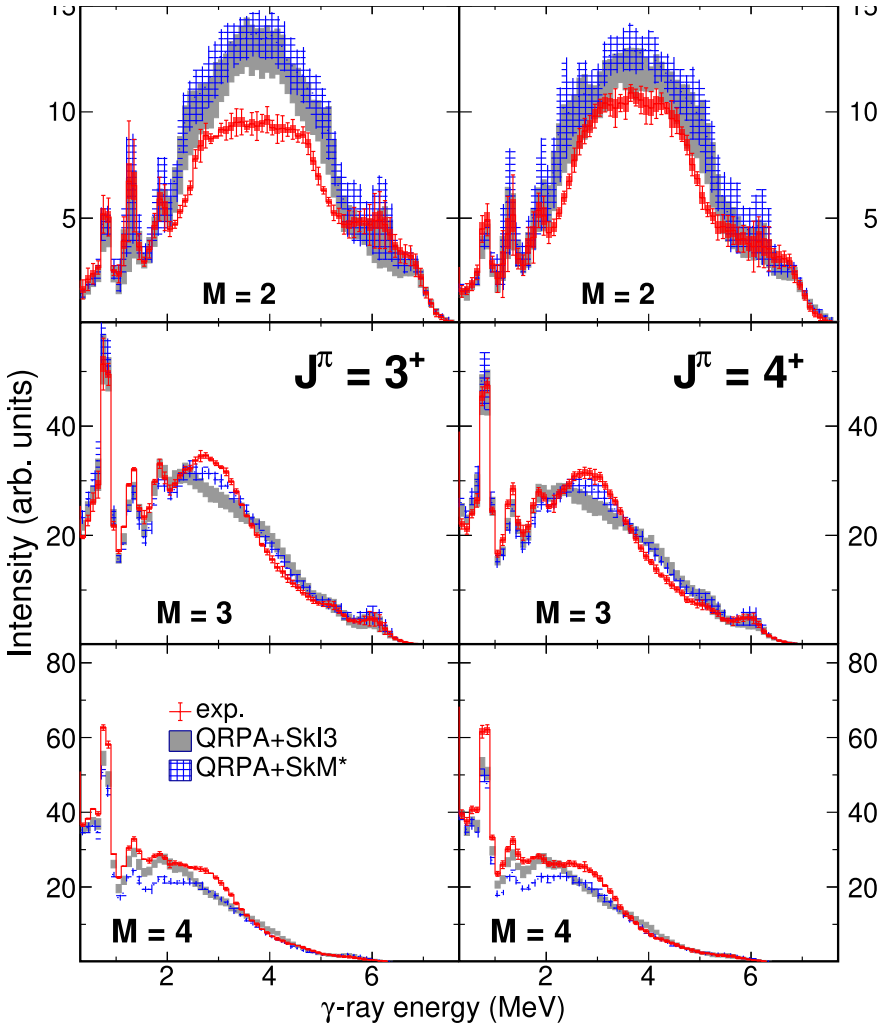

Figure 6.12: Comparison of the mean experimental MSC spectra and the simulated MSC spectra. The QRPA+SkI3 model for $E1$ and $M1$ is plotted in grey, while the QRPA+SkM* model for $E1$ and $M1$ is plotted in blue. Both models adopted the HFB LD [19]. The meaning of the symbols is analogous to the Fig. 6.7.

parametrization yields approximately 1.35 × larger $\overline{\Gamma}_\gamma$ than the one from Dietrich and Berman [43]. The $\overline{\Gamma}_\gamma^{(E1)}$ value for $^{\text{nat}}$Er from Ref. [43] parametrization is $\approx$ 10% larger compared to the ^{160}Gd parametrization [43] that was used in the previously published analyses of the MSC spectra for Gd and Dy isotopes [87, 62].

The $\overline{\Gamma}_\gamma$ also depends on the adopted LD model. The HFB LD model yields unrealistically different values for each resonance spin - this is the consequence of a strong even-odd staggering persisting up to S_n energy. A very different spin distribution of neutron resonances in the HFB model compared to other ones is visible from Fig. 10 of the App. A. For a fixed PSF model, the BSFG LD gives about two times larger $\overline{\Gamma}_\gamma$ than the CT LD. The HFB model for $J = 3$ resonances predicts $\overline{\Gamma}_\gamma$ almost identical to the BSFG, while for $J = 4$ it is about 70% of the value. The SM contributes to the total $\overline{\Gamma}_\gamma$ with $\approx$ 15%.

The MGLO ($k = 3$) $E1$ PSF combined with the $M1$ PSF composite model

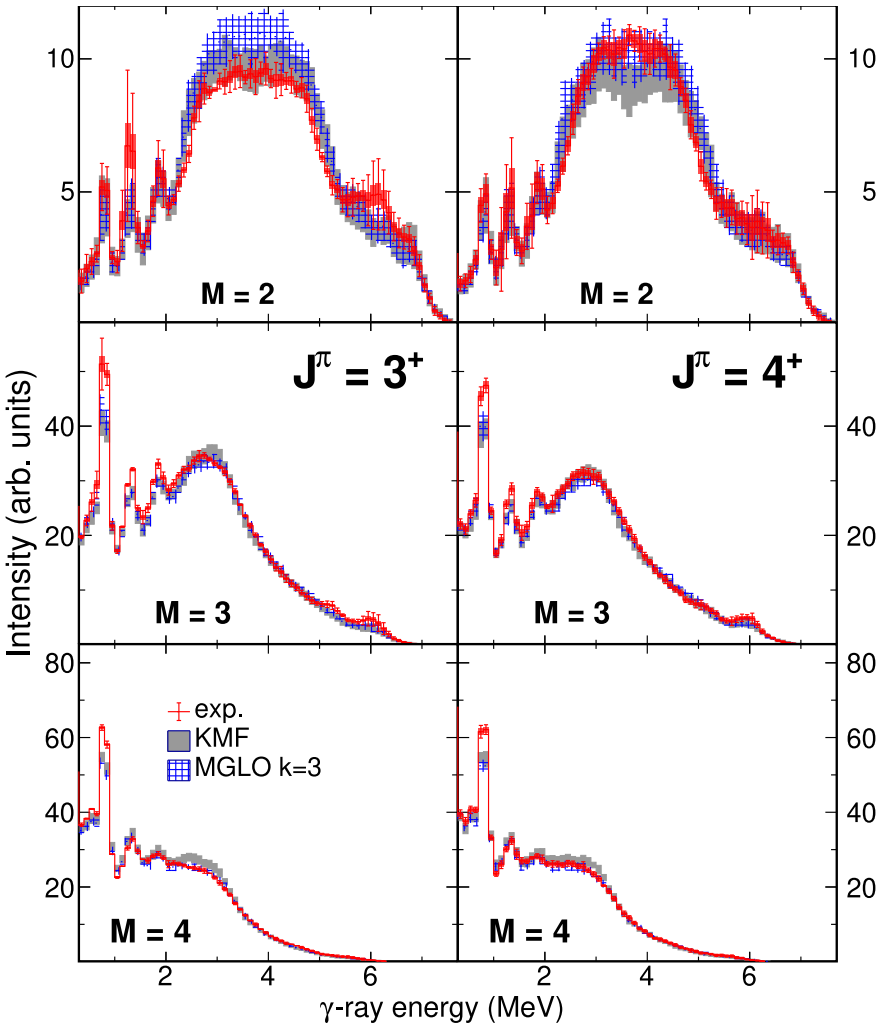

Figure 6.13: Comparison of the mean experimental MSC spectra and the simulated MSC spectra. The KMF $E1$ PSF model is plotted in grey, while the MGLO ($k = 3$) $E1$ PSF model is plotted in blue. Both models adopted the BSFG LD and the composite $M1$ model with separately adjusted parameters of the SM. The meaning of the symbols is analogous to the Fig. 6.7.

and BSFG LD yields $\overline{\Gamma}_\gamma \approx 125\,\text{meV}$ with the parametrization from Ref. [43], not consistent with the above-presented reported value [128]. This finding indicates that the absolute PSF below S_n might be inappropriate and/or the actual LD model has a different energy dependence for the spins relevant to the decay of neutron resonances. The absolute value of $\overline{\Gamma}_\gamma$ thus could not be used in our analysis to further restrict the acceptability of the tested model combinations.

6.2.5 Comparison of SM Strength with Other Data

The acceptable SM (or total $M1$) strength obtained from the analysis of the MSC spectra can be compared to the experimental data obtained in the NRF and Oslo-type experiments. The MSC spectra are sensitive only to the relative E_γ dependence of the PSFs, therefore the absolute SM strength scales with the adopted parametrization of the GEDR. As mentioned above, the two available

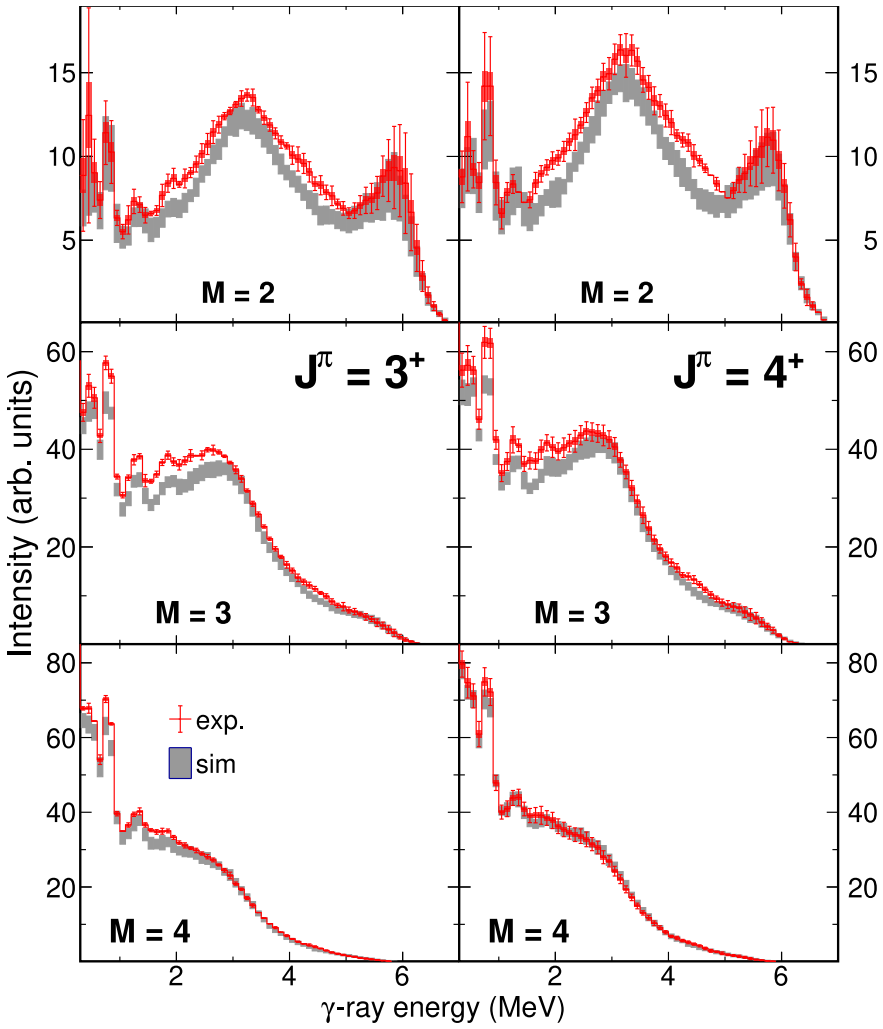

Figure 6.14: Comparison of the mean experimental MSC spectra and the simulated MSC spectra using the $E_\Sigma = 6 - 7\,\mathrm{MeV}$ range. The best-fitting model combination using HFB LD [19], MGLO ($k = 3$) $E1$ PSF model and adjusted parameters of the SM $E_{\mathrm{SM}} = 3.2\,\mathrm{MeV}$ and $\Gamma_{\mathrm{SM}} = 1.0\,\mathrm{MeV}$ and $\sigma_{\mathrm{SM}} = 0.6\,\mathrm{mb}$ is plotted in grey. The meaning of the symbols is analogous to the Fig. 6.7. Note the normalization factor for these spectra is the same as for the MSC constructed from $E_\Sigma = 7 - 8\,\mathrm{MeV}$ range.

parametrizations [43, 21] differ in the absolute value by a factor of about 1.35. Unfortunately, as discussed in Sec. 6.2.4, the obtained average radiative width does not help us to constrain the GEDR parametrization. All the SM strengths described below correspond to the GEDR parametrization from Ref. [43].

To compare with the NRF obtained strength, we determined the total $M1$ contribution of reduced transition probabilities $\sum B^{(M1)}$ in the region $E_\gamma = 2.7 - 3.7\,\mathrm{MeV}$, calculated from the SM+SF composite $M1$ PSF with no SP part assumed. The SM contributes to the total $\sum B^{(M1)}$ by $\approx 90\%$. The comparison with the even-even isotopes of Gd, Dy, and Er is shown in Fig. 6.16, our derived value is in perfect agreement with the NRF one and compatible with neighboring nuclei.

Furthermore, we calculated the total SM strength $\sum B_{\mathrm{SM}}$ by integrating the

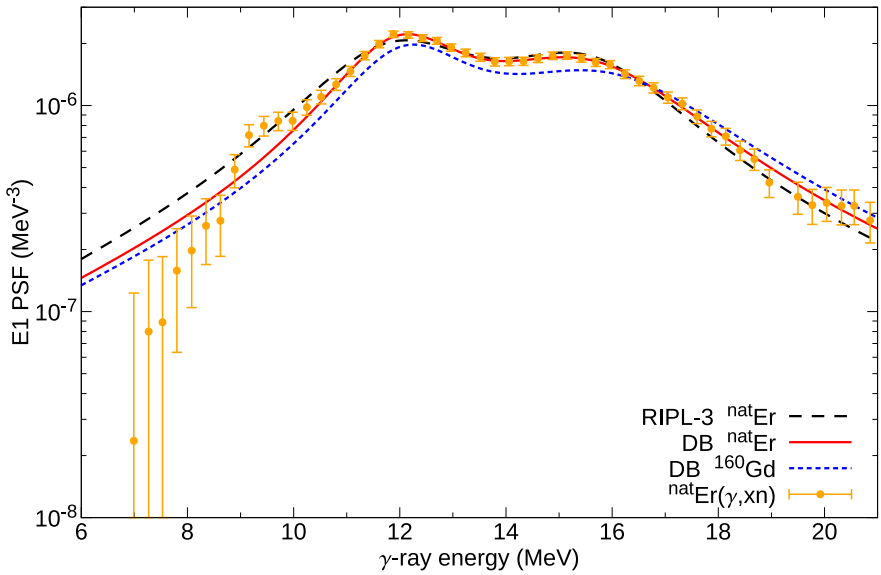

Figure 6.15: Experimental (γ, xn) data for $^{\text{nat}}$Er and two available parametrizations of the GEDR - Dietrich and Berman compilation from Ref. [43] and RIPL-3 from Ref. [21], for comparison also parametrization for ^{160}Gd from Ref. [43] is plotted.

SM resonance over the interval 0-10 MeV and compared it to the results from ^{3}He induced experiments using the Oslo method for even-even Gd, Dy, and Er. We assumed the $M1$ character of the reported pygmy resonance in Er at ≈ 3 MeV. Note that there was no Oslo measurement for ^{168}Er, only for ^{166}Er. Our result is consistent with the values observed for even-even nuclei with $A \geq 160$, if we consider the former Dy data [88], see Fig. 6.16.

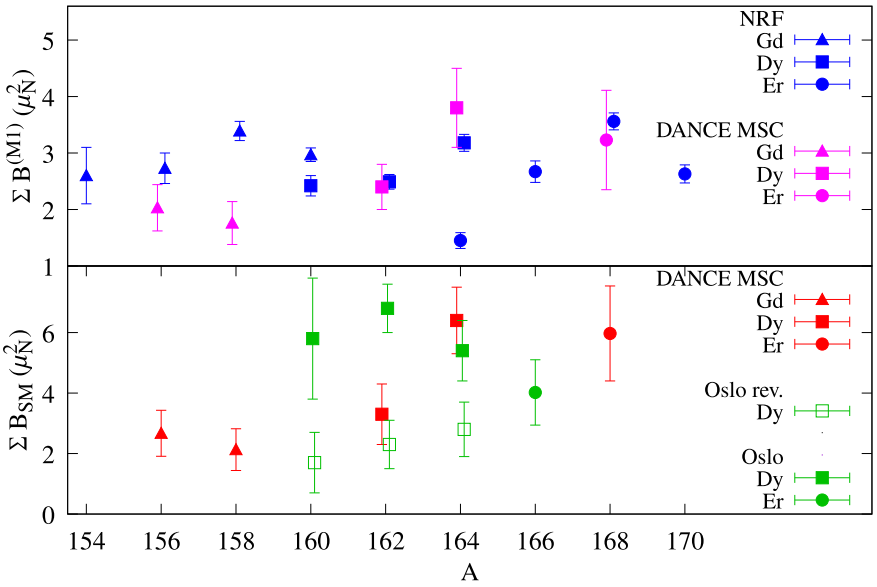

Figure 6.16: Top panel: The total M1 strength $\sum B^{(M1)}$ summed over $E_\gamma = 2.7 - 3.7\,\mathrm{MeV}$ for even-even isotopes of Gd, Dy and Er as a function of mass number A. Data from (γ, γ') measurements [81, 77] are plotted together with our result for ^{168}Er and data from Gd [134] and Dy [87] analyses of the MSC spectra. Bottom panel: Comparison of the total SM strength $\sum B_{\mathrm{SM}}$ integrated for $E_\gamma = 0 - 10\,\mathrm{MeV}$. Values from Oslo method for ^{166}Er [32], Dy [51, 53] and revisited Dy [88] are plotted together with data for ^{168}Er, Gd [134], and Dy [87] analyses of the MSC spectra.

6.3 Isomeric Ratio

Statistical γ decay of ^{168}Er is significantly influenced by the presence of an isomeric state at 1094 keV. It is a K-isomer with $J^\pi = 4^-$ and a bandhead of the $K = 4$ rotational band. Its half-life from the ENSDF evaluation of ^{168}Tm ϵ decay [104] is $T_{1/2} = 109.0(7)$ ns. One of the quantities of interest related to isomers is the isomeric ratio, i.e. the relative number of γ cascades going via the isomeric state over all γ cascades going to the ground state. We determined the experimental isomeric ratio for several resonances of both spins and compared it to simulated isomeric ratio for the tested model combinations of LD and PSFs.

6.3.1 Experimental Isomeric Ratio

From the time-difference spectra and their fit introduced in Sec. 5.2.2, we obtained results on the isomeric decay listed in Tab. 6.4. The experimental isomeric ratio was calculated using the form of Eq. (5.1) for 6 resonances of $J^\pi = 3^+$ and 5 resonances of $J^\pi = 4^+$. In addition, we used an off-resonance range of $E_n = 0.2 - 0.25$ with a contribution from captures on both resonance spins - about 23% of $J^\pi = 3^+$ based on [128].The uncertainties come from the fit for $T_{1/2}$ and $N_{\rm iso}$, and are assumed Poisson for $N_{\rm pr}$. All but one value of half-life are 2σ compatible with the literature value $T_{1/2} = 109.0(7)$ ns [104].

The individual values of $R_{\rm iso}$ are expected to fluctuate, we thus determined the average $R_{\rm iso} = 14.5(8)\%$ and $25.0(14)\%$ and the width of the distribution $\sigma_{R_{\rm iso}} = 1.7(6)\%$ and $2.5(10)\%$ for $J^\pi = 3^+$ and 4^+ resonances, respectively. Considering the experimental uncertainties, the expectation values and the width of the distribution were obtained using the maximum likelihood fit similarly as for the experimental MSC spectra. Using the average values for each spin and the corresponding spin contributions, we obtained $R_{\rm iso} = 22.6(11)\%$ in the $E_n = 0.2 - 0.25\,$eV range, which is consistent with the value $23.6(3)\%$ obtained from the fit.

The $R_{\rm iso}$ value from the ENSDF evaluation (n_{th}, γ) at the thermal point is $26.6(10)\%$ [104]. Weighting our values by contributions of each resonance group to the thermal point, which are 215.9 b and 426.3 b [128] for $J^\pi = 3^+$ and $J^\pi = 4^+$, respectively, yields $21.4(10)\%$. These value are not compatible, however, we have two comments regarding this outcome. First, the intensities of the isomeric decay from Ref. [104] are given as an average from two measurements, where the newer measurement reports the intensities systematically smaller by about 5-10% than the average. Second, the obtained $\sigma_{R_{\rm iso}}$ values indicate that the fluctuations of $R_{\rm iso}$ are rather large. The largest contribution to the thermal point is given by the $J^\pi = 4^+$ resonance at 0.460 eV with $\approx 160\,$b and $J^\pi = 3^+$ resonance at 0.584 eV with $\approx 425\,$b. Unfortunately, due to high number of busy crystals, we were not able to determine the $R_{\rm iso}$ for these two resonances.

6.3.2 Simulated Isomeric Ratio

We obtained the simulated $R_{\rm iso}$ as the simulated population of the isomeric state using the best-fitting model combination of LD and PSF presented in Fig. 6.7. We generated 50 NRs within each of 50 NSs to account for fluctuations from both NRs and NSs. To examine the applicability of the statistical model to reproduce the experimental $R_{\rm iso}$, we determined the simulated $R_{\rm iso}$ as a function of $E_{\rm crit}$,

J^π	E_{res} (eV)	$T_{1/2}$ (ns)	N_{iso} (x10^2)	N_{pr} (x10^2)	R_{iso} (%)
3^+	22.02	112.4(28)	681(21)	7446	17.3(5)
	39.43	103.0(31)	1021(43)	14045	13.8(6)
	42.23	107.4(41)	471(34)	5872	15.2(11)
	59.96	109.8(46)	685(60)	9325	13.9(12)
	85.42	106.9(118)	39(6)	487	15.3(22)
	107.6	109.8(28)	421(15)	6701	11.9(4)
4^+	50.19	105.8(34)	972(63)	8822	20.6(10)
	69.43	117.4(46)	232(11)	1605	27.1(13)
	91.20	119.1(61)	163(11)	1251	24.4(17)
	184.7	123.1(61)	192(15)	1334	26.9(21)
	217.2	121.4(76)	84(9)	556	28.3(29)
-	0.2-0.25	109.2(18)	75870(27)	9536(24)	23.6(3)

Table 6.4: The experimental results on the isomeric decay, including the obtained half-life $T_{1/2}$, number of detected isomeric decays N_{iso}, number of detected prompt cascades N_{pr} and the obtained isomeric ratio R_{iso} for 6 resonances of $J^\pi = 3^+$ and 5 resonances of $J^\pi = 4^+$ and one off-resonance region.

the results for both resonance spins are shown in Fig. 6.17. If we do not assume any structural effects above the isomer, i.e. we adopt the E_{crit} just above 1094 keV, the simulated R_{iso} is significantly lower than the experimental one.

We observe an increase in the simulated R_{iso} with increasing E_{crit}, which is related to the presence of the levels that dominantly feed the isomer. Hereafter, we will refer to these levels that directly or indirectly feed the isomer with at least 80% of the branching intensity as the *doorway levels*. The level scheme below the maximum E_{crit} taken from [104] is shown in Fig. 6.18. It illustrates an example of a doorway and a non-doorway level with the same J^π that are very close in excitation energy, but have a very different decay pattern. While the doorway level at 1773.20 eV decays directly to the isomer and its rotational band, the 1760.76 eV non-doorway level decays to the lowest-lying positive-parity rotational bands. Including of a doorway level at low energy leads to an increase of the simulated R_{iso} by a few percent, see Fig. 6.17. On the contrary, the population of a single level near the highest E_{crit} is 0.4% at maximum and it decreases exponentially, therefore a single doorway level at higher energy does not induce such a strong effect. The Fig. 6.19 illustrates the statistical behavior of the simulated populations at higher excitation energies $E_{\mathrm{exc}} \geq 1.5$ MeV, where the exponential fit gives a very reasonable description. Below this region we observe levels with larger populations that clearly cannot be described exclusively within the statistical model. An illustration of how increasing the E_{crit} leads to a larger feeding of the isomeric state can be also observed in the sum-energy spectra in Fig. 6.20, where the simulated intensity in the 6.6 MeV peak is much larger for higher E_{crit}.

From Fig. 6.17 we observe increase of R_{iso} up to highest adopted E_{crit} for $J^\pi = 4^+$ and $E_{\mathrm{crit}} \approx 2.3$ MeV for‘$J^\pi = 3^+$ resonances. This finding indicates that the

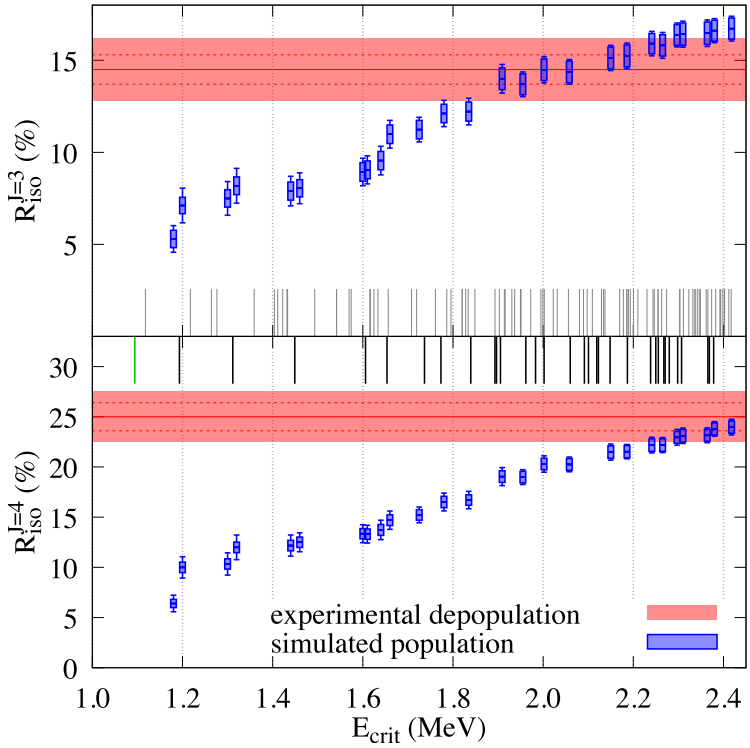

Figure 6.17: Simulated R_{iso} as a function of the critical energy for capturing state spin $J = 3$ (upper panel) and 4 (lower panel). The average from the experimental R_{iso} is drawn as a red line, uncertainty of the average as a dashed line and the red band represents the fluctuations $\sigma_{R_{\mathrm{iso}}}$. The fluctuations of the simulated R_{iso} over NRs within a single NS are plotted as blue rectangles, while the error bars correspond to the total fluctuations from all NRs. The excitation energies of the isomer, doorway levels and non-doorway levels are marked by the green, black and gray lines, respectively.

statistical description of the γ decay is not fully adequate for levels even up to excitation energies close to the maximum E_{crit}. It was not possible to go up to higher $E_{\mathrm{crit}} > 2.4\,\mathrm{MeV}$ as the information about the levels definitely becomes incomplete in this region.

The R_{iso} dependence on E_{crit} is similar for other model combinations reasonably reproducing the MSC spectra, the BSFG LD yields R_{iso} values smaller by about 10% than the presented ones with the HFB LD (see Fig. 6.7). It is evident from the Fig. 6.17 that simultaneous reproduction of the isomeric populations for both spins is problematic - the simulated population for $J^{\pi} = 3^{+}$ resonances for the highest E_{crit} is already above the experimental average, while for $J^{\pi} = 4^{+}$ slightly below the experimental average. The discrepancies are on the level of two to three standard deviations for the worse spin. This finding is consistent with the trends observed in the MSC spectra, where we were unable to describe $M = 2$ spectra perfectly for both spins.

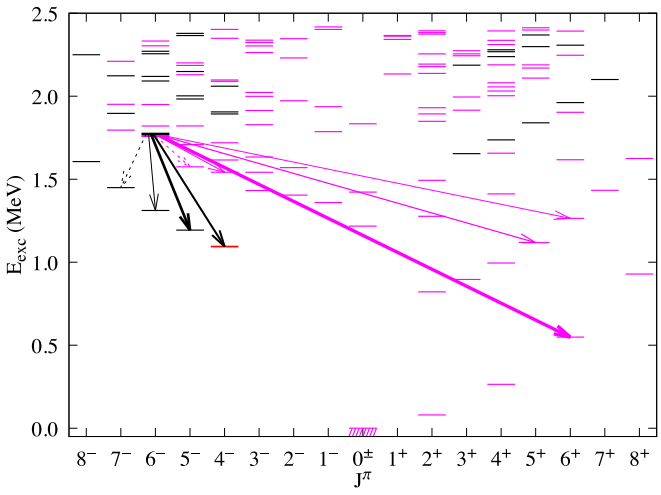

Figure 6.18: The low-lying level scheme of ^{168}Er with the decay of the $J^\pi = 6^-$ non-doorway level at 1760.76 keV (magenta) and the 6^- doorway level at 1773.20 keV (black). The isomer is drawn in red, the doorway levels are in black and the other levels in magenta.

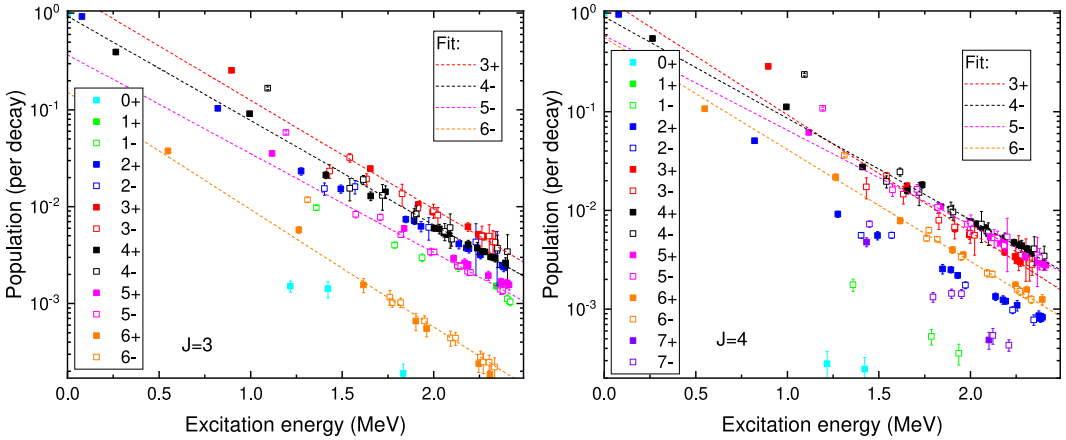

Figure 6.19: Simulated populations of the levels as a function of the excitation energy of the level, the left panel corresponds to $J^\pi = 3^+$ resonance and the right panel to $J^\pi = 4^+$ resonance. The illustrative exponential fits performed at the excitation energy range above 1.5 MeV for the given spin and parity are plotted as dashed lines.

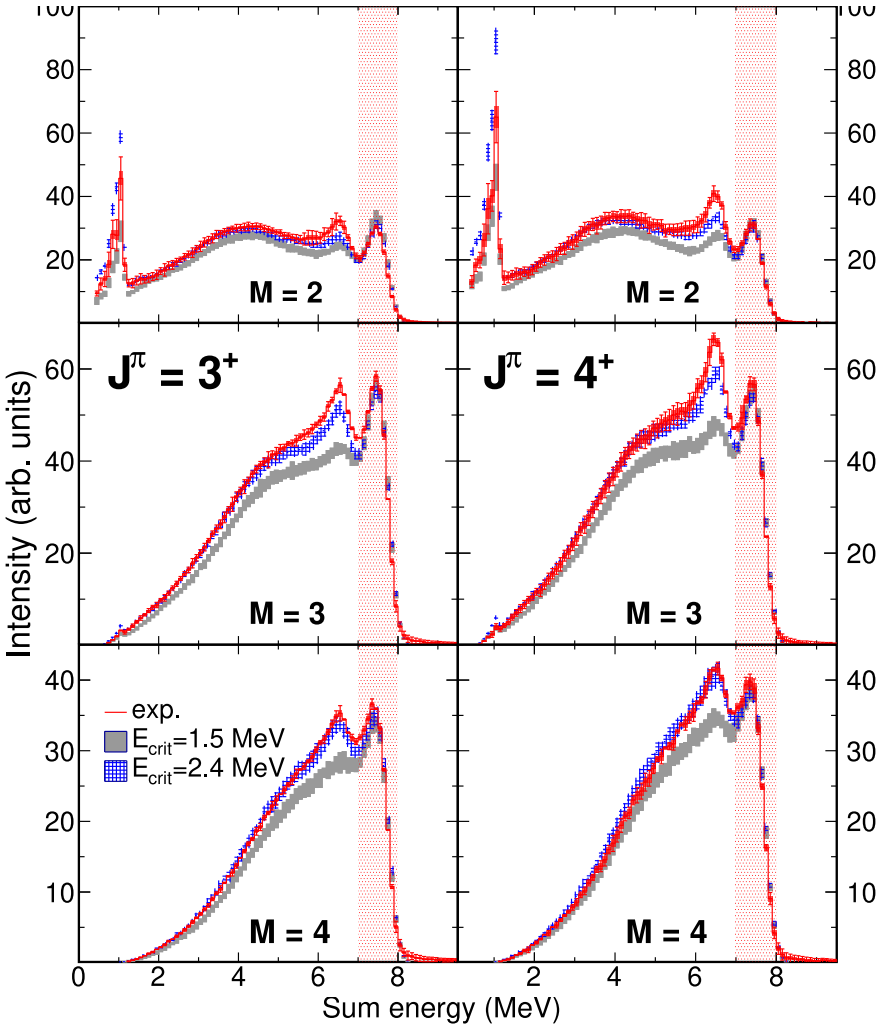

Figure 6.20: Mean experimental sum-energy spectra for $M = 2 - 4$ and resonance spins $J^\pi = 3^+, 4^+$ compared to the simulated spectra for the best model combination given in Fig. 6.7, plotted for two different E_{crit}. The E_Σ range used to construct the MSC spectra is illustrated as a red band.

Conclusions and Outlook

Coincident γ-ray spectra from the neutron capture $^{167}\mathrm{Er}(n,\gamma)^{168}\mathrm{Er}$ on s-wave resonances of both spins were measured with the DANCE detector at LANSCE spallation neutron source. The calorimetric capabilities of the detector enabled us to assign spin to neutron resonances and perform the analysis of their fluctuation properties. We analyzed the completeness of the observed resonance sequences using properties of the Porter-Thomas distribution of neutron widths and resonance position predictions from GOE. The constructed γ-ray multi-step cascade spectra were used to test the validity of various LD and PSF models within the statistical approach. The DANCE setup allowed us to detect the decay of the isomeric state at 1094 keV with 109 ns half-life present in ^{168}Er and to determine the experimental isomeric ratio, which was compared with the simulated one using the statistical model.

The main results can be summarized as follows:

- The analysis of the completeness of observed resonance sequences based on their fluctuation properties predicted from GOE indicates a very restricted sensitivity to estimate the number of missing resonances. Furthermore, we cannot expect completeness for sequences consisting of more than a few tens of resonances for well-deformed rare-earth odd-mass targets. Nevertheless, assuming corrections to the number of missing resonances, we determined the average level spacing D_0 =3.86(12) eV for the s-wave resonances of ^{167}Er.

- The best description of the LD was obtained with the HFB model [19], contrary to the previous analyses of the MSC spectra [86, 87] where the BSFG LD model was preferred. The BSFG model yields slightly worse prediction than the HFB, but significantly better than the CT model. The $E1$ PSF was well reproduced using the MGLO ($k = 2, 3$), KMF, and KMF-T model. The resonance structure at $\approx 3.1 - 3.3$ MeV in $M1$ PSF was definitely necessary for the reproduction of the spectra and it was identified as the scissors mode. Its strength is likely comparable to the neighboring even-even rare-earth nuclei. Simultaneous description of the MSC spectra for both spins was found to be rather difficult.

- The QRPA+D1M and SMLO model combinations of PSFs proposed in the recent PSF review [63] do not reproduce the measured MSC spectra. A similar conclusion can be made for PSFs based on the QRPA calculations with several different parametrizations of the Skyrme interaction [64, 65, 66]. On the other hand, the PSFs obtained from the (^{3}He,^{3}He'γ)^{166}Er measurement [32] using the Oslo method provide a rather good description, which was not achieved with the Oslo-derived PSFs in the previous MSC analyses of rare-earth nuclei.

- The simulated isomeric ratio is significantly lower than the experimental one if no structure effects are assumed above the excitation energy of the isomer. In contrast to previous analyses[10, 11, 12], we were able to reproduce

the experimental isomeric ratio on the level of about two standard deviations if we adopt the decay scheme up to excitation energy well above 2 MeV. This finding indicates that the structure effects play a role up to high excitation energies.

Despite the finding that the structure effects influence the γ decay up to at least 2 MeV in ^{168}Er, the overall reasonable description of the experimental MSC spectra indicates that the commonly-used statistical approach is at least a good approximation at energies above about 2.0-2.4 MeV. Further studies of the applicability of the statistical model can be hopefully performed using the DANCE calorimeter, which has been proven to be a useful tool to measure isomeric decay in rare-earth nuclei.

The MSC data for the neighboring ^{167}Er and ^{170}Tm were recently also measured by DANCE and their ongoing analysis should allow us to study the LD and PSFs and establish the systematics of the scissors mode for well-deformed rare-earth nuclei. For ^{167}Er, the results could also be compared to the (^{3}He,^{3}He'γ)^{167}Er Oslo-type measurement [32].

Bibliography

[1] E. Fermi *et al.*, Proc. of the R. Soc. of London. Ser. A **146**, 483 (1934).

[2] E. Amaldi *et al.*, Proc. of the R. Soc. of London. Ser. A **149**, 522 (1935).

[3] N. Bohr, Nature **137**, 344 (1936).

[4] N. Bohr, Science **86**, 161 (1937).

[5] F. Bečvář, Ph.d. thesis, unpublished, (1992).

[6] E. P. Wigner, Ann. Math. **67**, 325 (1958).

[7] C. E. Porter, *Statistical theories of spectra: fluctuations* (Academic, New York, 1965).

[8] A. M. Lane and J. E. Lynn, Nucl. Phys. **11**, 646 (1959).

[9] G. C. Baldwin and G. S. Klaiber, Phys. Rev. **71**, 3 (1947).

[10] X. Ledoux *et al.*, Eur. Phys. J. A **27**, 59 (2006).

[11] D. Denis-Petit *et al.*, Phys. Rev. C **94**, 054612 (2016).

[12] K. Wisshak *et al.*, Phys. Rev. C **73**, 045807 (2006).

[13] H. A. Bethe, Phys. Rev. **50**, 332 (1936).

[14] A. Gilbert and A. G. W. Cameron, Can. J. Phys. **43**, 1446 (1965).

[15] T. Ericson, Adv. Phys. **9**, 425 (1960).

[16] S. I. Al-Quraishi *et al.*, Phys. Rev. C **67**, 015803 (2003).

[17] T. von Egidy and D. Bucurescu, Phys. Rev. C **72**, 044311 (2005), Erratum in Ref. [135].

[18] T. von Egidy and D. Bucurescu, Phys. Rev. C **80**, 054310 (2009).

[19] S. Goriely, S. Hilaire, and A. J. Koning, Phys. Rev. C **78**, 064307 (2008).

[20] E. Melby *et al.*, Phys. Rev. C **63**, 044309 (2001).

[21] R. Capote *et al.*, Nucl. Data Sheets **110**, 3107 (2009).

[22] A. J. Koning, S. Hilaire, and S. Goriely, Nucl. Phys. A **810**, 13 (2008).

[23] Y. Alhassid, L. Fang, and H. Nakada, Phys. Rev. Lett. **101**, 082501 (2008).

[24] C. Özen, Y. Alhassid, and H. Nakada, Phys. Rev. C **91**, 034329 (2015).

[25] B. V. Zhuravlev *et al.*, Yad. Fiz. **39**, 264 (1984).

[26] B. V. Zhuravlev *et al.*, in *Proc. of VI Int. Sem. on Inter. of Neutr. with Nucl.* (Dubna, 1998).

[27] A. Wallner, B. Strohmaier, and H. Vonach, Phys. Rev. C **51**, 614 (1995).

[28] J. Rekstad *et al.*, Phys. Scr. **T5**, 45 (1983).

[29] M. Guttormsen, T. Ramsøy, and J. Rekstad, Nucl. Instrum. Methods A **255**, 518 (1987).

[30] A. Schiller *et al.*, Nucl. Instrum. Methods A **447**, 494 (1999).

[31] M. Guttormsen *et al.*, Nucl. Instrum. Methods A **374**, 371 (1996).

[32] E. Melby *et al.*, Phys. Rev. Lett. **83**, 3150 (1999).

[33] G. A. Bartholomew, Annu. Rev. Nucl. Sci. **11**, 259 (1961).

[34] D. M. Brink, Ph.d. thesis, unpublished, (1955).

[35] G. C. Baldwin and G. S. Klaiber, Phys. Rev. **73**, 1156 (1948).

[36] A. Migdal, J. Phys.(USSR) (1944).

[37] H. Steinwedel *et al.*, Phys. Rev. **79**, 1019 (1950).

[38] M. Goldhaber and E. Teller, Phys. Rev. **74**, 1046 (1948).

[39] B. L. Berman and S. C. Fultz, Rev. Mod. Phys. **47**, 713 (1975).

[40] K. A. Snover, Ann. Rev. of Nucl. Part. Sci. **36**, 545 (1986).

[41] P. Carlos *et al.*, Nucl. Phys. A **219**, 61 (1974).

[42] W. Greiner and J. A. Maruhn, *Nuclear models* (Springer, 1996).

[43] S. S. Dietrich and B. L. Berman, At. Data Nucl. Data Tables **38**, 199 (1988).

[44] G. A. Bartholomew *et al.*, Adv. Nucl. Phys. **7**, 229 (1973).

[45] C. M. McCullagh *et al.*, Phys. Rev. C **23**, 1394 (1981).

[46] W. I. Furman *et al.*, Phys. Lett. B **44**, 465 (1973).

[47] L. Aldea *et al.*, Z. Phys. A **283**, 391 (1977).

[48] Y. P. Popov, in *Neutron induced reactions* (Physics and Applications, Smolenice, 1982) p. 121.

[49] S. G. Kadmenskii, V. P. Markushev, and V. I. Furman, Sov. J. Nucl. Phys **37**, 165 (1983).

[50] S. Siem *et al.*, Phys. Rev. C **65**, 044318 (2002).

[51] M. Guttormsen *et al.*, Phys. Rev. C **68**, 064306 (2003).

[52] A. Voinov *et al.*, Phys. Rev. C **63**, 044313 (2001).

[53] H. T. Nyhus *et al.*, Phys. Rev. C **81**, 024325 (2010), Erratum in Ref. [136].

[54] R. E. Chrien, in *Proceedings of the 5th International School on Neutron Physics, Alushta, USSR, 1987* (1987) edited by B. B. Kolesova, and V. R. Sarantseva, JINR Report No. D3,4,17-86-747.

[55] J. Kopecky and M. Uhl, Phys. Rev. C **41**, 1941 (1990).

[56] S. F. Mughabghab and C. L. Dunford, Phys. Lett. B **487**, 155 (2000).

[57] S. Goriely, Phys. Lett. B **436**, 10 (1998).

[58] V. A. Plujko *et al.*, Nucl. Data Sheets **118**, 237 (2014).

[59] Goriely, S. *et al.*, Eur. Phys. J. A **55**, 172 (2019).

[60] J. Kopecky, M. Uhl, and R. E. Chrien, Phys. Rev. C **47**, 312 (1993).

[61] J. Kopecky, *Handbook for Calculations of Nuclear Reaction Data, RIPL-2*, TECDOC Series No. 1506 (IAEA, Vienna, 2006).

[62] J. Kroll *et al.*, Phys. Rev. C **88**, 034317 (2013).

[63] S. Goriely *et al.*, Phys. Rev. C **98**, 014327 (2018).

[64] A. Repko *et al.*, Eur. Phys. J. A **53**, 221 (2017).

[65] J. Kvasil *et al.*, Eur. Phys. J. A **55**, 213 (2019).

[66] V. O. Nesterenko *et al.*, Phys. Rev. C **103**, 064313 (2021).

[67] P. G. Reinhard and H. Flocard, Nucl. Phys. A **584**, 467 (1995).

[68] J. Bartel *et al.*, Nucl. Phys. A **386**, 79 (1982).

[69] E. Chabanat *et al.*, Nucl. Phys. A **635**, 231 (1998).

[70] P. Klüpfel *et al.*, Phys. Rev. C **79**, 034310 (2009).

[71] P. G. Reinhard *et al.*, Phys. Rev. C **60**, 014316 (1999).

[72] R. R. Hilton, in *Proc. of the International Conference on Nuclear Structure* (Dubna, 1976).

[73] N. L. Iudice and F. Palumbo, Phys. Rev. Lett. **41**, 1532 (1978).

[74] F. Iachello, Nucl. Phys. A **358**, 89 (1981).

[75] D. Bohle *et al.*, Phys. Lett. B **137**, 27 (1984).

[76] D. Bohle *et al.*, Phys. Lett. B **148**, 260 (1984).

[77] U. Kneissl, H. H. Pitz, and A. Zilges, Prog. Part. Nucl. Phys. **37**, 349 (1996).

[78] N. Pietralla *et al.*, Phys. Rev. C **58**, 184 (1998).

[79] A. Richter, Prog. Part. Nucl. Phys. **34**, 261 (1995).

[80] W. Ziegler *et al.*, Phys. Rev. Lett. **65**, 2515 (1990).

[81] H. Maser *et al.*, Phys. Rev. C **53**, 2749 (1996).

[82] C. Schlegel *et al.*, Phys. Lett. B **375**, 21 (1996).

[83] F. Bečvář *et al.*, Phys. Rev. C **52**, 1278 (1995).

[84] M. Krtička *et al.*, Phys. Rev. Lett. **92**, 172501 (2004).

[85] A. Chyzh *et al.*, Phys. Rev. C **84**, 014306 (2011).

[86] B. Baramsai *et al.*, Phys. Rev. C **87**, 044609 (2013).

[87] S. Valenta *et al.*, Phys. Rev. C **96**, 054315 (2017).

[88] T. Renstrøm *et al.*, Phys. Rev. C **98**, 054310 (2018).

[89] D. Frekers *et al.*, Phys. Lett. B **244**, 178 (1990).

[90] J. Kopecky and R. E. Chrien, Nucl. Phys. A **468**, 285 (1987).

[91] L. M. Bollinger and G. E. Thomas, Phys. Rev. C **2**, 1951 (1970).

[92] A. Simon *et al.*, Phys. Rev. C **93**, 034303 (2016).

[93] F. Naqvi *et al.*, Phys. Rev. C **99**, 054331 (2019).

[94] K. L. Malatji *et al.*, Phys. Rev. C **103**, 014309 (2021).

[95] R. Schwengner, S. Frauendorf, and A. C. Larsen, Phys. Rev. Lett. **111**, 232504 (2013).

[96] B. A. Brown and A. C. Larsen, Phys. Rev. Lett. **113**, 252502 (2014).

[97] R. Schwengner, S. Frauendorf, and B. A. Brown, Phys. Rev. Lett. **118**, 092502 (2017).

[98] K. Sieja, Phys. Rev. Lett. **119**, 052502 (2017).

[99] P. J. Siemens and A. S. Jensen, *Elements of Nuclei* (Addison-Wesley, 1987).

[100] J. Speth and A. van der Woude, Rep. Prog. Phys. **44**, 719 (1981).

[101] W. V. Prestwich, M. A. Islam, and T. J. Kennett, Z. Phys. A **315**, 103 (1984).

[102] F. Bečvář, Nucl. Instrum. Methods A **417**, 434 (1998), erratum in Ref. [137].

[103] M. Krtička and S. Valenta, Dicebox γ decay simulation tool (2018).

[104] C. M. Baglin, Nucl. Data Sheets **111**, 1807 (2010).

[105] T. Kibédi *et al.*, Nucl. Instrum. Methods A **589**, 202 (2008).

[106] M. Jandel *et al.*, Nucl. Instrum. Methods B **261**, 1117 (2007).

[107] G. E. Mitchell and J. F. Shriner Jr, *Missing level corrections using neutron spacings*, Tech. Rep. (International Atomic Energy Agency, 2009).

[108] T. A. Brody *et al.*, Rev. Mod. Phys. **53**, 385 (1981).

[109] H. A. Weidenmüller and G. E. Mitchell, Rev. Mod. Phys. **81**, 539 (2009).

[110] C. E. Porter and R. G. Thomas, Phys. Rev. **104**, 483 (1956).

[111] H. S. Camarda, Phys. Rev. C **49**, 1391 (1994).

[112] A. Volya, H. A. Weidenmüller, and V. Zelevinsky, Phys. Rev. Lett. **115**, 052501 (2015).

[113] P. E. Koehler *et al.*, Fortschr. Phys. **61**, 80 (2013).

[114] M. Gaudin, Nucl. Phys. **25**, 447 (1961).

[115] R. U. Haq, A. Pandey, and O. Bohigas, Phys. Rev. Lett. **48**, 1086 (1982).

[116] O. Bohigas, R. U. Haq, and A. Pandey, *Nuclear Data for Science and Technology* (Reidel, Dordrecht, 1983) edited by K. H. Böckhoff.

[117] H. I. Liou *et al.*, Phys. Rev. C **5**, 974 (1972).

[118] F. J. Dyson and M. L. Mehta, J. Math. Phys. **4**, 701 (1963).

[119] P. D. Georgopulos and H. S. Camarda, Phys. Rev. C **24**, 420 (1981).

[120] D. Mulhall, Z. Huard, and V. Zelevinsky, Phys. Rev. C **76**, 064611 (2007).

[121] P. W. Lisowski *et al.*, Nucl. Sci. Eng. **106**, 208 (1990).

[122] M. Mocko and G. Muhrer, Nucl. Instrum. Methods A **704**, 27 (2013).

[123] M. Heil *et al.*, Nucl. Instrum. Methods A **459**, 229 (2001).

[124] R. Reifarth *et al.*, Nucl. Instrum. Methods A **531**, 530 (2004).

[125] A. Couture *et al.*, EPJ Web of Conferences **93**, 07003 (2015).

[126] S. Mosby *et al.* (2018), Los Alamos National Laboratory Report No. LA-UR-18-22130 (unpublished).

[127] S. Ritt and P. A. Amaudruz, Midas–maximum integrated data acquisition system, unpublished.

[128] S. F. Mughabghab, *Atlas of Neutron Resonances* (Elsevier, 2018) Volume 2: Resonance Properties and Thermal Cross Sections Z=61-102.

[129] P. E. Koehler *et al.*, Phys. Rev. C **76**, 025804 (2007).

[130] B. Baramsai *et al.*, Phys. Rev. C **85**, 024622 (2012).

[131] F. Bečvář *et al.*, Nucl. Instrum. Methods A **647**, 73 (2011).

[132] J. Zhang, J. R. Statist. Soc. B **64**, 281 (2002).

[133] T. Kawano *et al.*, Nucl. Data Sheets **163**, 109 (2020).

[134] J. Kroll *et al.*, Phys. Scr. **T154**, 014009 (2013).

[135] T. von Egidy and D. Bucurescu, Phys. Rev. C **73**, 049901(E) (2006).

[136] H. T. Nyhus *et al.*, Phys. Rev. C **82**, 029909 (2010).

[137] F. Bečvář, Nucl. Instrum. Methods A **935**, 240 (2019).

List of Figures

1 Bohr's wooden toy model [4] . . . 3
2 Scheme of a neutron capture reaction . . . 4

1.1 Spin- and parity-summed LD models tested for ^{168}Er . . . 10
1.2 Spin distribution function $f(J, \sigma)$ of the LD models tested for ^{168}Er 11

2.1 Dipole PSF models for ^{168}Er tested in our simulations. . . . 22
2.2 Panel (a): Dipole photon strength functions models tested for ^{168}Er. Panel (b): Sum of dipole photon strength function models. . . . 23

3.1 Schematic description of generating γ cascades with the DICEBOX algorithm. . . . 29

4.1 The nearest neighbor spacing distribution for NDE. . . . 34

5.1 DANCE detector visualized with the GEANT4 simulation toolkit. 37
5.2 Left panel: Energy of the fast vs. slow component. Right panel: Deposited energy E_{dep} of the α particles . . . 39
5.3 Left panel: The measured spectrum of ^{22}Na source. Right panel: Time alignment of the crystal 5. . . . 40
5.4 Experimental E_n vs E_Σ spectrum for $^{167}\mathrm{Er}(n,\gamma)^{168}$Er summed over all multiplicities. . . . 41
5.5 Experimental sum-energy spectra from two resonances of each spin and multiplicities $M = 2 - 5$. . . . 42
5.6 Experimental MSC spectra from two resonances of each spin and multiplicities $M = 2 - 5$. . . . 43
5.7 Left panel: Scheme of the decay from the neutron capture state. Right panel: Cascades falling into the prompt gate and into the delayed gate. . . . 44
5.8 TOF spectrum of three resonances for all, prompt, and delayed events. . . . 45
5.9 Spectrum of time differences between the prompt and delayed cascades for 50.19 eV resonance. . . . 46
5.10 Partial low-level scheme of ^{168}Er including the isomeric state at 1094 keV. . . . 46

5.11 Average detector load from the higher-mass measurement. 47
5.12 Multiplicity distribution of two spin prototypes and off-resonance prototype. 49
5.13 Experimental and decomposed TOF spectra for two prototypes. . 49
5.14 Experimental and decomposed TOF spectra for three prototypes. 50
5.15 Sum-energy spectra summed over $M = 2 - 5$ from 9 eV resonance (left panel) and 22 eV resonance (right panel). 51
5.16 Experimental and decomposed TOF spectra from two measurements. 51
5.17 The multiplicity distribution of four $J = 3$ resonances constructed from events with $E_\Sigma = 7 - 8$ MeV. 52

6.1 Left panel: Simulated and experimental $2g\Gamma_n/\sqrt{E/1\text{eV}}$. Right panel: Simulated distribution of number of sub-threshold resonances. 54
6.2 Left panel: CDF of the simulated and experimental NNSD for a complete pure-spin $L_{\max} = 23$ sequence. Right panel: Right panel: Analogous figure for simulated and experimental NNSD of $L_{\max} = 69$. 56
6.3 CDF of the simulated correlation coefficient $\rho(D_i, D_{i+1})$ for a complete pure-spin $L_{\max} = 23$ sequence and $\rho^{\exp} = -0.6164$. 57
6.4 CDF for the pure-spin complete simulated sequences of $L_{\max} = 27$ to have N of $\Delta_3(L)$ points outside the simulated 95.45% central interval (i.e. $\approx 81\%$ of the 5000 simulated sequences have 0 points outside the 95.45% central interval). The experimental $J = 3$ sequence of $L_{\max} = 27$ and $E_{\max} = 200$ eV has $N = 12$ points outside the simulated 95.45% central interval (marked with a green arrow). The 4.55% limit for rejection of the hypothesis is shown as a red arrow. 58
6.5 Simulated Δ_3 statistics for mixed-spin sequences with $L_{\max} = 50$ and $L_{\text{extra}} = 0, 1$ and 7 compared to experimental values. 59
6.6 Simulated Δ_3 statistics for pure-spin sequences with $L_{\max} = 18$ and $L_{\text{extra}} = 0, 1$ and 7 compared to experimental values. 60
6.7 Comparison of the mean experimental MSC spectra and the simulated MSC spectra using the MGLO ($k = 3$) model and the Oslo model. 62
6.8 Comparison of the mean experimental MSC spectra and the simulated MSC spectra using the BSFG LD model and the HFB LD model. 63
6.9 Comparison of the mean experimental MSC spectra and the simulated MSC spectra using the CT LD model and the LEE $M1$ contribution. 64
6.10 Comparison of the mean experimental MSC spectra and the simulated MSC spectra using the SLO model and the EGLO ($k = 3$) model. 65
6.11 Comparison of the mean experimental MSC spectra and the simulated MSC spectra using the QRPA+D1M calculations and the SMLO model. 66

6.12 Comparison of the mean experimental MSC spectra and the simulated MSC spectra using the QRPA+SkI3* calculations and the QRPA+SkM* calculations. 67
6.13 Comparison of the mean experimental MSC spectra and the simulated MSC spectra using the KMF model and the MGLO ($k = 3$) model. 68
6.14 Comparison of the mean experimental MSC spectra and the simulated MSC spectra using the MGLO ($k = 3$) model constructed from $E_\Sigma = 6 - 7\,\mathrm{MeV}$ range. 69
6.15 Experimental (γ, xn) data and available parametrizations of the GEDR. 70
6.16 Top panel: The total M1 strength $\sum B^{(M1)}$ summed over $E_\gamma = 2.7 - 3.7\,\mathrm{MeV}$. Bottom panel: Total SM strength $\sum B_{\mathrm{SM}}$ integrated for $E_\gamma = 0 - 10\,\mathrm{MeV}$ 71
6.17 Simulated R_{iso} as a function of the critical energy compared to the experimental R_{iso}. 74
6.18 Low-lying level scheme of ^{168}Er with the decay of a non-doorway level and a doorway level. 75
6.19 Simulated populations of the levels as a function of the excitation energy of the level. 75
6.20 Mean experimental sum-energy spectra for $M = 2 - 4$ compared to the simulated spectra for the best model combination. 76

List of Tables

5.1 Mass and isotopic composition of the Er sample. 40

6.1 Fraction of complete mixed-spin sequences F_0^m of ^{167}Er and the mode of distribution of sub-threshold resonances. 54
6.2 Results of the statistical analysis of ^{167}Er resonance sequences. . . 55
6.3 Determined average resonance spacing D_0^-,D_0^+ and D_0. 58
6.4 The experimental results on the isomeric decay. 73

List of Abbreviations

RMT	Random Matrix Theory
LD	Level Density
PSF	Photon Strength Function
GEDR	Giant Electric Dipole Resonance
DANCE	Detector for Advanced Neutron Capture Experiments
LANL	Los Alamos National Laboratory
BSFG	Back-Shifted Fermi Gas
CT	Constant Temperature
HFB	Hartree-Fock-Bogoliubov
SSMC	Shell-Model Monte Carlo
TRK	Thomas-Reiche-Kuhn
SLO	Standard Lorentzian
KMF	Kadmenskij-Markushev-Furman
KMF-T	Kadmenskij-Markushev-Furman with Constant T
GLO	Generalized Lorentzian
ELO	Lorentzian with Energy-Dependent Width
MLO	Modified Lorentzian
SMLO	Simplified Modified Lorentzian
ARC	Average Resonance Capture
EGLO	Enhanced Generalized Lorentzian
MGLO	Modified Generalized Lorentzian
QRPA	Quasiparticle Random–Phase Approximation
SM	Scissors Mode
SF	Spin-Flip Mode
LEE	Low-Energy Enhancement
NRF	Nuclear Resonance Fluorescence
TSC	Two-Step Cascade
GEQR	Giant Electric Quadrupole Resonance
SP	Single-Particle
PT	Porter-Thomas
NR	Nuclear Realization
NS	Nuclear Suprarealization
RNG	Random Number Generator
GOE	Gaussian Orthogonal Ensemble
NNSD	Nearest Neighbor Spacing Distribution
NDE	Nuclear Data Ensemble
LANSCE	Los Alamos Neutron Science Center
MIDAS	Maximum Integrated Data Acquisition System
MSC	Multi-Step Cascade
CDF	Cumulative Distribution Function

List of Publications

1. N. Simbirtseva , M. Krtička, R. F. Casten, A. Couture, W. I. Furman, I. Knapová, J. M. O'Donnell, G. Rusev, J. L. Ullmann, and S. Valenta

   Examination of photon strength functions and nuclear level density in ^{196}Pt from the γ-ray spectra measured at the DANCE facility

   Physical Review C **101** (2020) 024302

2. I. Knapová, S. Valenta, B. Baramsai, T. A. Bredeweg, A. Couture, C. Fry, M. Jandel, J. Kroll, M. Krtička, G. E. Mitchell, J. M. O'Donnell, C. J. Prokop, G. Rusev and J. L. Ullmann

   Spin assignment and statistical properties of neutron resonances from ^{161,163}Dy(n,γ) and ^{167}Er(n,γ) measured at the DANCE facility

   accepted in Physical Review C (CS10722), July 16 (2022)

3. I. Knapová, F. Bečvář, R. F. Casten, A. Couture, C. Fry, J. Kvasil, M. Krtička, V. O. Nesterenko, J. M. O'Donnell, C. J. Prokop, G. Rusev, J. L. Ullmann and S. Valenta

   Photon strength functions, level densities and isomeric ratio in ^{168}Er from the radiative neutron capture measured at the DANCE facility

   to be submitted to Physical Review C, August (2022)

Appendices

A. Spin assignment and statistical properties of neutron resonances from $^{161,163}\mathrm{Dy}(n,\gamma)$ and $^{167}\mathrm{Er}(n,\gamma)$ measured at the DANCE facility

Authors:

I. Knapová, S. Valenta, B. Baramsai, T. A. Bredeweg, A. Couture, C. Fry, M. Jandel, J. Kroll, M. Krtička, G. E. Mitchell, J. M. O'Donnell, C. J. Prokop, G. Rusev and J. L. Ullmann

Accepted:

Physical Review C, CS10722, July 16 (2022).

B. Photon strength functions, level densities and isomeric ratio in ^{168}Er from the radiative neutron capture measured at the DANCE facility

Authors:

I. Knapová, F. Bečvář, R. F. Casten, A. Couture, C. Fry, J. Kvasil, M. Krtička, V. O. Nesterenko, J. M. O'Donnell, C. J. Prokop, G. Rusev, J. L. Ullmann and S. Valenta

To be submitted:

Physical Review C, August (2022).